

AD-A242 027

PAGE

Form Approved  
OMB No. 0704-0188Public reporting  
burden and  
collection of  
this data  
has been  
reduced by  
this  
document.

or required, including the time for reviewing instructions, searching existing data sources, gathering the data, reviewing the data, and completing the review of this information. Send comments regarding this burden estimate or any other aspect of this document, including suggestions for reducing the burden, to Washington Headquarters Services, Directorate for Information Operations and Reports, 1215 Jefferson Avenue, Washington, DC 20540.

1. AGENCY (Use ONLY (Leave blank))

2. REPORT DATE

31 August 1991

3. REPORT TYPE AND DATES COVERED

Final Technical 1 May 1988-30 Jun 1990

4. TITLE AND SUBTITLE

(U) Local Extinction Mechanisms in Non-Premixed  
Turbulent Combustion

5. FUNDING NUMBERS

PE - 61102F

PR - 2308

SA - BS

C - F49620-88-C-0066

6. AUTHOR(S)

S M Correa and A Gulati

7. PERFORMING ORGANIZATION NAME(S) AND ADDRESS(ES)

General Electric Corporate Research and Development  
P O Box 8  
Schenectady NY 123018. PERFORMING ORGANIZATION  
REPORT NUMBER

AFOSR-TR-

91 0871

9. SPONSORING/MONITORING AGENCY NAME(S) AND ADDRESS(ES)

AFOSR/NA  
Building 410  
Bolling AFB DC 20332-644810. SPONSORING/MONITORING  
AGENCY REPORT NUMBER

11. SUPPLEMENTARY NOTES

D.T.I.C.  
ELECTE  
OCT 22 1991  
S B D

12a. DISTRIBUTION/AVAILABILITY STATEMENT

Approved for public release; distribution is  
unlimited

12b. DISTRIBUTION CODE

13. ABSTRACT (Maximum 200 words)

The goal of this research program was a quantitative understanding of turbulence-chemistry interactions pertinent to future aeropropulsion combustors. For example, (i) flameout and relight in turbine combustors are related to interactions of turbulence with chain-branching reactions, (ii) hydrogen burnout in supersonic combustors is related to interactions with recombination reactions, and (iii) emissions of NO<sub>x</sub>, CO, smoke and other observables are related to nonequilibrium in the populations of intermediate species such as oxyhydrogen radicals and C<sub>2</sub>H<sub>2</sub>.

A bluff-body stabilized turbulent diffusion flame, time- and space-resolved laser Raman measurements of major species, and a nonequilibrium computational fluid mechanics code were applied to the problem. The principal conclusions are

1. Turbulent jet flames are being abandoned in the search for more intensely turbulent flames.
2. An axisymmetric bluff-body stabilized turbulent diffusion flame burner is a reasonable choice for combustion research at high Reynolds numbers, approaching blowoff.

14. SUBJECT TERMS

Turbulent Combustion, Modeling, Raman Scattering, Strained  
Flames, Local Extinction

15. NUMBER OF PAGES

69

16. PRICE CODE

17. SECURITY CLASSIFICATION  
OF REPORT

Unclassified

18. SECURITY CLASSIFICATION  
OF THIS PAGE

Unclassified

19. SECURITY CLASSIFICATION  
OF ABSTRACT

Unclassified

20. LIMITATION OF ABSTRACT

UL

NSN 7540-01-280-5500

91 10 22 050

Standard Form 298 (890104) Drg  
Prescribed by ANSI Std. Z39-18  
700-01

91-13762

Original contains color  
plates. DTIC reproduction  
not available in black and  
white.

3. Raman scattering for measurements of major species and temperature can be extended into the sooting/chemiluminescent environment of methane flames. Space- and time-resolved Raman scattering measurements have been made in bluff-body stabilized CO/H<sub>2</sub>/N<sub>2</sub> and CH<sub>4</sub> flames at conditions approaching blowoff.
4. A thermochemical submodel based on partial equilibrium in the oxyhydrogen radical pool was developed for the 27.5% CO/ 32.3% H<sub>2</sub>/40.2% N<sub>2</sub>-air system. The chemistry can be described in terms of two scalars. The elliptic form of the time-averaged Navier Stokes equations with k- $\epsilon$  closure was solved using an iterative finite-volume/pressure-correction algorithm. Mean properties such as density were obtained at each iteration by convolution with the joint pdf over the two thermochemical scalars. The pdf itself was obtained by the moment-equation/assumed-shape method.
5. Calculations compare favorably with the Raman data.
6. Work on pdf transport/Monte-Carlo methods in recirculation-stabilized flames has begun.
7. The range of turbulence-chemistry interactions in combustion has been quantified, in an attempt to gauge the universality of turbulence-chemistry models. While some combustion reactions fall in the flamelet regime and some in the distributed regime, many important reactions fall in between. Turbulence-chemistry interactions occur in a greater variety of modes than accounted for by current combustion theory. The simultaneous prediction of kinetically sensitive phenomena such as pollutants, flame stability and combustion efficiency, will require a new approach.

## Table of Contents

### Section

	Nomenclature .....	ix
1	Summary .....	1
2	Technical Discussion.....	3
2.1	Choice of Axisymmetric Bluff-Body Stabilized Burner over Jet Flame .....	4
2.2	Setup of Experiments .....	5
2.3	Discussion of Data .....	16
2.4	Governing Equations and Models .....	21
2.5	Comparison of Model Predictions with Data .....	38
2.6	Monte-Carlo Pdf Transport Method in Recirculating Flow .....	58
2.7	Universality of Turbulence-Chemistry Models.....	58
3	Conclusions .....	63
4	References .....	65
5	Written Publications.....	68
6	Professional Personnel .....	69
7	Interactions.....	69



<b>Accession For</b>	
NTIS GRA&I	<input checked="" type="checkbox"/>
DTIC TAB	<input type="checkbox"/>
Unannounced	<input type="checkbox"/>
Justification .....	
By .....	
Distribution/ .....	
Availability Codes	
Dist	Avail and/or Special
A-1	

## List of Illustrations

### Figure

1	Inlet conditions and schematic of the burner in the tunnel .....	6
2	Photograph of the Raman system consisting of the dye laser, data acquisition electronics, and the flow tunnel .....	8
3	Photograph showing the spectrometer and the PMT housing box.....	9
4	The bluff-body stabilized CO/H <sub>2</sub> /N <sub>2</sub> flame.....	10
5	The bluff-body stabilized methane flame.....	10
6	Schematic showing the location of the two additional photomultiplier tubes (F1 and F2) used to monitor the laser-induced fluorescence relative to other Raman channels in the wavelength space .....	12
7	Raw Raman data (mean profiles) for N <sub>2</sub> , O <sub>2</sub> , CH <sub>4</sub> , and CO at x = 10 mm, in a laminar diffusion CH <sub>4</sub> /CO (70%) flame .....	13
8	Raw Raman data (mean profiles) for CO <sub>2</sub> , H <sub>2</sub> O, and H <sub>2</sub> at x = 10 mm, in a laminar diffusion CH <sub>4</sub> /CO (70%) flame .....	13
9	Comparison of reduced Raman data with laminar counterflow diffusion flame calculation with correction factors for fluorescence set to zero: Temperature .....	14
10	Comparison of reduced Raman data with laminar counterflow diffusion flame calculation with correction factors for fluorescence set to zero: N <sub>2</sub> , O <sub>2</sub> , and CO.....	14
11	Comparison of reduced Raman data with laminar counterflow diffusion flame calculation with correction factors for fluorescence set to zero: CO <sub>2</sub> , H <sub>2</sub> , and CH <sub>4</sub> .....	15
12	Comparison of fluorescence-corrected Raman data, corresponding to Fig. 9, with laminar counterflow diffusion flame calculation.....	17
13	Comparison of fluorescence-corrected Raman data, corresponding to Fig. 10, with laminar counterflow diffusion flame calculation.....	17
14	Comparison of fluorescence-corrected Raman data, corresponding to Fig. 11, with laminar counterflow diffusion flame calculation.....	18
15	Schematic of various regions of the bluff-body stabilized methane flame indicating various regions of interest.....	18
16	Scattergram of temperature vs. mixture fraction at x/d = 5 .....	19
17	Scattergram of temperature vs. mixture fraction in the narrow neck region of the flame (x/d = 10 and 20).....	19
18	Scattergram of temperature vs. mixture vs. mixture fraction at x/d = 30 .....	20
19	Scattergram of temperature vs. mixture vs. mixture fraction at x/d = 70 .....	20

20	Scattergram of mass-fraction of $O_2$ vs. mixture fraction in the narrow neck region of the flame ( $x/d = 20$ ).....	22
21	Scattergram of mass-fraction of $N_2$ vs. mixture fraction in the narrow neck region of the flame ( $x/d = 10$ and $20$ ).....	22
22	Scattergram of mass-fraction of $CH_4$ vs. mixture fraction in the narrow neck region of the flame ( $x/d = 10$ and $20$ ).....	23
23	Scattergram of mass-fraction of $H_2O$ vs. mixture fraction in the narrow neck region of the flame ( $x/d = 10$ and $20$ ).....	23
24	Scattergram of mass-fraction of $CO_2$ vs. mixture fraction in the narrow neck region of the flame ( $x/d = 20$ ).....	24
25	Profile of mean temperature across the burner at $x/d = 10$ .....	24
26	Profile of normalized r.m.s. temperature across the burner at $x/d = 10$ .....	25
27	Measured mean profile of $O_2$ , $N_2$ , and $CH_4$ across the burner at $x/d = 10$ .....	25
28	Measured mean profile of $CO$ and $H_2$ across the burner at $x/d = 10$ .....	26
29	Measured mean profile of $CO_2$ and $H_2O$ across the burner at $x/d = 10$ .....	26
30	Contours in thermochemical phase space .....	33
31	Nonuniform rectilinear $75$ (axial) $\times$ $60$ (radial) grid.....	39
32	Transverse cell Reynolds numbers in the calculation .....	41
33	Contours of the Favre-averaged mean mixture fraction.....	42
34	Contours of the Favre-averaged mixture fraction variance.....	42
35	Contours of the mean temperature .....	44
36	Contours of the mean reaction progress variable .....	44
37	Contours of the Favre-averaged mean species mass fractions.....	45-49
38	Centerline axial profile of the mean density .....	49
39	Centerline axial profile of the mean axial velocity .....	50
40	Centerline axial profile of the mean turbulence kinetic energy .....	50
41	Centerline axial profile of the mean mixture fraction .....	51
42	Centerline axial profile of the variance in mixture fraction .....	51
43	Normalized turbulence intensity $\sqrt{(2k/3)} / U$ along centerline.....	52
44	Comparison of predicted normalized scalar variance with Raman data .....	52
45	Comparison of predicted radial profiles with Raman data at $x/d = 10$ .....	53-55
46	Comparison of predicted radial profiles at $x/d = 15.4$ with Raman data at $x/d = 20$ .....	56

47	Comparison of the predicted normalized r.m.s. mixture fraction with the Raman data at $x/d = 10$ .....	57
48	Comparison of the predicted normalized r.m.s. mixture fraction with the Raman data at $x/d = 40$ .....	57
49	Application of hybrid Monte-Carlo-pdf transport/finite-difference code to axisymmetric constant-density 1:2 sudden-expansion flow with step-function inlet profile for the conserved scalar.....	59

## NOMENCLATURE

$a, b$	Parameters in beta function
$c_1 - c_3$	Parameters in pdf
$C_1, C_2$	Constants in k- $\epsilon$ model
$D$	Diffusion coefficient
$d$	Diameter
$f$	pdf of conserved scalar
$g$	pdf of reactive scalar
$h$	Total enthalpy
$j$	Turbulent flux
$J$	Jacobian
$k$	Turbulence kinetic energy, reaction rate
$M$	Number of chemical elements
$M_i$	Molecular mass of species $i$
$N$	Number of species
$p$	Pressure
$P$	Probability density function
$Pe$	Peclet number
$Pr$	Prandtl number
$q$	Twice the turbulence kinetic energy
$q_{ij}$	Metric terms in coordinate transformation
$R$	Universal gas constant, turbulence time-scale ratio
$\dot{r}$	Reaction rate per unit volume
$S$	Swirl ratio, source term
$Sc$	Schmidt number
$T$	Temperature
$U, V, W$	Contravariant velocity components

$u, v, w$	Velocity components in Cartesian coordinates
$u_i$	Velocity component in $i$ direction
$\dot{w}_i$	Rate of reaction $i$
$x_i$	Cartesian coordinate $i$
$Y_i$	Mass fraction of species $i$
$z_i$	Elemental mass fraction of species $i$
$\beta$	Beta function
$\Gamma_i$	Diffusion coefficient for quantity $i$
$\delta$	Dirac delta function
$\varepsilon$	Dissipation rate
$\eta$	Reaction progress variable, coordinate
$\mu$	Viscosity
$\mu_{ij}$	Mass of $i$ th element in unit mass of $j$ th species
$\nu$	Kinematic viscosity
$\xi$	Mixture fraction, coordinate
$\rho$	Density
$\sigma_i$	Turbulent Prandtl number for quantity $i$
$\tau$	Time
$\tau_{ij}$	Turbulent stress
$\phi$	Scalar variable, generalized variable
$\psi$	Deviation variable for CO kinetics

#### Subscripts

$\xi, \eta, \gamma$	Derivative with respect to coordinate $\xi, \eta, \gamma$
$i$	Cartesian component
$s$	Species index



### Superscripts

$l$	Laminar
$a$	Air
$e$	Equilibrium
$f$	Fuel
$s$	Stretched
$t$	Turbulent
$u$	Unburned (frozen)
$(\sim)$	Density-weighted mean
$(\sim)''$	Density-weighted fluctuation
$*$	Transformed variable
$(-)$	Conventional mean
$(-)'$	Conventional fluctuation

## Section 1

### SUMMARY

This report describes work performed in the period May 1988 to June 1991 for the U.S. Air Force Office of Scientific Research under Contract F49620-88-C-0066. Dr. Julian Tishkoff was the AFOSR Project Monitor. The work was performed and the report has been prepared by the Engineering Systems Laboratory at the General Electric Research and Development Center, Schenectady, New York. This section summarizes the technical problem which was considered and outlines the results obtained in the course of the program.

Aircraft and industrial gas-turbine engines generally employ non-premixed turbulent combustion. The goal of this three-year research program was a quantitative understanding of turbulence-chemistry interactions in such flames. Although the fast chemistry or "mixed-is-burned" paradigm is useful for understanding traditional design issues, present-day demands on combustion equipment and thus on computational models are increasing the need for a more advanced understanding of turbulence-chemistry interactions. For example, (i) flameout and relight in turbine combustors are related to interactions of turbulence with chain-branching reactions, (ii) hydrogen burnout in supersonic combustors is related to interactions with recombination reactions, and (iii) emissions of  $\text{NO}_x$ , CO, smoke and other observables are related to nonequilibrium in the populations of intermediate species such as oxyhydrogen radicals and  $\text{C}_x\text{H}_y$ .

#### Statement of Work

- a. Identify conditions necessary to observe extinction in pilot-stabilized hydrocarbon jet flames.
- b. Modify the Raman system to obtain data in the blue region of hydrocarbon jet flames; measure major species concentrations, temperature, and density under local extinction conditions; measure inlet conditions for modeling purposes.
- c. Extend the chemical scheme in the model to hydrocarbons, using multistep/partial-equilibrium schemes and apply joint pdf/Monte Carlo and conventional flow models to hydrocarbon jet flames.
- d. Compare data and calculations; evaluate the model and mechanisms of extinction, hypothesize new mechanisms if necessary.
- e. Use a combustor with bluff-body stabilization of carbon monoxide/hydrogen/nitrogen flames at high Reynolds numbers and establish local extinction conditions.
- f. Measure major species concentrations, temperature, and density in bluff-body stabilized carbon monoxide/hydrogen/nitrogen flames under conditions of significant local extinction; if significant levels are not found, use hydrocarbon fuels; measure inlet conditions for modeling purposes.
- g. Model the bluff-body-stabilized flames using state-of-art numerical techniques, algebraic or differential Reynolds stress models for turbulence, and turbulence-chemistry interaction models suggested by the work in jet flames, compare with data and draw conclusions regarding extinction mechanisms.
- h. In flames(s) that show the most significant local extinction, measure velocity and turbulence intensity (LDV) and minor species concentrations (saturated laser-induced fluorescence of OH), establish the topology of the flame through planar OH imaging and Schlieren photography; estimate scalar dissipation rates by Rayleigh (or Raman, if possible) imaging.

- i. Investigate the universality of the turbulence-chemistry interaction model by calculating a range of measured nonequilibrium phenomena from low levels of superequilibrium radicals to local extinction.

#### Status

A bluff-body stabilized turbulent diffusion flame, time- and space-resolved laser Raman measurements of major species, and a nonequilibrium computational fluid mechanics code were applied to the problem. The principal conclusions are

1. Turbulent jet "diffusion" flames are being abandoned in the search for more intensely turbulent flames. Jet flames, however, have had a highly successful record over the last twenty years and have provided most of the current understanding of turbulence-chemistry interactions in non-premixed flames.
2. An axisymmetric bluff-body stabilized turbulent diffusion flame burner is a reasonable choice for combustion research at high Reynolds numbers, approaching blowoff.
3. Raman scattering for measurements of major species and temperature was extended into the sooting/chemiluminescent environment of methane flames. (This requires substantial time and effort and precluded LDV and LIF (OH) measurements.) Space- and time-resolved Raman scattering measurements have been made in bluff-body stabilized CO/H<sub>2</sub>/N<sub>2</sub> and CH<sub>4</sub> flames at conditions approaching blowoff.
4. A thermochemical submodel based on partial equilibrium in the oxyhydrogen radical pool was developed for the 27.5% CO/ 32.3% H<sub>2</sub>/ 40.2% N<sub>2</sub>-air system. The chemistry can be described in terms of two scalars.
5. The elliptic form of the time-averaged Navier Stokes equations with k- $\epsilon$  closure was solved using an iterative finite-volume/pressure-correction algorithm. Mean properties such as density were obtained at each iteration by convolution with the joint pdf over the two thermochemical scalars. The pdf itself was obtained by the moment-equation/assumed-shape method.
6. Calculations have been compared with the Raman data.
7. Work on pdf transport/Monte-Carlo methods in recirculation-stabilized flames has begun.
8. The range of turbulence-chemistry interactions in combustion has been quantified in an attempt to gauge the universality of turbulence-chemistry models. While some combustion reactions fall in the flamelet regime and some in the distributed regime, many important reactions fall in between.

This study has shown that turbulence-chemistry interactions occur in a greater variety of modes than accounted for by current combustion theory. The simultaneous prediction of kinetically sensitive phenomena such as pollutants, flame stability and combustion efficiency will require a new approach.

## Section 2

### TECHNICAL DISCUSSION

This study consisted of experiments on and modeling of turbulence-chemistry interactions in turbulent gaseous flames under conditions approaching blowoff. It builds on prior work, first on unassisted and more recently on pilot-stabilized  $\text{CO}/\text{H}_2/\text{N}_2$  jet flames in coflowing air. To obtain higher turbulent strain rates than attainable even with pilot-flame stabilization, an axisymmetric bluff-body stabilized burner was used. First, however, the merits of jet flames are reviewed.

The relatively simple fuel-jet-in-coflowing-air configuration has been favored for twenty years because the mean profiles can be predicted by gradient diffusion models [Starter and Bilger (1980, 1981); Lockwood and Stolakis (1983)], the flow can be described by the computationally straightforward shear layer form of convection-diffusion-source equations, and the flame permits laser-based spectroscopic measurements which have become critical to progress in understanding. Penner et al. (1984) review a wide variety of these laser-based methods. Jet flames can be fully turbulent and manifest a wide range of turbulence-chemistry interactions. Because of these advantages, studies in jet flames have contributed much to turbulent combustion.

As the Reynolds number of the jet is increased, the flame blows off the lip at the exit of the nozzle. Thus strong turbulence-chemistry interactions leading to turbulent extinction cannot be studied.

In the preceding study, we investigated a non-premixed turbulent jet flame composed volumetrically of a 40%  $\text{CO}/10\% \text{H}_2/50\% \text{N}_2$  mixture in co-flowing air [Correa and Gulati (1989)]. This mixture of  $\text{CO}$  and  $\text{H}_2$  was used as the fuel because the chemistry is known and can be simplified reasonably well and the extinction limits approach those of hydrocarbons, which are the fuels of practical relevance. The flame was stabilized by a co-annular premixed pilot flame. Pointwise measurements included (i) temperature, mole fractions of major species, and mixture fraction  $\xi$ , by spontaneous Raman spectroscopy and (ii) velocity, by laser velocimetry. The data, e.g., temperature-mixture fraction scattergrams, showed significant temperature decrements due to finite-rate chemistry but no evidence of localized extinction.

A computational model for a jet flame under such conditions was also presented in Correa and Gulati (1989). Combustion chemistry was represented by two-body shuffle reactions and three-body recombination reactions. The scalar dissipation rate field was examined for a critical value below which the two-body reactions were assumed to be in partial equilibrium and above which they were assumed to be frozen and the gas therefore unburned. The kinetics of the recombination reactions were activated for the former fraction of the gas. This approach was implemented in a shear-layer finite-volume averaged Navier-Stokes model with  $k-\epsilon$ /assumed shape probability density function (pdf) submodels for turbulence. It was concluded that local strain-induced extinction is not seen in the above  $\text{CO}/\text{H}_2/\text{N}_2$ -air flame, despite its relatively low critical strain of  $950 \text{ s}^{-1}$  in a laminar counterflow diffusion flame ("Tsuji") burner. Localized extinction is absent because the reaction zones, centered on  $\xi_s \approx 0.43$ , are too broad to interact with the straining scales [Peters (1988), Bilger (1989)].  $\text{H}_2$  and  $\text{CH}_4$  flames have much narrower reaction zones, and  $\text{CH}_4$  flames do indeed show localized extinction. Alkyl consumption of radicals may, however, provide a chemical (nonaerodynamic) explanation for extinction in the methane case [Bilger (1989)].

The jet-flame work has shown that it is overly simplistic to consider turbulent flames as ensembles of laminar flames subjected to strain. The reason is that different kinetic steps in a combustion mechanism can have widely disparate time-scales (e.g., chain-branching reactions are much faster than recombination reactions). The fastest reactions can interact with the local turbulence in a "flamelet" manner while, for the slow reactions, the Damkohler numbers are relatively small and the

flame is more akin to a well-distributed zone of reaction. Section 2.7 presents a more detailed discussion of this point.

## 2.1 Choice of Axisymmetric Bluff-Body Stabilized Burner over Jet Flame

To increase the interaction between turbulence and chemistry, and the probability of localized extinction, the jet velocity in the pilot-stabilized burner was increased; however, only a small increase was possible before the flame blew off the lip. Moreover, the coannular premixed pilot flame used to stabilize the (non-premixed) jet flame complicates the near-field turbulence, without greatly increasing permissible dissipation rates prior to blowoff. To remedy this, we switched to an axisymmetric bluff-body stabilized non-premixed flame, with a view to obtaining Raman data on turbulence-chemistry interactions at very high dissipation rates. While axisymmetric bluff-body stabilized burners can be operated in a regime dominated by unsteady vortex shedding [Correa and Pitz (1982), Roquemore et al. (1982)], here we wish to avoid unsteadiness in the mean flow.

Axisymmetric bluff-body stabilized flames have two advantages over jet flames, but one significant drawback. The first advantage is that the cylindrical shear layer behind the bluff body provides a region of large dissipation rates, located far enough downstream of the bluff body that perturbations at the inlet should not affect the dissipation field dramatically. [In jet flames the maximum dissipation rates are at the lip of the jet, a region which is very sensitive to the inlet conditions.] The second advantage is that there is no need for pilot stabilization and thus there is no interference from the premixed pilot as might occur in jet flames. On the other hand, the major drawback of bluff-body flows is that they cannot be modeled as accurately as shear flows and jets because of the elliptic nature of the flowfield and the lack of sufficiently reliable turbulence models for recirculating flow. These problems historically overshadowed the modeling of many turbulence-chemistry effects, making evaluation of the models difficult. Large supercomputers and improved modeling techniques, however, have made it worthwhile to model the axisymmetric bluff-body experiments now being performed.

Other researchers are also being driven away from jet flames in the search for higher turbulence levels. Notice the increase in complexity in the following sequence of experiments:

1. Simple jet flames, e.g., those reviewed by Strahle and Lekoudis (1985).
2. Pilot-stabilized jet flames (pilot disturbances in enthalpy and other quantities are generally assumed away in calculations).
3. The axisymmetric "Reverse Flow Reactor," employed at the University of Sydney/SANDIA (Mansour et al. 1989), which uses flow recirculation to stabilize the flame above jet-blowoff conditions.
4. Axisymmetric bluff-body stabilized flames, such as one being studied using advanced laser diagnostics including Raman imaging by an ALTEX/SANDIA team [Schefer et al. (1989)]. An earlier propane-fueled bluff-body stabilized flame at the U.S. Air Force Aeropropulsion Laboratory [Roquemore et al. (1982)] was analyzed computationally by Correa (1984), using an equilibrium chemistry/assumed shape pdf approach. This study revealed many of the shortcomings of such models. Later work by Switzer et al. (1985) applied CARS to this bluff-body stabilized flame.
5. The GE axisymmetric bluff-body stabilized burner developed and used in the present study.

It is clear that simple "parabolic" flows are being replaced in the drive toward strong turbulence-chemistry interactions. It will be necessary to accurately model these more complex flows if the link

between theory and experiment is to continue as productively as before.

## 2.2 Setup of Experiments

Since the turbulence in a pilot-stabilized non-premixed turbulent  $\text{CO}/\text{H}_2/\text{N}_2$  jet flame was not intense enough to cause local extinction, axisymmetric bluff-body stabilization was resorted to.

### 2.2.1 Bluff-Body Stabilized Burner

Typical conditions and a schematic of the burner in the tunnel are shown in Figure 1. The subsonic, low turbulence wind tunnel has been used extensively for experimental studies of laminar, transitional, and turbulent diffusion flames in the past [Lapp et al. (1983)]. The axisymmetric bluff-body has an outer diameter of 38.1 mm with an axial jet of diameter 3.18 mm located in the center. The back surface of the bluff body is coated with a thermal barrier material to reduce heat loss. The flame is stabilized by the recirculation zone provided by the bluff body. The ratio of the bluff-body diameter to the central jet diameter is 12:1. The tunnel cross section is 6 in.  $\times$  6 in. so, and the bluff-body blockage is  $\sim$  5%. Comprehensive observations and photographs of  $\text{H}_2$ ,  $\text{CO}/\text{H}_2/\text{N}_2$ ,  $\text{CH}_4$ , and  $\text{CH}_4/\text{N}_2$  flames at various air and fuel jet velocities were obtained earlier and have been used to select promising cases for the Raman-scattering measurements reported below.

### 2.2.2 Raman Setup

The Raman diagnostic system used for space (almost) and time-resolved measurement of temperature, mixture fraction and major species is similar to that used earlier for  $\text{H}_2$  and  $\text{H}_2/\text{CO}/\text{N}_2$  flames and was described in detail by Lapp et al. (1983). For Raman measurements in methane flames, the system was extensively modified to account for the significant levels of laser-induced fluorescence/incandescence encountered in the rich sooty zone of flame, as described below.

#### (a) Raman Measurements in Bluff-Body Stabilized $\text{CO}/\text{H}_2/\text{N}_2$ Flame

The Raman system is based on a flashlamp pumped dye laser which provides pulses of  $\sim 1\text{J}$  in 2-4  $\mu\text{s}$  within a 0.2 nm bandpass at 488.0 nm at a repetition rate of 10 pps. The light scattered at right angles is collected by two lenses, separated in frequency by a 3/4 m spectrometer and is detected by eight photomultiplier tubes. The photomultiplier tubes detect anti-Stokes vibrational Raman scattering from  $\text{N}_2$ , Stokes vibrational Raman scattering from  $\text{N}_2$ ,  $\text{O}_2$ ,  $\text{H}_2$ ,  $\text{H}_2\text{O}$ ,  $\text{CO}$  and  $\text{CO}_2$ , and Rayleigh scattering. The temporal resolution (2  $\mu\text{s}$ ) of the technique is limited by the laser pulse length, the spatial resolution ( $0.2 \times 0.2 \times 0.6\text{ mm}$ ) by the spectrometer entrance slit and the collection optics, while the data acquisition rate (5 Hz) is limited by the laser repetition rate. The flame luminescence was found to be very broad-banded throughout the visible region. A polarization filter was used in the collection optics system to reduce flame luminescence. The polarization vector was aligned to pass the horizontally polarized Raman- and Rayleigh-scattered light. Typically 200 measurements were made at each flame location. 2000 shots were also recorded at some locations for statistical purposes.

The joint Rayleigh-Raman data is obtained as follows. The photomultiplier tubes are gated electronically before and after the firing of the laser. The differential voltages, which correspond to the Raman signal minus the flame background at  $t=0$  are amplified and filtered before digitization using a 12-bit A/D convertor. The signals are then corrected for electrical and other background errors corresponding to each channel and are normalized by the laser energy for every shot. The subsequent signals are corrected for relative sensitivities of the photomultiplier tubes to obtain the final values corresponding to the vibrational intensities of Raman scattering (which is linearly proportional to the number density) in the bandpass of the exit slits of the spectrometer. The system is calibrated exten-

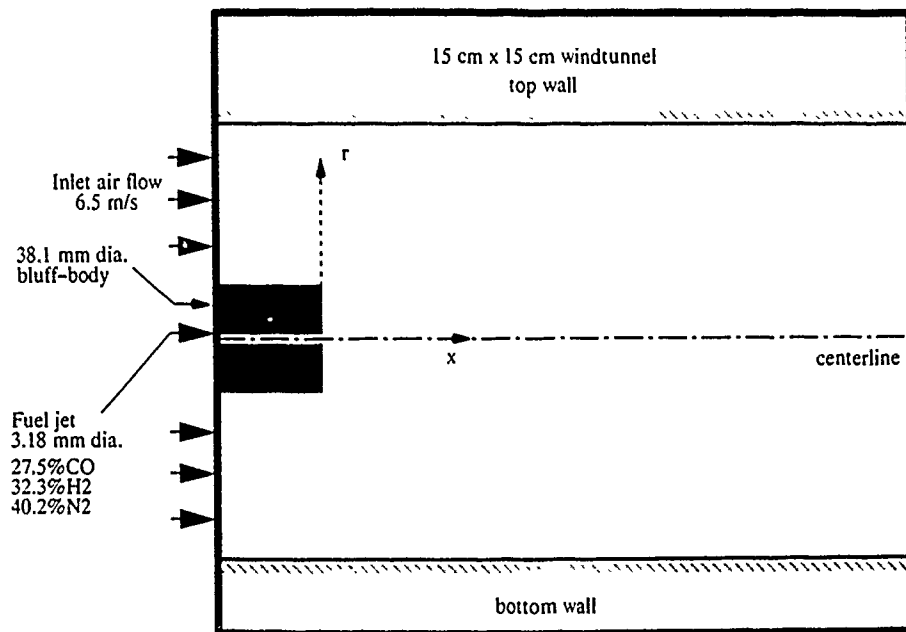


Figure 1. Inlet conditions and schematic of the burner in the tunnel.

sively using 100% pure gases and well-characterized premixed porous plug burners before and after each set of data in the turbulent flame is obtained. The data is collected using data translation DT2821 board mounted in a DELL333 system using GLOBAL lab software. The data is processed on the IBM compatible DELL system. Figure 2 shows the Raman system consisting of the dye laser, data acquisition electronics, and the flow tunnel. Figure 3 shows the spectrometer and the PMT housing box from the other side of the setup.

A photograph of the bluff-body stabilized CO/H<sub>2</sub>/N<sub>2</sub> flame used in this study is shown in Figure 4. The flame is bluish-white because of chemiluminescence, but no yellow sooty region is visible.

The instantaneous temperature at every shot was determined using three independent methods. The Stokes-anti-Stokes (SAS) ratio method as described in Drake et al. (1982) is based on the nitrogen element and yields the temperature directly. The second method is based on an iterative scheme in which an initial temperature is guessed, based on which the mole fraction of all major species are calculated using their measured vibrational intensities. The mole fractions are then corrected using high-temperature correction factors to account for changes in the fraction of the Raman band falling in the exit slits provided for the respective photomultiplier tubes. The iteration process is repeated till the sum of the mole fractions is unity. This iteration procedure converges in two to three iterations since the correction factors are relatively weak functions of temperature. The mixture fraction is calculated using the definition suggested by Bilger (1989) which takes into account the balance of three atoms i.e., C, H, and O, and is defined such that the conserved scalar preserves its stoichiometric value even in the presence of differential diffusion.

$$\zeta = \frac{2 Z_C/W_C + \frac{1}{2} Z_H/W_H + (Z_{O,a} - Z_O)/W_O}{2 Z_{C,f}/W_C + \frac{1}{2} Z_{H,f}/W_H + Z_{O,a}/W_O} \quad (1)$$

Other definitions of mixture fraction were also used.

In this flame it was found that the chemiluminescence caused by the CO + O → CO<sub>2</sub> reaction was significant and extra precautions had to be taken to improve the signal-to-noise ratio, such as inserting a polarization filter in the collection optics, reducing the entrance slit size, and so on. In addition, since the N<sub>2</sub> channel is affected most by the luminosity of the flame, the SAS measurements were susceptible to this error. Hence, Rayleigh scattering was used to obtain an independent measurement of temperature. Since the flame is of the diffusion or non-premixed type, additional information about the Rayleigh cross section of the species involved is needed for Rayleigh scattering to be applicable. In this flame the Raman scattering signals from the major species were used to obtain information about changes in the Rayleigh cross section of the mixture, and thus we were able to measure temperature in an iterative manner.

Results are discussed in subsection 2.3.

#### (b) Raman Measurements in a Bluff-Body Stabilized Pure Methane Flame

Figure 5 shows that the methane flame has a sooty yellow region in the recirculation zone of the bluff body. The flame then narrows significantly and appears to be intermittently connected in the neck region, following which the flame is fairly blue. Initial measurements with the Raman system showed that there was significant laser-induced fluorescence interference throughout the flame, as also reported in Masri et al. (1987, 1988, 1989), and Dibble et al. (1987). The fluorescence is believed



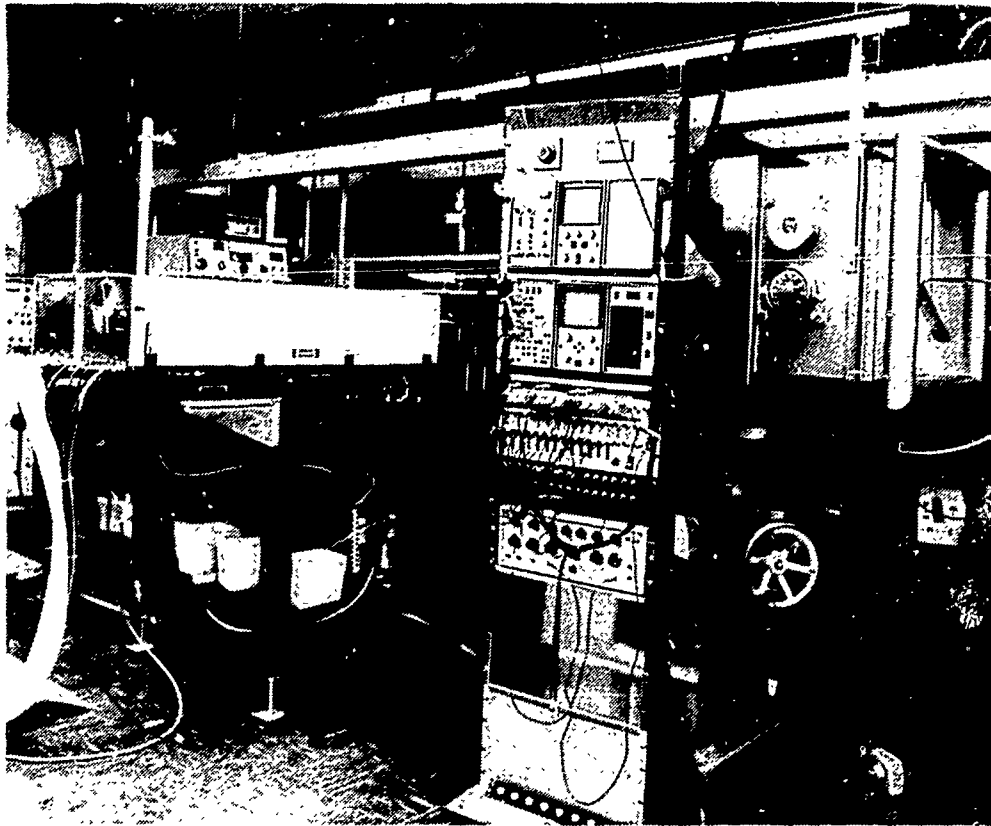


**Figure 2.** Photograph of the Raman system consisting of the dye laser, data acquisition electronics, and the flow tunnel.

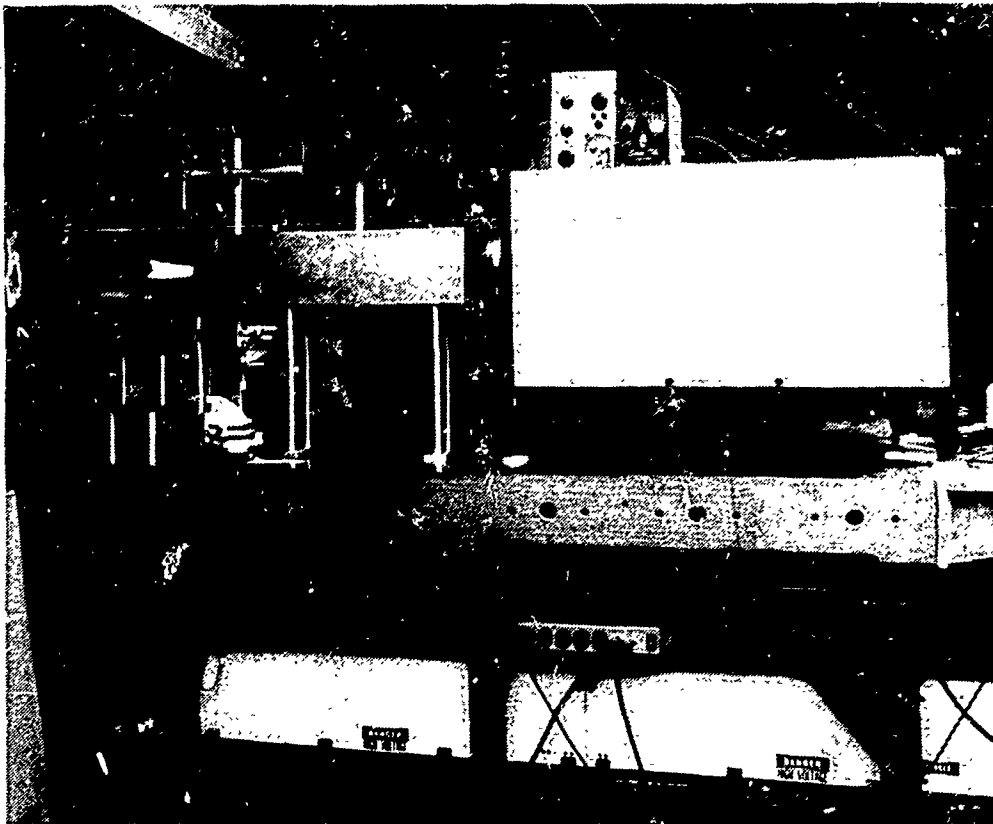


Figure 3. Photograph showing the spectrometer and the PMT housing box.  
The bluff-body has a blockage of 5%.

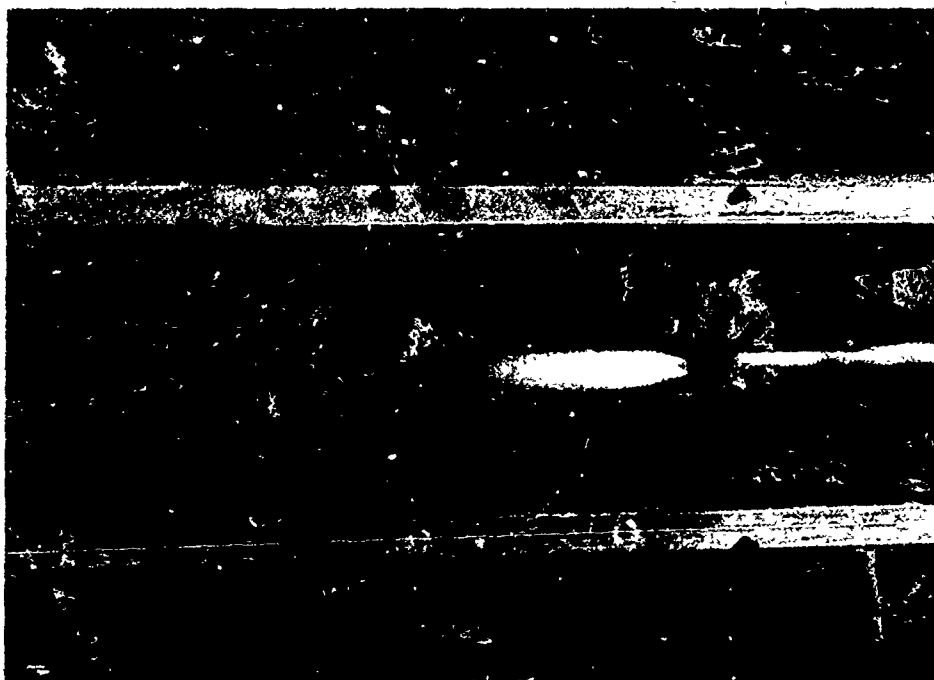


Figure 4. The bluff-body stabilized  $\text{CO}/\text{H}_2/\text{N}_2$  flame.



Figure 5. The bluff-body stabilized methane flame.

to be from soot precursors and other higher hydrocarbons. Profiles suggested that the laser-induced fluorescence was fairly broadband and contaminated all Raman channels, but surprisingly was negligible in the Rayleigh channel. An additional problem encountered in the application of Raman to this flame is the crosstalk between CH and other Raman channels, primarily  $O_2$ . For the 488.0 nm excitation used here, the Raman interference in the major species was insignificant.

To account for these two additional sources of contamination in the signals, the system as well as calibration procedures were significantly modified in the following manner. Since the laser-induced incandescence/fluorescence interference is fairly broadband, additional photomultiplier tubes were installed in two Raman-free regions of the spectra to monitor the laser-induced fluorescence on a shot-to-shot basis. Figure 6 shows the location of these two additional PMTs in the box relative to the existing photomultiplier tube locations. The new PMTs, termed F1 and F2 respectively, were located at 540 nm (between  $O_2$  and  $CO_2$ ) and at 590 nm (between  $CH_4$  and  $H_2O$ ) respectively. These two signals were found to correlate very well with each other and with all other Raman signals, so that in the calibration procedures used eventually, the use of F1 was found to be sufficient to allow corrections in all other channels. Since space was severely limited in the PMT housing box, the new PMTs were mounted remotely with a fibre optic bundle connecting the slit exits to the cathodes of the PMTs.

The calibration procedure used to correct for laser induced fluorescence is similar to that used by Dibble et al (1987, 1990). To facilitate daily calibrations, a 38.0 mm dia. honeycomb burner was built to provide laminar diffusion flames of  $CH_4$  and CO stabilized at the burner end. The burner had flame arrestors and flow straighteners in it and resulted in a smooth thin laminar flame which was visibly sooty and yellow at the downstream end, but contained enough soot precursors and laser-induced fluorescence at the upstream end to allow calibrations. The amount of soot and the color of the flame could be easily controlled by varying the ratio of  $CH_4$  to CO in the laminar flame. Figures 7 and 8 present profiles of Raman data for major species obtained 10 mm downstream of the burner exit in a laminar  $CH_4$ /CO (70%) flame. Measured laser-induced fluorescence signals monitored via channel F1 are also plotted. On the each side of the flame contamination of Raman signals is observed in all major species as evident by the "bumps" in the raw data profiles. The shape of the bump corresponds to the shape of the F1 signal for all channels.

Additional tests showed that the magnitude of the bump also increased linearly with the amount of soot in the flame, and with increased F1. For major species such as  $N_2$ ,  $CH_4$ , and CO the contamination due to laser-induced fluorescence can be readily accounted for because they are expected to decay monotonically through the flamefront. The situation for  $O_2$ , and product species such as  $CO_2$  and  $H_2O$ , is more complicated.  $O_2$  is also contaminated by cross-talk from the  $CH_4$  channel. The product species  $CO_2$  and  $H_2O$  peak somewhere in the flamefront, where F1 also peaks.

The calibration factors to correct for fluorescence in all channels were obtained by iteration. First the raw data were used (without any correction factors) to calculate temperature (using the sum of mole fraction method) and mole fraction of major species. The calculated results were plotted in mixture fraction space, and compared with equilibrium and counterflow laminar diffusion flame calculations for methane in air under assumed values of stretch [Chen et al. (1989)]. Figures 9 to 11 show typical results. The effect of contamination caused by fluorescence is clearly evident from the kinks in the measured profiles, particularly in the fuel-rich regions of the flame. The next step in the process is to estimate correction factors for each of the major species ( $CO_2$ ,  $O_2$ , CO,  $H_2O$ ,  $H_2$ ,  $N_2$ ) based on the raw data (Figures 7 and 8). Then we subtract a component of the Raman signal equal to the product of the correction factor for species "i" and the value of F1:

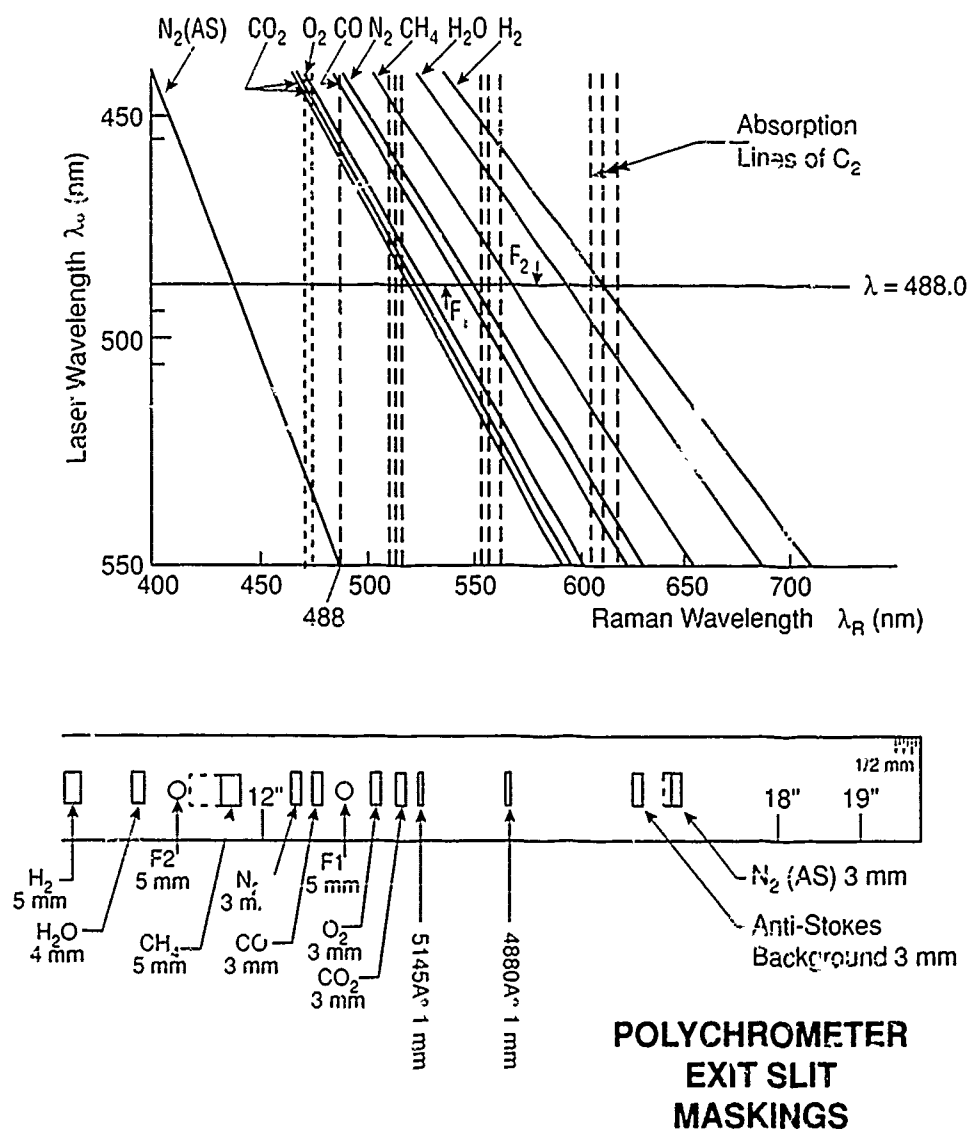


Figure 6. Schematic showing the location of the two additional photomultiplier tubes (F1 and F2) used to monitor the laser-induced fluorescence relative to other Raman channels in the wavelength space.

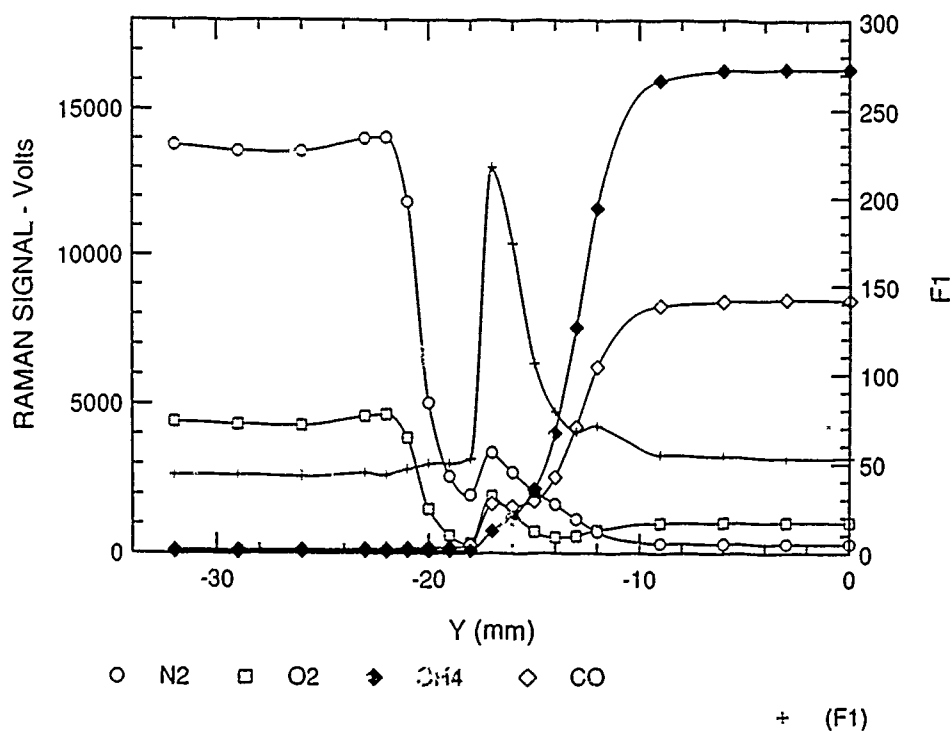


Figure 7. Raw Raman data (mean profiles) for N<sub>2</sub>, O<sub>2</sub>, CH<sub>4</sub>, and CO at  $x = 10$  mm, in a laminar diffusion CH<sub>4</sub>/CO (70%) flame.

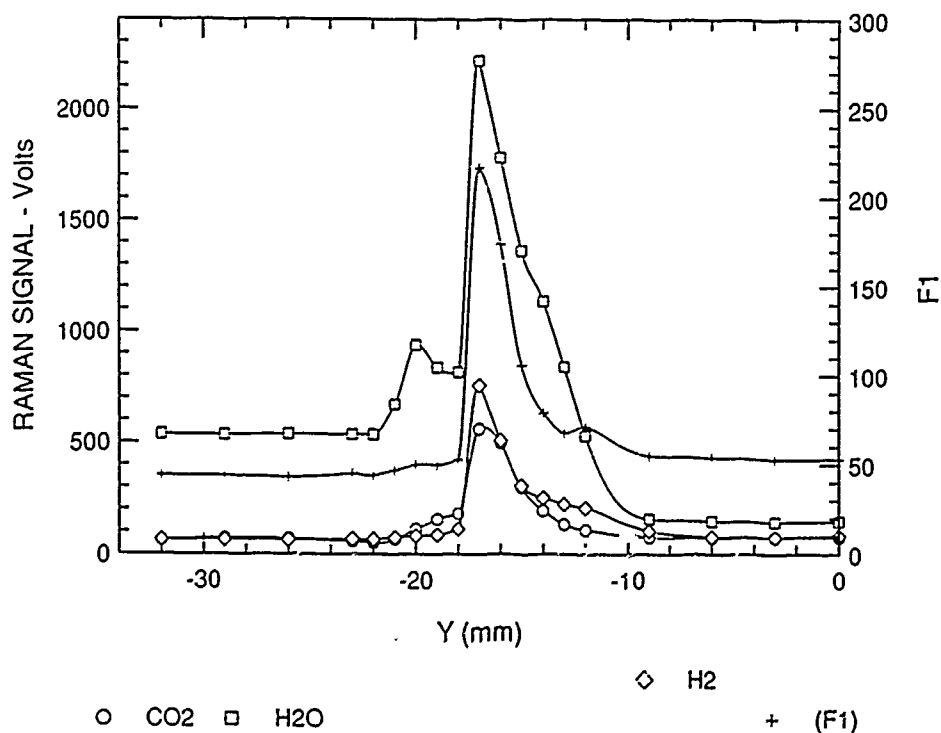


Figure 8. Raw Raman data (mean profiles) for CO<sub>2</sub>, H<sub>2</sub>O, and H<sub>2</sub> at  $x = 10$  mm, in a laminar diffusion CH<sub>4</sub>/CO (70%) flame.

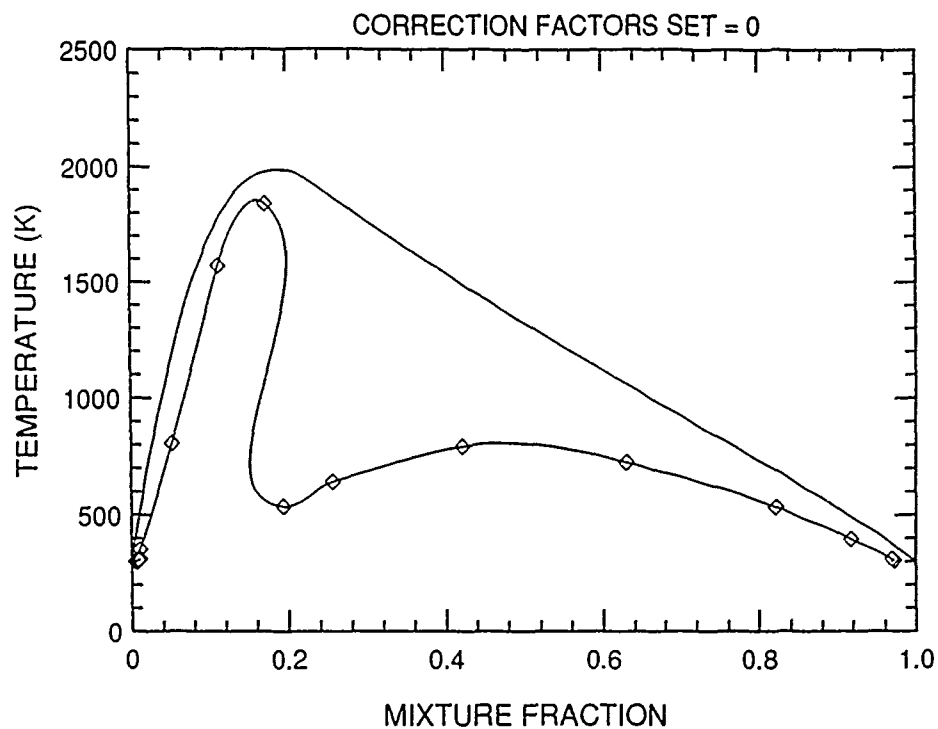


Figure 9. Comparison of reduced Raman data with laminar counterflow diffusion flame calculation with correction factors for fluorescence set to zero: Temperature.

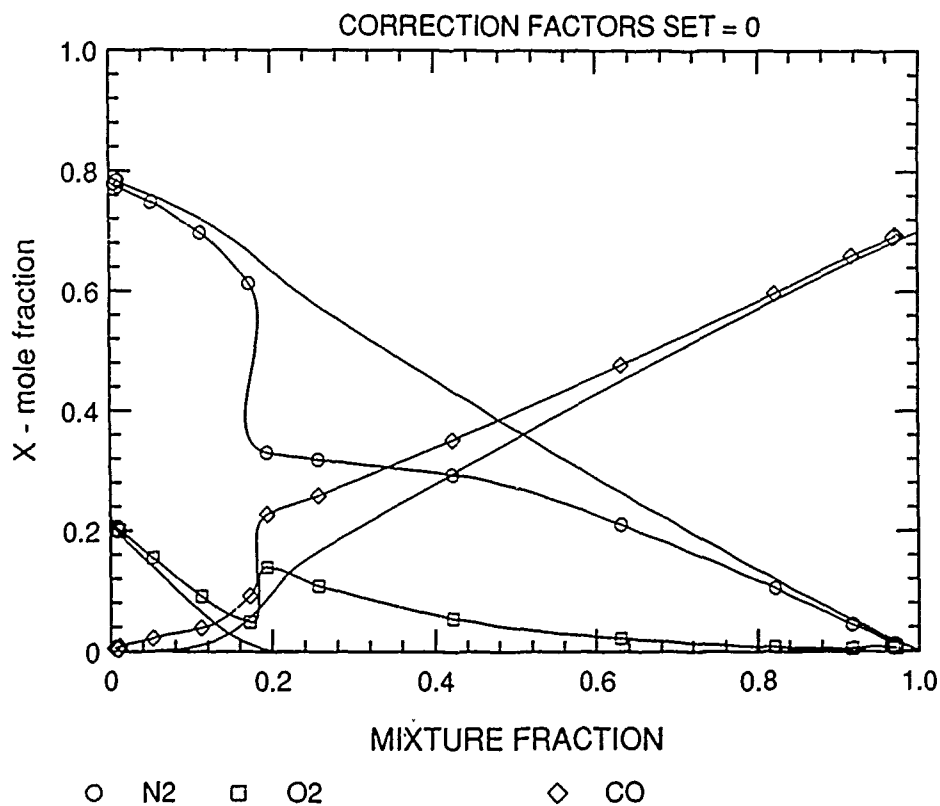


Figure 10. Comparison of reduced Raman data with laminar counterflow diffusion flame calculation with correction factors for fluorescence set to zero:  $N_2$ ,  $O_2$ , and CO

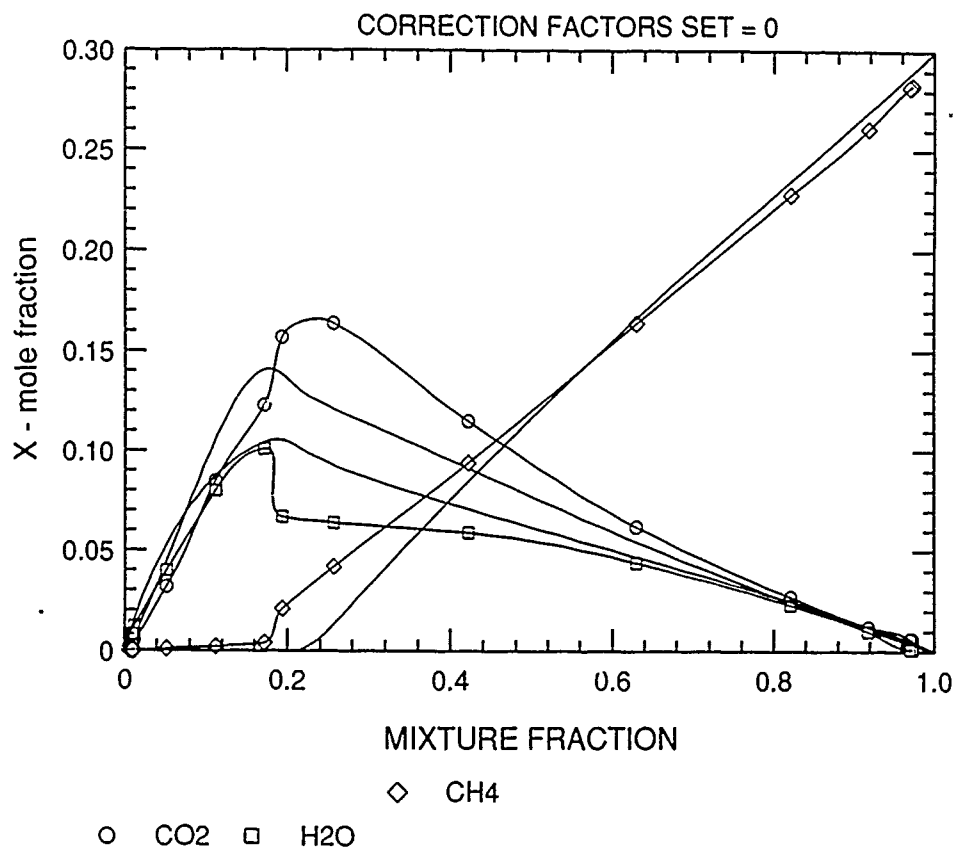


Figure 11. Comparison of reduced Raman data with laminar counterflow diffusion flame calculation with correction factors for fluorescence set to zero: CO<sub>2</sub>, H<sub>2</sub>, and CH<sub>4</sub>.



$$(RS_c)_i = (RS_{uc})_i - (CF)_i \times (FS)_{F1} \quad (2)$$

where  $RS_c$  refers to the corrected Raman signal,  $RS_{uc}$  refers to the uncorrected Raman signal,  $CF$  is the correction factor, and  $FS$  refers to the Fluorescence signal measured in photomultiplier tube  $F1$ . Using the estimated correction factors and Eq. (2), the calculated temperature and mole fraction profiles are then compared with the predicted values. The process is iterated to convergence. Figures 12 to 14 show the end result of one such process where the inclusion of correction factors have resulted in data agreeing fairly well with the predicted laminar flamelet calculations. An implicit assumption in this calibration procedure is that the flames are laminar and have very limited amount of stretch such that they do not have any nonequilibrium effects. Predicted values for the  $CH_4$ -containing flames were obtained for different assumed stretch rates [Chen et al. (1989)]. The profiles shown in Figures 7 to 14 were obtained for an assumed stretch of 5/s and did not depend strongly on this assumed value.

Once the correction factors were obtained they were kept constant for reduction of all the turbulent flame data. More sophisticated methods using linear matrix manipulation and artificial intelligence codes are being pursued elsewhere [Dibble et al. (1990)]. Experience has shown that this iteration process can be accelerated by "educated guesses." The calibration procedures were repeated before and after each set of measurements.

## 2.3 Discussion of Data

### (a) $CO/H_2/N_2$ Flame

The fuel consists of a mixture of 27.5%  $CO$ / 32.3%  $H_2$ / 40.2%  $N_2$ , a medium Btu gas. The experimental results are compared with calculations in Section 2.5; here only qualitative observations are made. The data showed significant nonequilibrium chemistry effects. However, even in the high shear region in the neck of the flame no significant localized extinction was observed because of the high hydrogen content of the fuel. To study a flame with significant extent of local extinction it was decided to switch to pure methane, whose slower kinetics are expected to increase the probability of localized extinction. The results of Masri et. al. (1987, 1988, 1989) and Dibble et al. (1987) support this expectation, but Bilger (1989) points out that the reason may be chemical rather than aerodynamic.

### (b) Pure Methane Flame

The  $CH_4$  flame used in this study (Figure 5) is at a Reynolds number of 12,000, based on the jet diameter of 3.175 mm and jet exit velocity of 62.5 m/s. Radial profiles of temperature and mole fractions of major species were measured at axial locations of  $x/d = 5, 10, 20, 30, 50$  and 70 and at the centerline. The data presented here were all corrected using the factors obtained by the procedure of Section 2.2.2. To help visualize the results better, a schematic of bluff-body stabilized flame outlining the various regions of interest is shown in Figure 15.

Figures 16 to 19 present scattergrams of temperature vs. mixture fraction in various regions of the flame. In the recirculation zone ( $x/d = 5$ ), most of the data in the  $T-\xi$  space lies on the rich side close to the profile obtained with  $CH_4$  flames at assumed stretch of 5/s. As Figure 17 shows, the predicted temperature profiles for stretch of 5/s and 300/s are quite close to each other. In the neck region ( $x/d = 10 - 20$ ) shown in Figure 17 the scattergram is clearly bimodal. A significant number of points correspond to rich equilibrated eddies, while a significant number of eddies have fuel-air mixture fraction values close to stoichiometric but significantly lower temperature. These eddies manifest

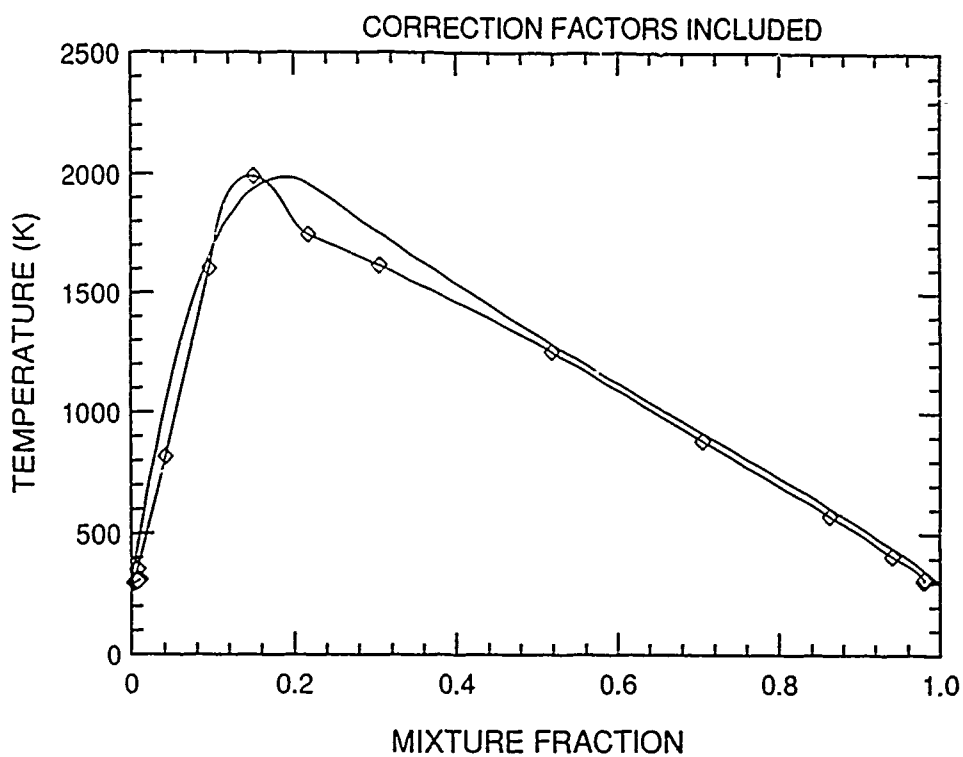


Figure 12. Comparison of fluorescence-corrected Raman data, corresponding to Fig. 9, with laminar counterflow diffusion flame calculation.

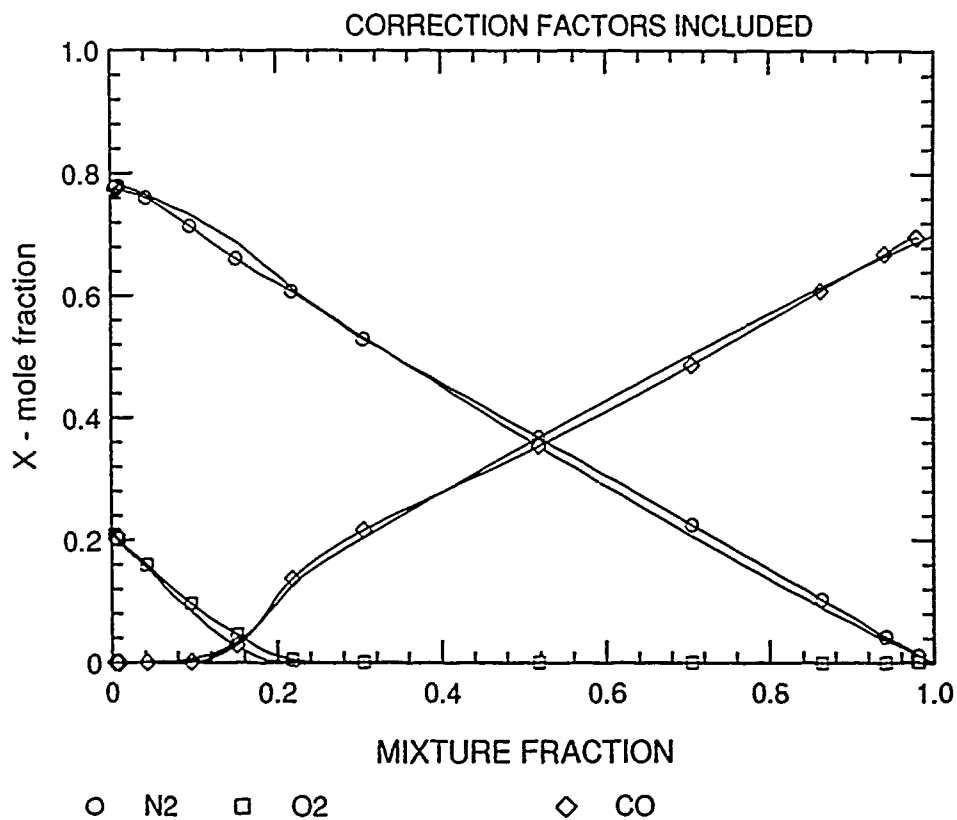


Figure 13. Comparison of fluorescence-corrected Raman data, corresponding to Fig. 10, with laminar counterflow diffusion flame calculation.

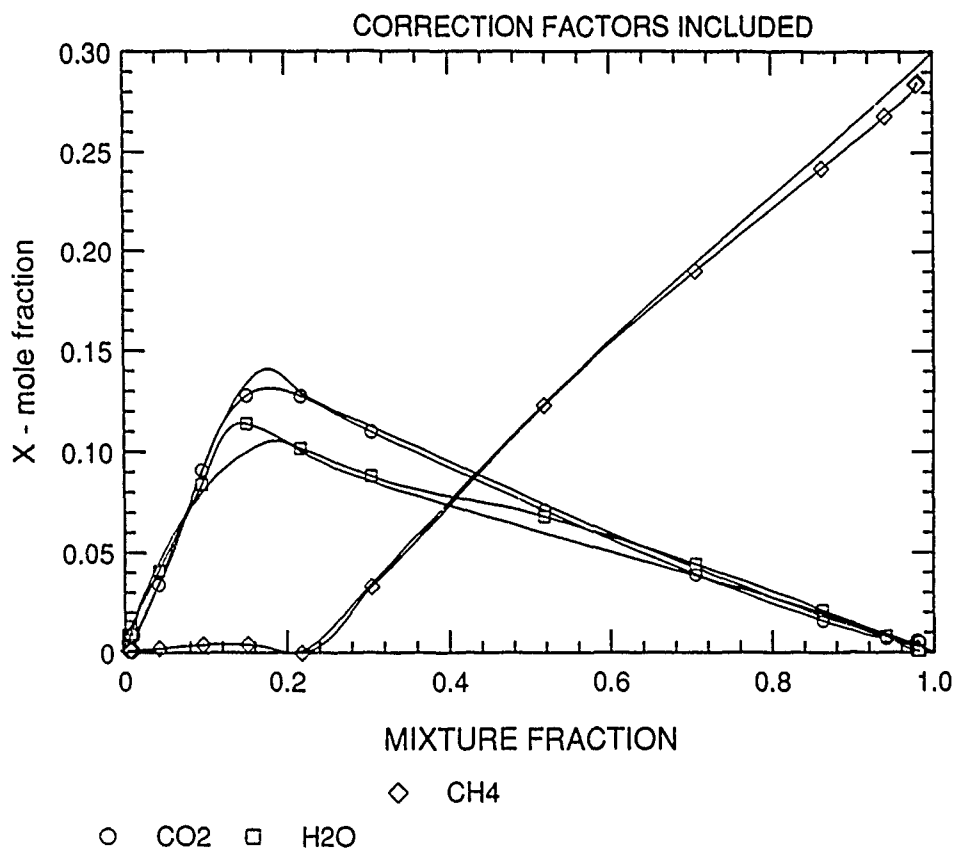


Figure 14. Comparison of fluorescence-corrected Raman data, corresponding to Fig. 11, with laminar counterflow diffusion flame calculation.

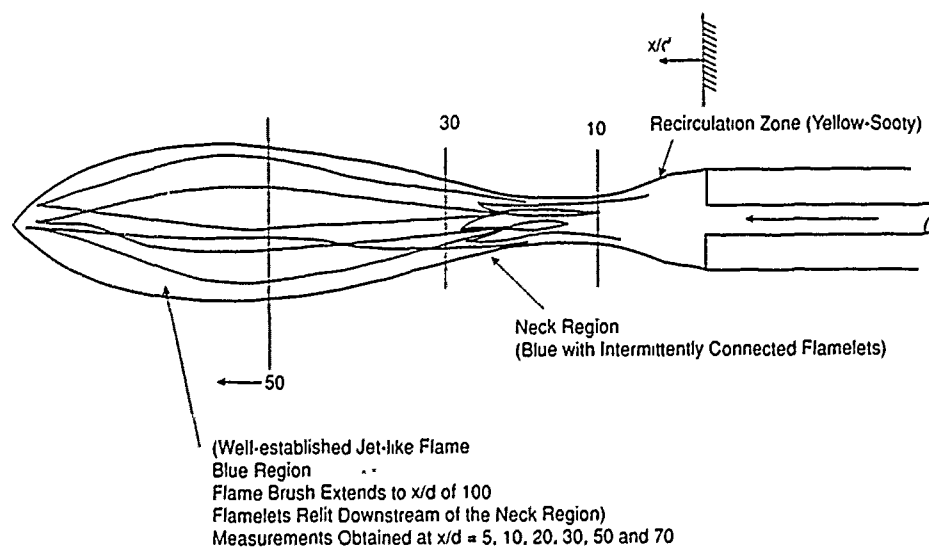


Figure 15. Schematic of various regions of the bluff-body stabilized methane flame indicating various regions of interest.

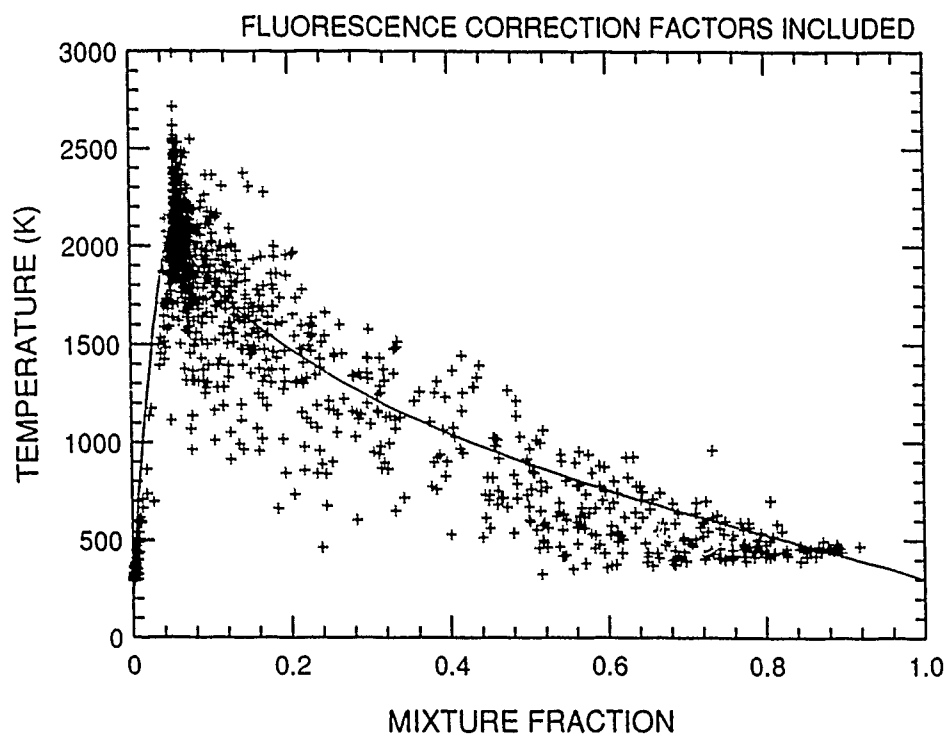


Figure 16. Scattergram of temperature vs. mixture fraction at  $x/d = 5$ .

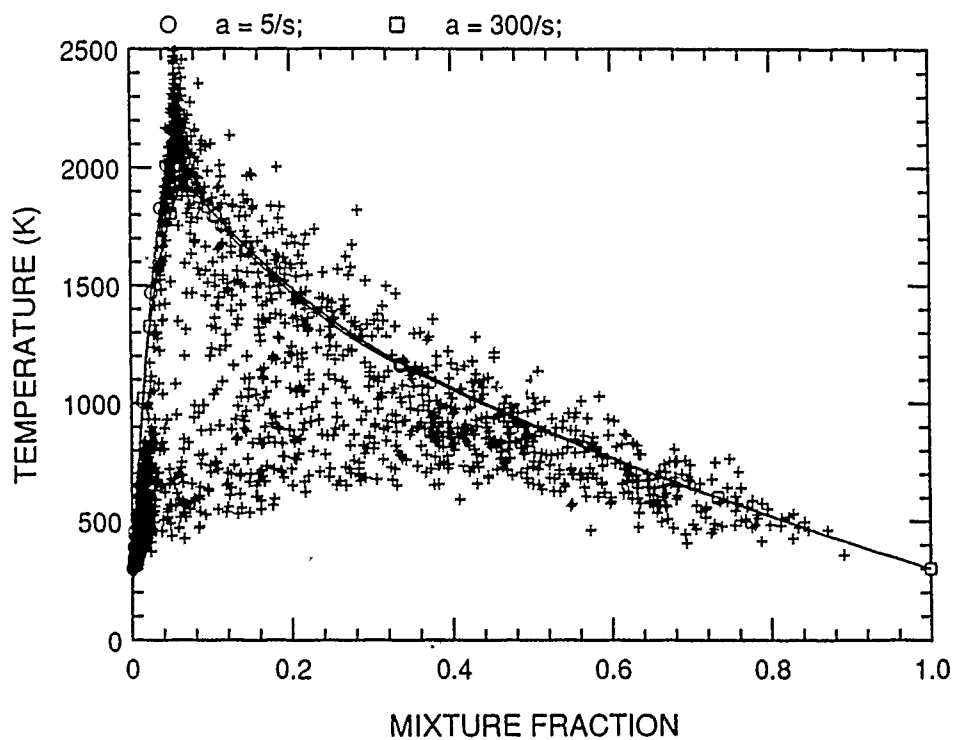


Figure 17. Scattergram of temperature vs. mixture fraction in the narrow neck region of the flame ( $x/d = 10$  and  $20$ ).

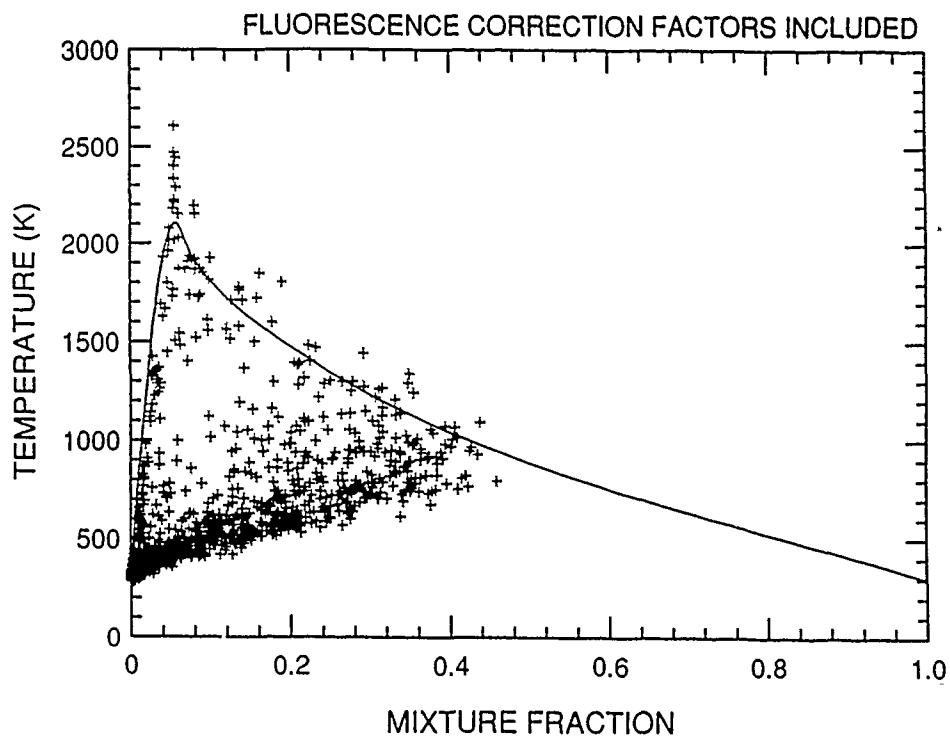


Figure 18. Scattergram of temperature vs. mixture fraction at  $x/d = 30$ .

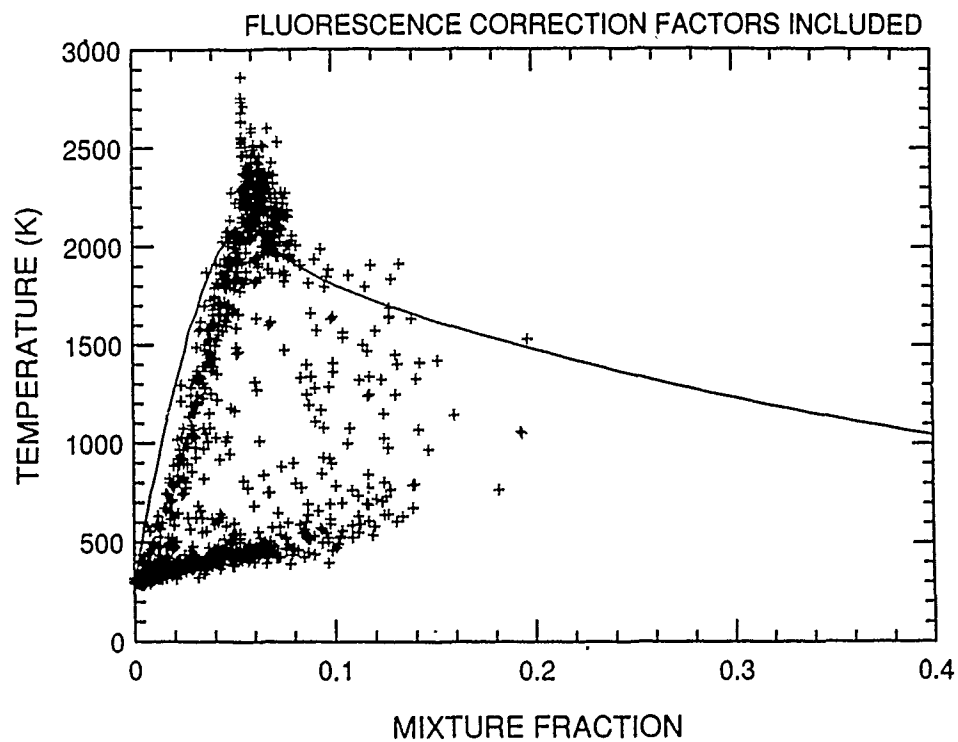


Figure 19. Scattergram of temperature vs. mixture fraction at  $x/d = 70$ .

localized extinction caused by high shear in the neck region of the flame (where the recirculation zone ends) and the slow kinetics of methane. Whether these eddies represent fuel-air mixture that became extinguished because of high strain or eddies that were never ignited is difficult to determine based on this data. Joint measurements of Raman and radical species as OH are needed to clarify this issue. At  $x/d = 30$  (Figure 18), there are still a number of locally extinguished eddies, but the fuel-air mixture is leaner and there are some eddies which have re-ignited (on the lean side) and have attained temperatures close to those of strained flamelets. As more eddies reach the low shear region downstream of the neck, they appear to re-ignite and equilibrate to high temperatures, as shown by data on the lean side in Figures 18 and 19. There are some extinguished eddies at  $x/d = 18$  as well, but their number is reduced significantly. The physical picture that emerges from the data of Figures 16-19 is that of a recirculation zone (which keeps the flame anchored) connected to a jet-like region by a fairly long but narrow neck region of high shear with a significant number of locally extinguished eddies. In the neck region the flame is intermittently connected at these high Reynold numbers.

The scattergrams of mass fractions of major species in mixture fraction space in the neck region of the flame is shown in Figures 20 to 24 for  $O_2$ ,  $N_2$ ,  $CH_4$ ,  $H_2O$ , and  $CO_2$ , respectively. Laminar-opposed-flow flame calculations for  $\alpha$  of 5/s and 300/s are also plotted in the figure for reference. All data has been included in all the scattergrams. The results for  $O_2$ ,  $CH_4$  and  $N_2$  distinctly show bimodal behavior between frozen values and equilibrated values, whereas the data for  $CO_2$  is widespread possibly because of contamination. It is to be noted that  $CO_2$  and CO species are most difficult to measure because of their relatively low signal values.

Finally, Figures 25 to 29 show the measured profile of temperature and major species across the burner at  $x/d = 10$ . The temperature has been calculated based on two methods, viz., sum of mole fractions and Rayleigh scattering. The Rayleigh signal is not contaminated by laser-induced fluorescence and therefore provides an independent temperature measurement. Figures 25 and 26 show that the temperature measurements obtained by the two methods agree fairly well for both mean and rms values. The mean temperature peaks in the recirculation zone and has a minimum in the core jet. The rms temperature values peak in the shear layer between the recirculation zone and the co-flowing air. The profiles for major species, Figures 27-29, show reasonable trends. There is some entrainment of air in the core of the main jet though the oxygen is depleted there. Profiles of CO and  $H_2$ , which are intermediates, peak in the recirculation zone. The mean values are very low. It should be recalled that  $x/d = 10$  corresponds to the narrow neck region containing a significant number of highly strained eddies. Finally, the products  $CO_2$ , and  $H_2O$  both peak in the recirculation zone and are fairly flat there. Detailed comparison of data with model predictions in the  $CH_4$  flame is in progress.

## 2.4 Governing Equations and Models

This subsection describes the physical submodels and the computational algorithm used to predict the bluff-body stabilized  $CO/H_2/N_2$  flame.

### 2.4.1 Navier-Stokes Equations

The governing equations for the flow of a multicomponent reacting gas are

- Continuity:

$$\frac{\partial \rho}{\partial t} + \frac{\partial}{\partial x_i} (\rho u_i) = 0 \quad (3)$$

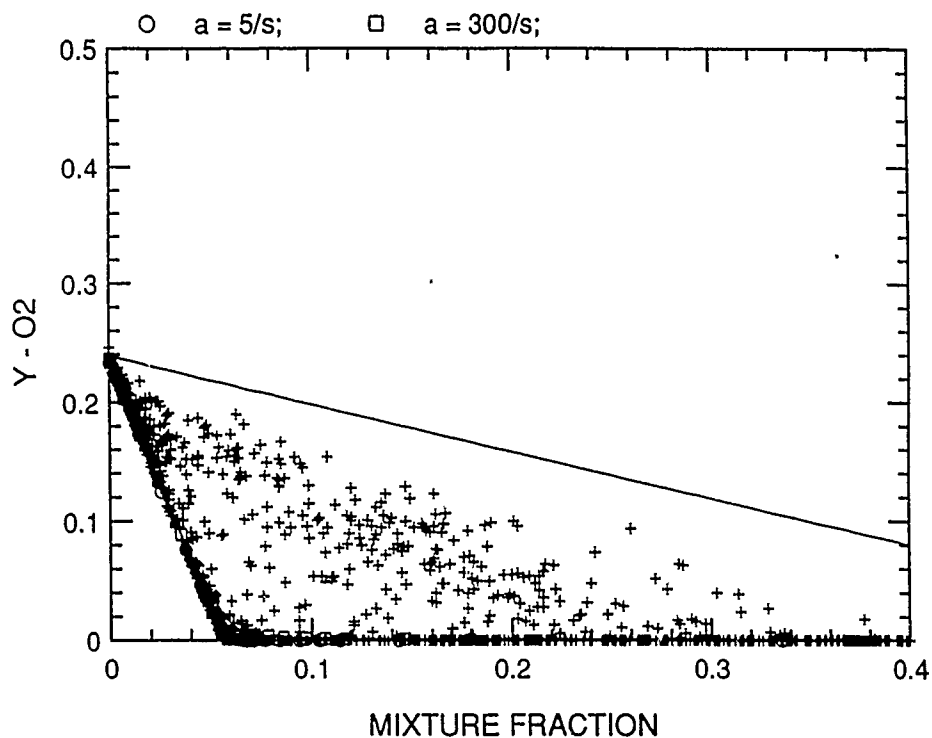


Figure 20. Scattergram of mass-fraction of  $O_2$  vs. mixture fraction in the narrow neck region of the flame ( $x/d = 20$ ). Profiles obtained from laminar flamelet calculations for  $\alpha$  of 5/s and 300/s are also shown.

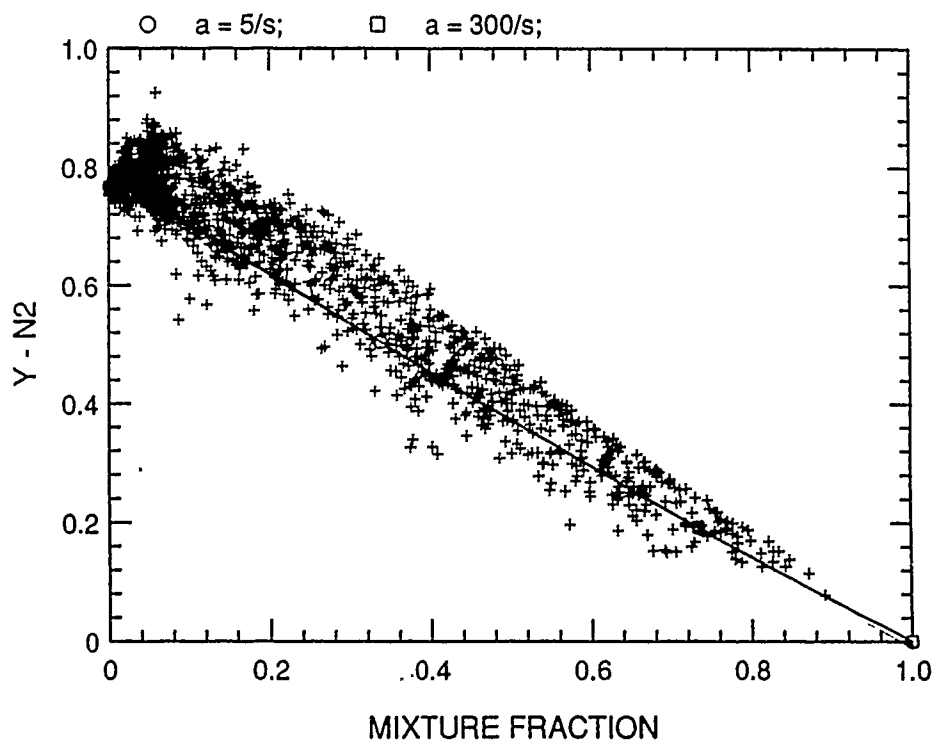


Figure 21. Scattergram of mass-fraction of  $N_2$  vs. mixture fraction in the narrow neck region of the flame ( $x/d = 10$  and 20). Profiles obtained from laminar flamelet calculations for  $\alpha$  of 5/s and 300/s are also shown.

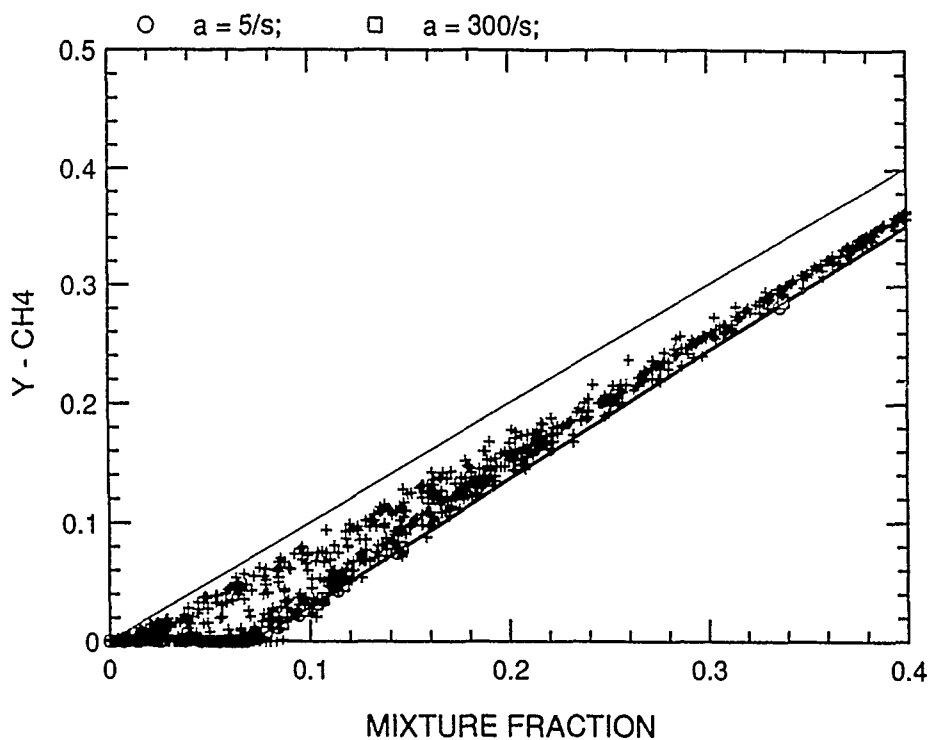


Figure 22. Scattergram of mass-fraction of  $\text{CH}_4$  vs. mixture fraction in the narrow neck region of the flame ( $x/d = 10$  and  $20$ ). Profiles obtained from laminar flamelet calculations for  $\alpha$  of  $5/\text{s}$  and  $300/\text{s}$  are also shown.

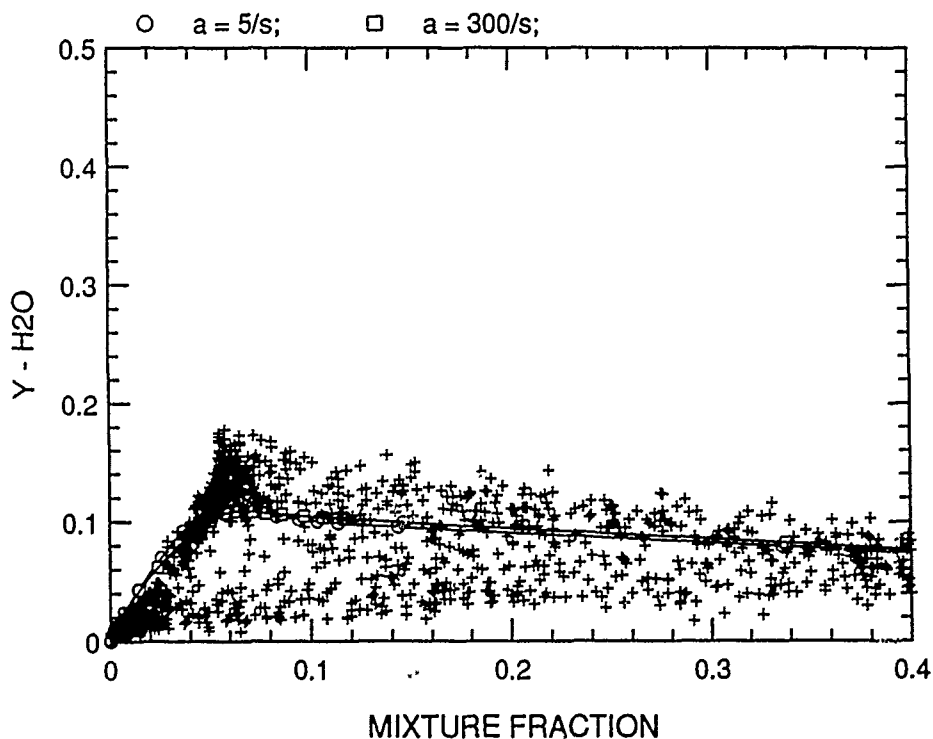


Figure 23. Scattergram of mass-fraction of  $\text{H}_2\text{O}$  vs. mixture fraction in the narrow neck region of the flame ( $x/d = 10$  and  $20$ ). Profiles obtained from laminar flamelet calculations for  $\alpha$  of  $5/\text{s}$  and  $300/\text{s}$  are also shown.



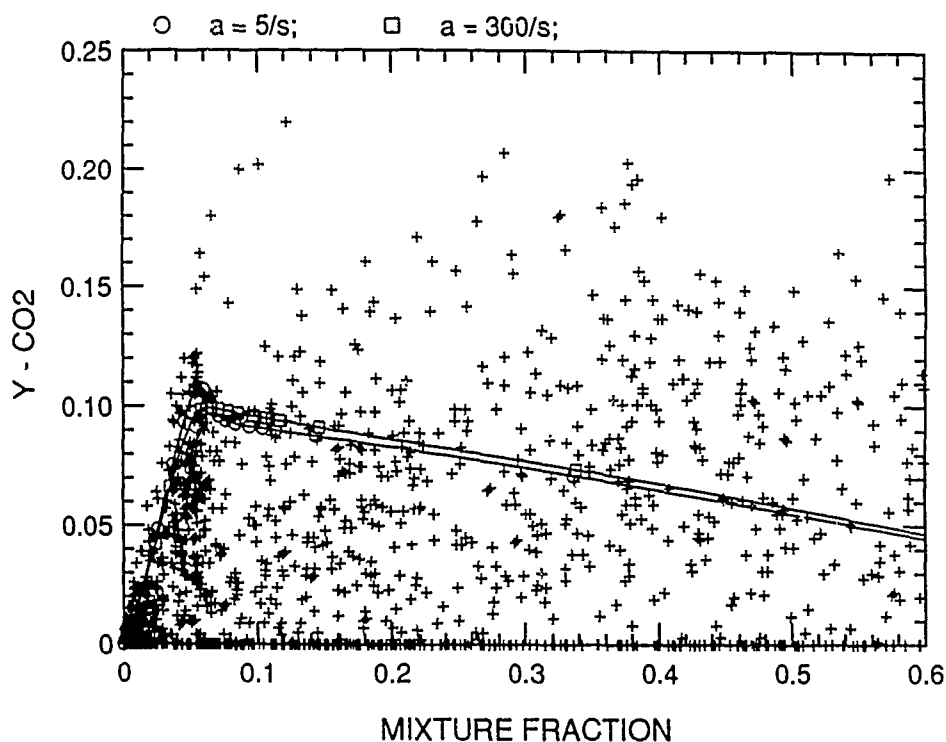


Figure 24. Scattergram of mass-fraction of  $\text{CO}_2$  vs. mixture fraction in the narrow neck region of the flame ( $x/d = 20$ ). Profiles obtained from laminar flamelet calculations for  $\alpha$  of 5/s and 300/s are also shown.

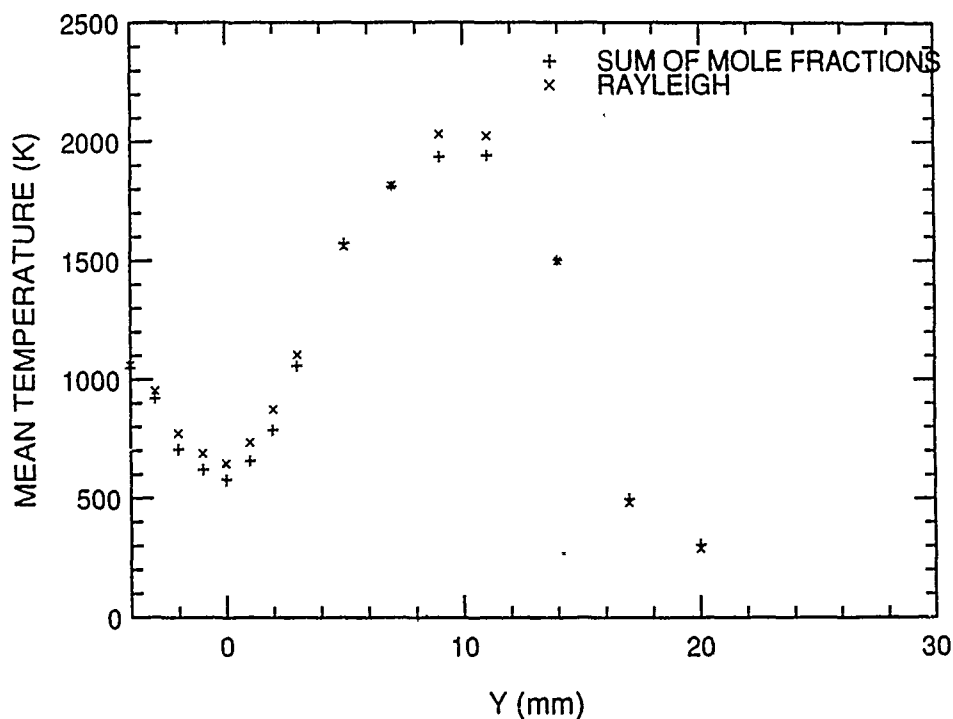


Figure 25. Profile of mean temperature across the burner at  $x/d = 10$ . Data calculated using sum of mole fraction method and Rayleigh scattering are also shown.

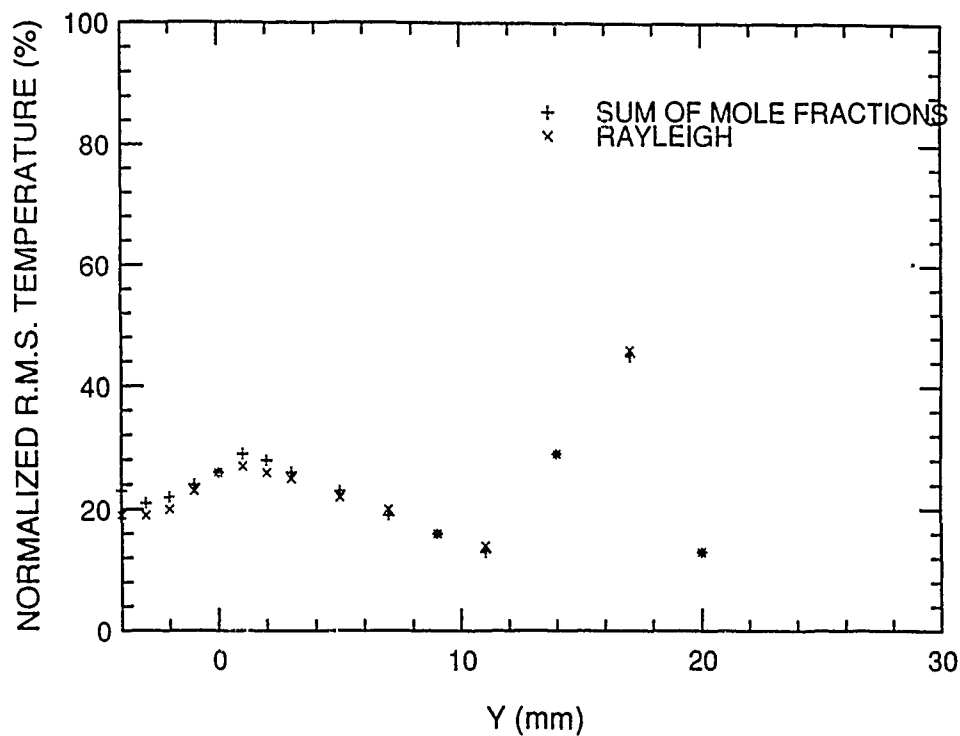


Figure 26. Profile of normalized r.m.s. temperature across the burner at  $x/d = 10$ . Data calculated using sum of mole fraction method and Rayleigh scattering are also shown.

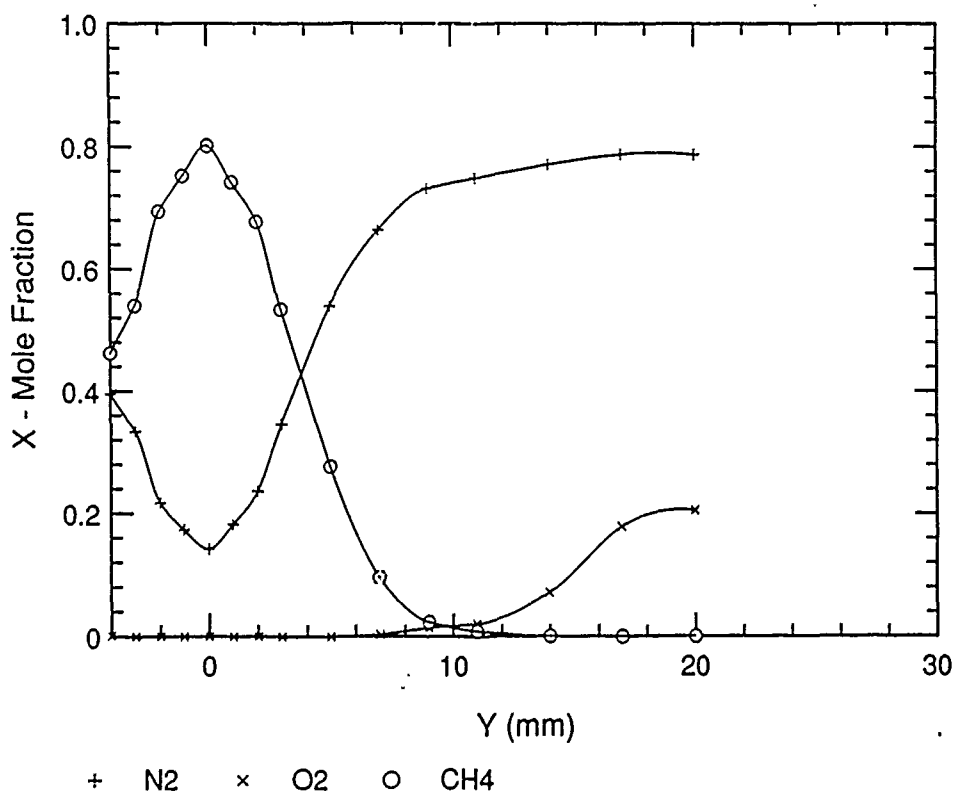


Figure 27. Measured mean profile of  $O_2$ ,  $N_2$ , and  $CH_4$  across the burner at  $x/d = 10$ .

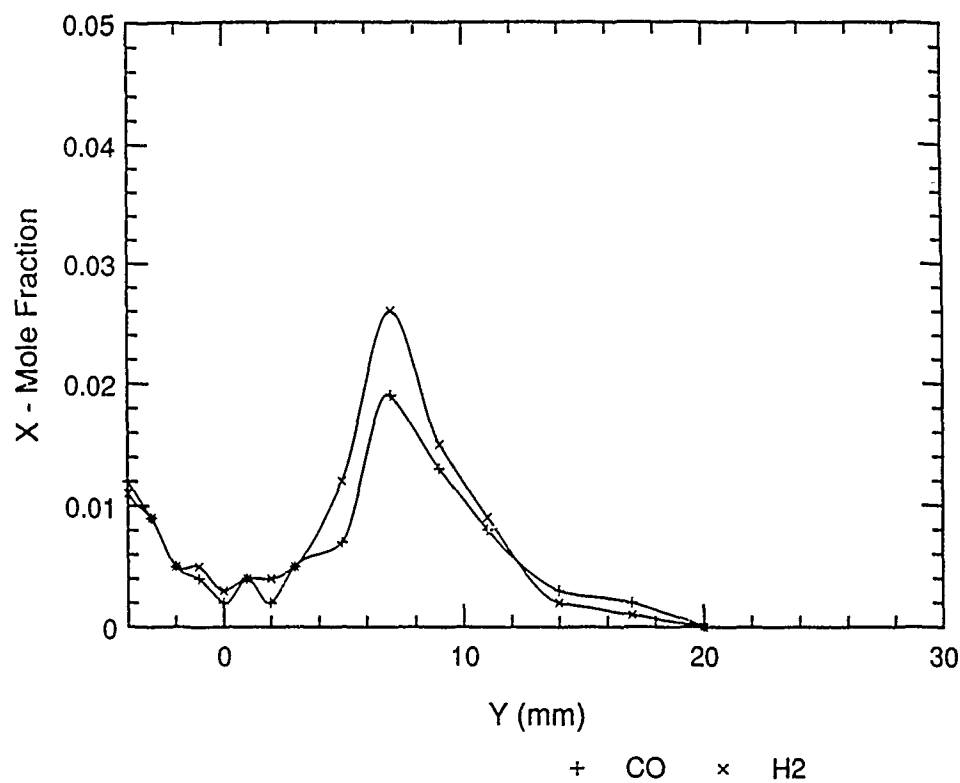


Figure 28. Measured mean profile of CO and H<sub>2</sub> across the burner at  $x/d = 10$ .

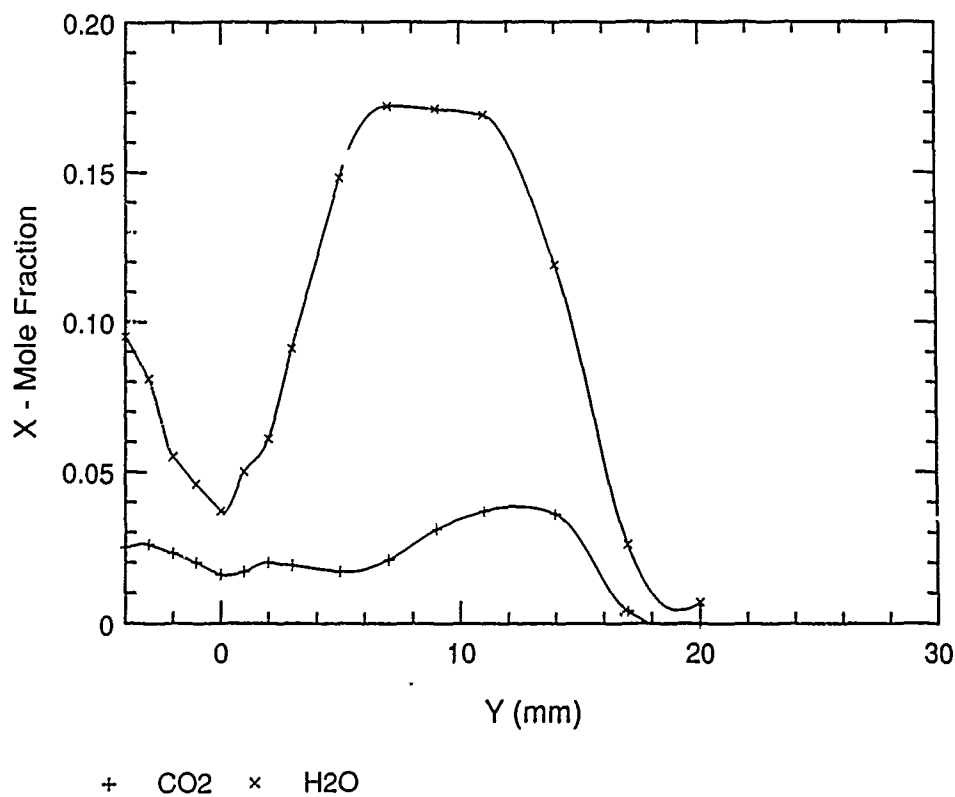


Figure 29. Measured mean profile of CO<sub>2</sub> and H<sub>2</sub>O across the burner at  $x/d = 10$ .

- Momentum:

$$\frac{\partial}{\partial t} (\rho u_i) + \frac{\partial}{\partial x_j} (\rho u_i u_j) = - \frac{\partial p}{\partial x_i} + \frac{\partial}{\partial x_j} \left[ \mu \left( \frac{\partial u_i}{\partial x_j} + \frac{\partial u_j}{\partial x_i} - \frac{2}{3} \delta_{ij} \frac{\partial u_k}{\partial x_k} \right) \right] \quad (4)$$

- Species:

$$\frac{\partial}{\partial t} (\rho Y_s) + \frac{\partial}{\partial x_j} (\rho u_j Y_s) = \frac{\partial}{\partial x_j} \left[ \frac{\mu}{Sc} \frac{\partial Y_s}{\partial x_j} \right] + \dot{\rho} \dot{r}_s \quad (5)$$

- Enthalpy:

$$\frac{\partial}{\partial t} (\rho h) + \frac{\partial}{\partial x_j} (\rho u_j h) = \frac{\partial p}{\partial t} + \frac{\partial}{\partial x_j} \left[ \frac{\mu}{Pr} \frac{\partial h}{\partial x_j} + \frac{\mu}{Pr} \left( \frac{Pr}{Sc} - 1 \right) \sum_{s=1}^N h_s \frac{\partial Y_s}{\partial x_j} \right] \quad (6)$$

These equations are supplemented by the equation of state

$$\rho = p / [RT \sum_{s=1}^N (Y_s / M_s)] \quad (7a)$$

and the thermodynamic data relating the enthalpy of the mixture and of each species to temperature

$$h = \sum_{s=1}^N Y_s h_s(T) \quad (7b)$$

in which the species enthalpy  $h_s(T)$  is known.

Turbulent flows are characterized by a widely disparate set of length and time scales so that direct numerical solution would require a very fine discretization of space and time. Over a domain of length  $L$ , resolution down to the viscous length  $l_\mu$  would require on the order of  $L/l_\mu$  or  $Re$  number of mesh points in each direction; a similar argument holds for temporal resolution. Introduction of chemical time-scales further exacerbates the problem. Direct simulations are therefore not currently possible for Reynolds and Damköhler numbers of interest, and indeed may never be. Turbulence and turbulence-chemistry interaction models are therefore required.

#### 2.4.2 Averaged Equations and Closure

The most common computational approach in multidimensional turbulent flow is a conventional or density-weighted decomposition of the dependent variables followed by a closure model for the correlations. Since the Reynolds number is high in typical flows of interest here, conventional closures assume that molecular transport processes are overwhelmed by turbulent transport. For this reason, the molecular transport terms are dropped in Eqs. (3) to (6), which may eventually be written as follows:

- Momentum:

$$\frac{\partial}{\partial t} (\bar{\rho} \bar{u}_i) + \frac{\partial}{\partial x_j} (\bar{\rho} \bar{u}_j \bar{u}_i) = - \frac{\partial \bar{p}}{\partial x_i} + \frac{\partial \tau_{ij}}{\partial x_j} \quad (8a)$$

- Species:

$$\frac{\partial}{\partial t} (\bar{\rho} \bar{\phi}_s) + \frac{\partial}{\partial x_j} (\bar{\rho} \bar{u}_j \bar{\phi}_s) = - \frac{\partial \bar{j}_j}{\partial x_j} (s) + \bar{\rho} \bar{r}_s \quad (8b)$$

Here  $\phi_s$  ( $s = 1, N + 1$ ) represents all  $N$  species mass fractions and the total chemical-plus-sensible enthalpy.

The standard approach does not account for molecular mixing processes. Experiments in liquids, where the Schmidt number  $Sc$  is on the order of  $10^3$ , have indicated that molecular processes cannot really be ignored in mixing [Koochesfahani et al. (1985)]. Such processes are less important in turbulent mixing of gaseous species.

Closure is most often accomplished by the  $k$ - $\epsilon$  turbulence model [Launder and Spalding (1974)] with a wall-function treatment of the near-wall region. In the  $k$ - $\epsilon$  model, the turbulent eddy viscosity  $\mu_t$  is obtained on dimensional grounds from

$$\mu_t = C_\mu \bar{\rho} k^2 / \epsilon \quad (9)$$

where the turbulence kinetic energy ( $k$ ) and the dissipation rate ( $\epsilon$ ) are obtained from modeled transport equations

$$\bar{\rho} \bar{u}_j \frac{\partial k}{\partial x_j} = \frac{\partial}{\partial x_j} \left[ \left( \frac{\mu_t}{\sigma_k} + \mu \right) \frac{\partial k}{\partial x_j} \right] - \bar{\rho} \bar{u}''_i \bar{u}''_j \frac{\partial \bar{u}_i}{\partial x_j} - \frac{\mu_t}{\bar{\rho}} \frac{\partial \bar{p}}{\partial x_i} \frac{\partial \bar{p}}{\partial x_i} - \bar{\rho} \epsilon, \quad (10)$$

and

$$\bar{\rho} \bar{u}_j \frac{\partial \epsilon}{\partial x_j} = \frac{\partial}{\partial x_j} \left[ \left( \frac{\mu_t}{\sigma_\epsilon} + \mu \right) \frac{\partial \epsilon}{\partial x_j} \right] - C_1 \frac{\epsilon}{k} \left[ \bar{\rho} \bar{u}''_i \bar{u}''_j \frac{\partial \bar{u}_i}{\partial x_j} + \frac{\mu_t}{\bar{\rho}} \frac{\partial \bar{p}}{\partial x_i} \frac{\partial \bar{p}}{\partial x_i} \right] - C_2 \bar{\rho} \frac{\epsilon^2}{k} \quad (11)$$

The constants in these equations are taken as [Launder and Spalding (1974)]

$$C_\mu = 0.09, \quad C_1 = 1.44, \quad C_2 = 1.92; \quad (12)$$

with turbulent Schmidt numbers for  $k$  and  $\epsilon$

$$\sigma_k = 1.0, \quad \sigma_\epsilon = 1.30, \quad (13)$$

and for thermochemical scalar quantities

$$\sigma_t = 0.7 \quad (14)$$

The two-equation  $k-\epsilon$  model might be expected to work in flows where the Reynolds stresses can indeed be related solely to the local strain rate [Rodi (1980)]. If this is not so, it is necessary to account for convection, diffusion, and production/destruction of these stresses, e.g., Amano and Kodali (1984). A major advantage of jet flows is that the  $k-\epsilon$  class of models is more successful there than in recirculating flows. The  $k-\epsilon$  model is known to have deficiencies in flows with strong curvature [(Launder et al. (1984); Gibson, (1985)] and in strongly swirling flows [(Launder et al. (1984)] but is successful in jet-like flow at least as far as prediction of the mean profiles is concerned.

Despite reservations, the  $k-\epsilon$  model is used here. The long-term plan is to switch to the Monte-Carlo pdf transport model, which is closed in the sense of turbulence correlations.

We note that all models –  $k-\epsilon$ , second-order Reynolds stress/flux, and pdf transport – obtain length-scale information from the dissipation rate equation.

To compute the transport of a scalar in turbulent flow, it is necessary to calculate the rate at which the fluctuations in the scalar field decay. Most closure models assume that the time scale of scalar turbulence is proportional to that of the turbulent velocity field, usually characterized as  $q^2/\epsilon$ , where  $q^2$  is twice the kinematic kinetic energy of turbulence and  $\epsilon$  is the energy dissipation rate. That means the ratio between the velocity and the thermal time scales,  $R$  is a constant. Here  $R = (q^2/\epsilon)/(\phi^2/\epsilon_\phi)$ , where  $\phi$  designates a scalar variable.

### 2.4.3 Chemistry Model

The thermochemistry must be represented by as few variables as possible, so as to minimize the number of field equations. Unfortunately, even for the simplest hydrocarbons,  $\sim 50$  species and  $\sim 250$  reactions are involved. While these detailed chemical models can be run for one-dimensional laminar flames (either premixed or diffusion), their applicability to multidimensional flames is limited by computational size and cost. Application to turbulent flames places further restrictions on the schemes. Thus, there is a need for simplified yet reliable kinetic models.

The partial-equilibrium model is used here and is presented in the hierarchy which starts with fast chemistry.

#### Fast Chemistry:

The scalar set  $\phi_s$  of species mass fractions and mixture enthalpy can be reduced to a single conserved variable,  $\xi$ , called the "mixture fraction" [Bilger, in Libby and Williams (1980)], as follows. Defining the elemental mass fraction  $z_i$ , which is related to the species mass fraction  $Y_j$  by

$$z_i = \sum_{j=1}^N \mu_{ij} Y_j \quad i = 1, M \quad (15)$$

where  $\mu_{ij}$  is the mass of the  $i^{th}$  element per unit mass of the  $j^{th}$  species in a system of  $M$  elements and  $N$  species, and assuming equal diffusion coefficients, the transport equation for  $z_i$  is

$$\frac{\partial}{\partial x_j} (\rho z_j z_i) = \frac{\partial}{\partial x_j} (\rho D \frac{\partial z_i}{\partial x_j}) \quad i = 1, M \quad (16)$$

These elemental transport equations are homogeneous since elements are neither created nor destroyed in chemical reactions. Thus  $M$  transport equations result. With equal transport coefficients,  $z_i$  is also the total (chemical plus sensible) enthalpy which is conserved for the low Mach number flows

considered here; at high Mach numbers the mechanical energy  $u^2/2$  cannot be neglected, and a separate equation is needed for the enthalpy; likewise for nonadiabatic flames.

If further, as in the flows of interest here, there are two chemically distinct reactant streams (superscripts f for fuel and a for air), the mixture fraction  $\xi$  is defined as

$$\xi \equiv \frac{z_i - z_i^a}{z_i^f - z_i^a} \quad \text{for each } i \quad (17)$$

and varies between 0 and 1 throughout the flow.

The equation for  $\xi$  is then obtained from Eqs. (16) and (17).

$$\frac{\partial}{\partial x_j} (\rho u_j \xi) = \frac{\partial}{\partial x_j} (\rho \Gamma_\xi \frac{\partial \xi}{\partial x_j}) \quad (18)$$

and the boundary conditions are

$$\xi = 0 \quad \text{in stream } a \quad (19)$$

$$\xi = 1 \quad \text{in stream } f \quad (20)$$

This is a very popular approach [Jones and Whitelaw (1984)] because all of the scalar information is contained in the mixture fraction and can be recovered from Eq. (17) as

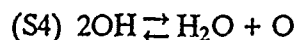
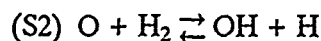
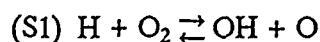
$$z_i = z_i^a + (z_i^f - z_i^a)\xi \quad (21)$$

and therefore only one transport equation, Eq. (18), has to be solved.

The atomic composition and total chemical plus sensible enthalpy is sufficient to determine the equilibrium composition of the gas, by minimization of the Gibbs free energy, for constant pressure systems.

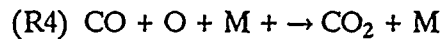
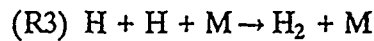
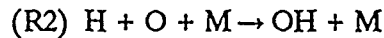
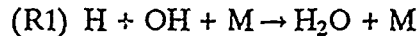
#### Partial-Equilibrium Model:

The partial-equilibrium model adds one more variable (besides  $\xi$ ) to track the progress of a pool of intermediate species as the system moves towards equilibrium. This approach has been developed for  $H_2$ -air [Janicka and Koliman (1979, 1982); Bilger (1980)], and  $CO/H_2/N_2$ -air systems [Correa et al. (1984)]. Two-variable schemes for  $H_2$ -air and  $CO/H_2/N_2$ -air systems may be described together. The kinetic mechanism adopted consists of fast shuffle reactions, which are considered to be fast enough for the participating species to be in partial equilibrium





and relatively slow three-body recombination reactions



Since the recombination reactions which govern the decay of the radical pool are slow, it is possible for the radicals to exist in concentrations larger than when in equilibrium. This phenomenon is referred to as radical overshoot or superequilibrium [Correa et al. (1984), Drake et al. (1984)].  $\text{HO}_2$  can be included in the scheme without difficulty.

The kinetic mechanism adopted here is simple so that the turbulence-chemistry interactions are not computationally prohibitive. It attempts to account for radical overshoot and post-flame burnout. Janicka and Kollman (1979) used the scheme without reactions (S5) and (R4) in their studies of turbulent hydrogen flames. Warnatz (1981) demonstrated its validity in laminar premixed hydrogen flames for temperatures above 1500 K. In earlier studies, Kaskan (1959) and Fenimore and Moore (1974) used the same shuffle reactions to describe the combustion of carbon monoxide in laminar flames. Bilger and Starner (1983) also discussed the merits of this kinetic scheme and concluded that it would be applicable at the higher temperatures. At high pressures (well above 10 atm), the rates of the shuffle and recombination reactions approach each other and the scheme ceases to be useful.

To reduce the number of conservation equations to be considered, a linear combination of concentrations is used. For this system, this leads to the combined variable  $Y_{H_2}^*$

$$Y_{H_2}^* = Y_{H_2} + \frac{1}{2} \frac{M_{H_2}}{M_{OH}} Y_{OH} + \frac{M_{H_2}}{M_O} Y_O + \frac{3}{2} \frac{M_{H_2}}{M_H} Y_H + \frac{M_{H_2}}{M_{CO}} Y_{CO}. \quad (22)$$

The formation rate of this variable becomes independent of the shuffle reactions:

$$\dot{w}_{H_2}^* = -2 M_{H_2} (\dot{w}_{R1} + \dot{w}_{R2} + \dot{w}_{R3}) \quad (23)$$

Eleven quantities are required to describe the instantaneous state of the system. nine species concentrations ( $\text{O}_2$ ,  $\text{H}_2$ ,  $\text{N}_2$ ,  $\text{CO}$ ,  $\text{CO}_2$ ,  $\text{H}_2\text{O}$ ,  $\text{O}$ ,  $\text{H}$ ,  $\text{OH}$ ), the density and the temperature. These can all be related to just two variables as shown next.

The variable  $Y_{H_2}^*$  varies between its frozen and equilibrium values leading to the definition of the reaction progress variable  $\eta$ :

$$\eta \equiv \frac{Y_{H_2}^* - Y_{H_2}^{*u}}{Y_{H_2}^{*e} - Y_{H_2}^{*u}} \quad (24)$$

Specification of  $\xi$  amounts to five equations from the definition Eq. (17), while four more independent equations are obtained from partial equilibrium of the radical pool; specification of  $\eta$  and the equation of state complete the set of nonlinear algebraic equations for the description of the instantaneous thermochemical state. Solution of these equations gives a table of concentrations,



temperature, and density for each  $\xi$  and  $\eta$ . Representative results are shown in Figure 30. The maximum temperature of  $\sim 2170$  K occurs at the stoichiometric mixture fraction  $\xi_s \approx 0.33$ , in equilibrium  $\eta = 1.0$ . The temperature decreases as  $\eta$  decreases below the equilibrium value of unity, while OH shows the expected superequilibrium peak. These results are stored in digitized form for use in flow calculations.

The transport equations for the two scalar variables are

$$\rho u_i \frac{\partial \xi}{\partial x_i} = \frac{\partial}{\partial x_i} (\Gamma_\xi \frac{\partial \xi}{\partial x_i}) \quad (25)$$

$$\rho u_i \frac{\partial Y_{H_2}^*}{\partial x_i} = \frac{\partial}{\partial x_i} (\Gamma_\eta \frac{\partial Y_{H_2}^*}{\partial x_i}) + \dot{w}_{H_2}^* \quad (26)$$

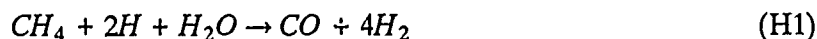
showing the passive and reactive natures of  $\xi$  and  $\eta$ , respectively. Equations (25) and (26) are analogous to the Navier-Stokes in that they must be subjected to time-averaging and closure (or other modeling) before becoming useful in the context of turbulent flames.

#### Hydrocarbon Kinetics:

Chemical kinetic models are available for the simple hydrocarbons such as lower alkanes, but involve  $\sim 50$  species and  $\sim 250$  elementary reactions if nitrogen chemistry is included. Such schemes cannot be implemented in turbulent flow models. There is an incentive to simplify schemes while preserving essential features.

By adding and subtracting elementary reactions in the full scheme so as to cancel out selected fast reactions, systematically reduced schemes have been obtained for simple hydrocarbons [e.g., Paczko et al. (1986)]. Typically three or four progress variables are required, but account for  $\sim 50$  kinetic source terms which are sums of the surviving elementary rates. Assessment has consisted primarily of running the reduced schemes, in calculations of laminar premixed and counterflow diffusion flames, against the full schemes. In general, results such as the flame speed of premixed flames and the structure of diffusion flames compare well.

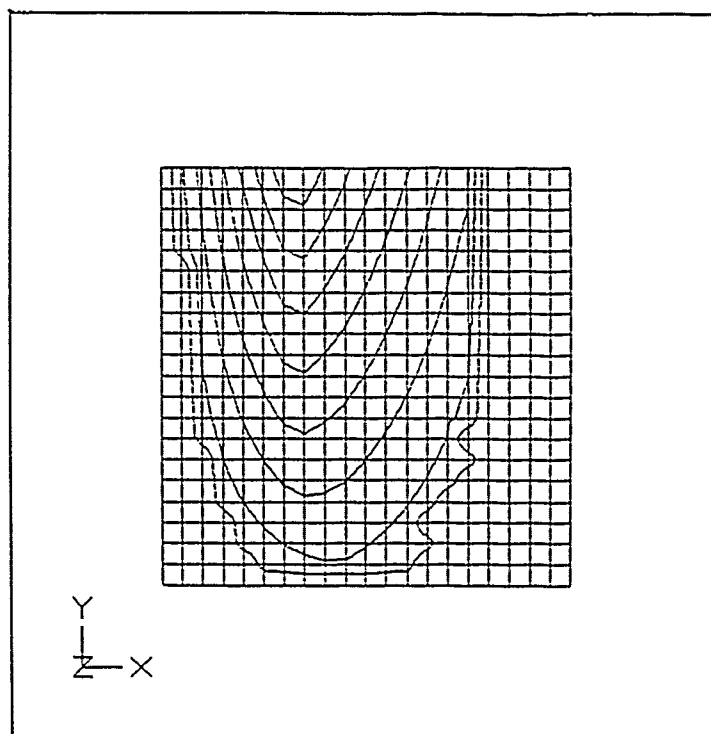
An example of such a scheme is



Such models are computationally tractable in multidimensional turbulent flow calculations and will be used in the future for methane flames.

LEVEL	VALUE
A	299.00
B	510.22
C	721.44
D	932.67
E	1143.9
F	1355.1
G	1566.3
H	1777.6
I	1988.8
J	2200.0

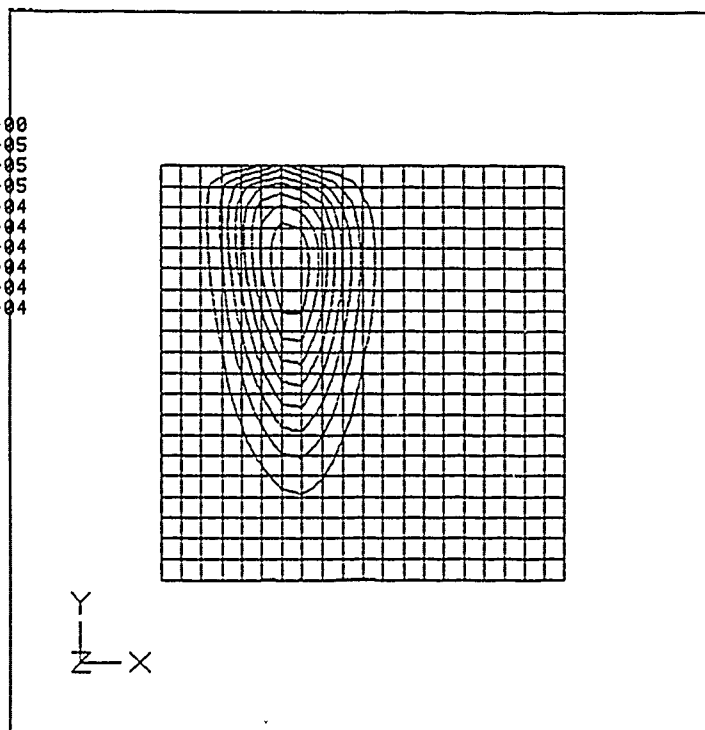
>> █



(a)

LEVEL	VALUE
A	0.00000E+00
B	2.77778E-05
C	5.55556E-05
D	8.33333E-05
E	1.11111E-04
F	1.38889E-04
G	1.66667E-04
H	1.94444E-04
I	2.22222E-04
J	2.50000E-04

>> oh █



(b)

Figure 30. Contours in thermochemical phase space.  
 (a) Temperature.  
 (b) Hydroxyl radical OH.

## 2.4.4 Turbulence-Chemistry Interaction Models

Just as closure is needed for velocity-velocity and velocity-scalar correlations, it is an important issue in the mean chemical source terms. The most widely used approach is to derive, in some manner to be discussed, the probability density function for the flow in terms of the required scalar(s). If those scalars are  $\psi_i$  ( $i = 1, N$ ), then the average of any quantity  $\phi_s$  is obtained by integration

$$\bar{\phi}_s = \int \cdots \int \phi_s(\psi_i) \bar{P}(\bar{x}; \psi_i) d\psi_1 \cdots d\psi_N \quad (27)$$

where  $\bar{P}(\bar{x}; \psi_i)$  is the pdf at the point  $\bar{x}$ , and  $\phi_s(\psi_i)$  is the instantaneous value of  $\phi_s$  corresponding to the particular values  $(\psi_i)$ . Higher moments can also be obtained, e.g.,

$$\phi_s^{-2} = \int \cdots \int (\phi_s - \bar{\phi}_s)^2 \bar{P}(\bar{x}; \psi_i) d\psi_1 \cdots d\psi_2 \quad (28)$$

The mean reaction rate, mean density, or any other scalar statistic are so obtained. Also because

$$\bar{P}(\bar{x}; \psi_i) = \frac{\rho(\psi_i)}{\bar{\rho}(x)} \bar{P}(x; \psi_i) \quad (29)$$

either density-weighted or conventional statistics can be obtained for all the  $\phi_s$ .

The closure problem is approached in ensemble-averaged Navier-Stokes models by solving for the lowest moments of the pdf over scalars. To be specific, closure for the (two-scalar) partial-equilibrium model is reviewed next.

Assumed Shape PDF Model:

The mean and variance of  $\xi$  and  $\eta$  which are obtained at each point constitute the local (lowest) moments of the joint pdf of fluctuations in  $\xi$  and  $\eta$ ,  $\bar{P}(\xi, \eta)$ . Moment methods assume that the functional relationship between the joint pdf and these moments is known, so that these moments lead to the local pdf. The functional relationship is assumed to be

$$\bar{P}(\xi, \eta) = \bar{f}(\xi) \bar{g}(\eta) \quad (30)$$

which implies that fluctuations in  $\xi$  and  $\eta$  are uncorrelated. The pdf over  $\xi$  is taken as a  $\beta$ -function:

$$\beta(\xi) = \frac{\xi^{a-1} (1-\xi)^{b-1}}{\int_0^1 \xi^{a-1} (1-\xi)^{b-1} d\xi} \quad (31)$$

In the other dimension ( $\eta$ ), Janicka and Kollman (1982) proposed the form of the pdf as three Dirac delta functions:

$$\bar{g}(\eta) = c_1 \delta(\eta) + c_2 \delta(\eta - \bar{\eta}) + c_3 \delta(1 - \eta) \quad (32)$$

The distribution consists of delta functions at  $\eta=0$ ,  $\eta=\bar{\eta}$  and  $\eta=1$ . The constants  $a$ ,  $b$ , and  $c_1 - c_3$  are obtained in terms of the moments from normalization conditions and expressions for the moments such as

$$\bar{\xi} = \int_0^1 \xi \bar{f}(\xi) d\xi \quad (33)$$

where the functional form of the pdf is used. Thus, the local pdf is obtained parametrically through

the coefficients which depend on the local moments. These moment equations are obtained by averaging the equations for mixture fraction and reaction progress variable [Jones and Whitelaw (1984), Correa and Shyy (1987)]. All mean quantities in the transport equations, e.g.,  $\dot{w}_{H_2}$ , are then obtained by convolution of the instantaneous quantity, e.g.,  $\dot{w}_{H_2}(\xi, \eta)$ , with the joint pdf.

A survey of the constants  $c_1 - c_3$  during calculation of jet flames has shown that  $c_2$  is very close to unity. This agrees with Janicka and Kollman's (1982) finding that  $g(\eta)$  could be specified as three delta functions, one delta function at  $\eta = \bar{\eta}$  or a  $\beta$ -function without much impact on the predicted mean OH concentration. The adequacy of the shape of the pdf in  $\eta$  was tested by the agreement on both the mean and rms components of the OH concentration [Correa et al. (1984)], and in comparisons with Monte Carlo methods for direct calculation of the joint velocity-scalars pdf evolution equation [Pope and Correa (1987)].

#### PDF Transport Model:

A turbulent flow is described by the following dependent variables: velocity  $\vec{U}$  and additional scalars such as mixture fraction  $\xi$  and the reaction progress variable  $\eta$ , introduced above. Here a one-point statistical description in terms of the joint pdf of  $\vec{U}$  and the scalars ( $\xi$  and  $\eta$ ) is sought. If the flow is statistically stationary, all one-point statistics depend only on the spatial coordinates.

The joint velocity-scalars' pdf evolution model relaxes many of the assumptions made in the above standard closure. The joint pdf  $P(\vec{V}, \xi, \eta; x, r)$  is the probability of the simultaneous events  $\vec{U} = \vec{V}$ ,  $\xi = \xi$  and  $\eta = \eta$  at that location in space and time. All one-point statistics are recovered from this pdf because the composition is a known function of  $\xi$  and  $\eta$ . For example, the mean of a quantity  $\phi$  is

$$\langle \phi(x, r) \rangle \equiv \int \int \phi(\xi, \eta) P(\vec{V}, \xi, \eta; x, r) d\vec{V} d\xi d\eta. \quad (34)$$

Any correlations such as higher moments or fluxes can be computed similarly. The problem is therefore to determine the joint pdf  $P$  at each point in the flowfield.

Pope (1985) has developed a transport equation for the evolution of the joint pdf. This exact equation for  $P$  is derived directly from the Navier-Stokes equations and the species conservation equations. Even for variable-density flows with complex chemistry, convection (including all fluxes), chemical reaction, and the mean pressure gradient do not have to be modeled. Molecular transport and the fluctuating pressure gradient require modeling for closure. The modeling used by Pope and Correa (1987) follows that for a self-similar plane jet. A conditional model was used to discriminate between the turbulent and the nonturbulent fluid in jet flows. The mixture fraction  $\xi$  also is the concentration of nozzle fluid; hence  $\xi = 0$  indicates nonturbulent ambient gas and  $\xi > 0$  indicates turbulent gas. Details of the stochastic mixing models, which account for molecular transport, and the stochastic reorientation models, which account for pressure fluctuations, were given first by Pope (1985).

The pdf transport occurs in a multidimensional space composed of the independent variables in the problem, viz., two spatial variables,  $(x, r)$ , three velocity variables  $\vec{V}$ , and two scalar variables  $(\xi, \eta)$ . Calculations of transport equations are already computationally intensive in three dimensions and so a Monte Carlo numerical technique is used [Pope (1985)]. Simplifications analogous to the boundary-layer approximation were made.

In the Monte Carlo method, the joint pdf is represented by a large number  $N$  of notional particles ( $N \approx 35,000$ ). At location  $x$ , the  $n$ -th particle has the radial position  $r^{(n)}(x)$ , velocity  $U^{(n)}(x)$  and composition  $\xi^{(n)}, \eta^{(n)}(x)$ . Initial conditions are specified at the jet exit ( $x = 0$ ).

This model has been applied to the  $Re=8500$ , 40%  $CO$ , 30%  $H_2$ , 30%  $N_2$  turbulent jet diffusion flame, with partial-equilibrium chemistry. Although the results agreed broadly with those of the assumed-shape pdf/ $k-\epsilon$  model, some differences were evident [Pope and Correa (1987)]. For example, a strong correlation was found to exist between  $\xi$  and  $\eta$ , but it did not greatly affect the predicted mean quantities. The prediction of rms quantities was improved.

#### 2.4.5 Flow Algorithm

This account of the flow algorithm is brief, since it has been well published already. Further details and applications may be found in the review by Correa and Shyy (1987).

Axisymmetric bluff-body stabilized flames are characterized by recirculating rather than jet-like flow, with attendant numerical complications. The governing equations are written in strong conservation law form in general curvilinear coordinates, as derived by Vinokur (1974). The conservation equations can be written in Cartesian coordinates for a dependent variable  $\phi$  in the following form, retaining 3D formulation for the present:

$$\frac{\partial}{\partial x} (\rho u \phi) + \frac{\partial}{\partial y} (\rho v \phi) + \frac{\partial}{\partial z} (\rho w \phi) = \frac{\partial}{\partial x} \left( \Gamma \frac{\partial \phi}{\partial x} \right) + \frac{\partial}{\partial y} \left( \Gamma \frac{\partial \phi}{\partial y} \right) + \frac{\partial}{\partial z} \left( \Gamma \frac{\partial \phi}{\partial z} \right) + R(x, y, z) \quad (35a)$$

where  $\Gamma$  is the effective diffusion coefficient and  $R$  is the source term. When new independent variables  $\xi, \eta$ , and  $\gamma$  are introduced, Eq. (35a) changes according to the general transformation  $\xi = \xi(x, y, z)$ ,  $\eta = \eta(x, y, z)$ ,  $\gamma = \gamma(x, y, z)$ . The result of this coordinate transformation is to transform the arbitrarily shaped physical domain into a rectangular parallelepiped.

Equation (35a) can be rewritten in  $(\xi, \eta, \gamma)$  coordinates as follows:

$$\begin{aligned} & \frac{\partial}{\partial \xi} (\rho U \phi) + \frac{\partial}{\partial \eta} (\rho V \phi) + \frac{\partial}{\partial \gamma} (\rho W \phi) \\ &= \frac{\partial}{\partial \xi} \left[ \frac{\Gamma}{J} (q_{11} \phi_\xi + q_{12} \phi_\eta + q_{13} \phi_\gamma) \right] + \frac{\partial}{\partial \eta} \left[ \frac{\Gamma}{J} (q_{21} \phi_\xi + q_{22} \phi_\eta + q_{23} \phi_\gamma) \right] \\ & \quad + \frac{\partial}{\partial \gamma} \left[ \frac{\Gamma}{J} (q_{31} \phi_\xi + q_{32} \phi_\eta + q_{33} \phi_\gamma) \right] + S(\xi, \eta, \gamma) \cdot J \end{aligned} \quad (35b)$$

where the contravariant velocity components and the combinations of metric terms,  $q_{ij}$ , are

$$U = u(y_\eta z_\gamma - y_\gamma z_\eta) + v(x_\gamma z_\eta - x_\eta z_\gamma) + w(x_\eta y_\gamma - x_\gamma y_\eta) \quad (36)$$

$$V = u(y_\gamma z_\xi - y_\xi z_\gamma) + v(x_\xi z_\gamma - x_\gamma z_\xi) + w(x_\gamma y_\xi - x_\xi y_\gamma) \quad (37)$$

$$W = u(y_\xi z_\eta - y_\eta z_\xi) + v(x_\eta z_\xi - x_\xi z_\eta) + w(x_\xi y_\eta - x_\eta y_\xi) \quad (38)$$

$$q_{11} = (y_\eta z_\gamma - y_\gamma z_\eta)^2 + (x_\gamma z_\eta - x_\eta z_\gamma)^2 + (x_\eta y_\gamma - x_\gamma y_\eta)^2 \quad (39)$$

$$q_{22} = (y_{\tau} z_{\xi} - y_{\xi} z_{\tau})^2 + (x_{\xi} z_{\tau} - x_{\tau} z_{\xi})^2 + (x_{\tau} y_{\xi} - x_{\xi} y_{\tau})^2 \quad (40)$$

$$q_{33} = (y_{\xi} z_{\eta} - y_{\eta} z_{\xi})^2 + (x_{\eta} z_{\xi} - x_{\xi} z_{\eta})^2 + (x_{\xi} y_{\eta} - x_{\eta} y_{\xi})^2 \quad (41)$$

$$q_{12} = (y_{\tau} z_{\xi} - y_{\xi} z_{\tau}) (y_{\tau} z_{\eta} - y_{\eta} z_{\tau}) + (x_{\xi} z_{\tau} - x_{\tau} z_{\xi}) (x_{\tau} z_{\eta} - x_{\eta} z_{\tau}) + (x_{\tau} y_{\xi} - x_{\xi} y_{\tau}) (x_{\eta} y_{\tau} - x_{\tau} y_{\eta}) \quad (42)$$

$$q_{13} = (y_{\xi} z_{\eta} - y_{\eta} z_{\xi}) (y_{\tau} z_{\xi} - y_{\xi} z_{\tau}) + (x_{\tau} z_{\eta} - x_{\eta} z_{\tau}) (x_{\eta} z_{\xi} - x_{\xi} z_{\eta}) + (x_{\xi} y_{\eta} - x_{\eta} y_{\xi}) (x_{\eta} y_{\tau} - x_{\tau} y_{\eta}) \quad (43)$$

$$q_{23} = (y_{\xi} z_{\eta} - y_{\eta} z_{\xi}) (y_{\tau} z_{\xi} - y_{\xi} z_{\tau}) + (x_{\eta} z_{\xi} - x_{\xi} z_{\eta}) (x_{\xi} z_{\tau} - x_{\tau} z_{\xi}) + (x_{\xi} y_{\eta} - x_{\eta} y_{\xi}) (x_{\tau} y_{\xi} - x_{\xi} y_{\tau}) \quad (44)$$

with  $q_{21} = q_{12}$ ,  $q_{31} = q_{13}$ ,  $q_{32} = q_{23}$ , and finally

$$J = x_{\xi} y_{\eta} z_{\tau} + x_{\tau} y_{\xi} z_{\eta} + x_{\eta} y_{\tau} z_{\xi} - x_{\xi} y_{\tau} z_{\eta} - x_{\tau} y_{\eta} z_{\xi} - x_{\eta} y_{\xi} z_{\tau} \quad (45)$$

$S(\xi, \eta, \gamma)$  is the source term of the governing equation in  $(\xi, \eta, \gamma)$  coordinates. The momentum equations are written in terms of the Cartesian velocity components, while in the continuity equation the contravariant velocity components are used. This formulation has the advantage that the equations retain simple forms without a large number of additional terms.

The main features of the computational method are

1. **Meshing:** The domain of interest in the physical domain is covered with a body-fitted computational mesh and is numerically transformed to a square in 2D (cube in 3D). The transformed equations (35b) are solved in the transformed domain. Of course, most laboratory experiments, including the present one, can be described in terms of a rectilinear (Cartesian or cylindrical-polar) mesh, perhaps nonuniform in cell size.
2. **Staggered Grid:** Variables are not defined at the same mesh points. The "staggered" grid concept [Harlow and Welch (1965)] locates scalar variables such as pressure, density, turbulence kinetic energy, and so on, at common mesh points. Offset half a mesh-spacing to the left and below are the (axial)  $u$  and (lateral)  $v$  velocity points, respectively (in three dimensions,  $w$  is similarly staggered). This configuration stabilizes the pressure-velocity coupling.
3. **Control Volume Formulation:** The partial differential equations are integrated over control volumes centered on each grid point. The advantages of the staggered grid are then realized, since the velocity and scalar values are located exactly where they are needed – at the surfaces of the control volumes. This formulation also ensures global conservation.
4. **Discretization Schemes:** Discretization of the convection terms can be one of the principal sources of error in numerical solutions of high Reynolds number flow. Second-order central differences for the convection term are consistent with discretization of diffusion terms, but make the coefficient matrix lose diagonal dominance when the cell Reynolds/Peclet number exceeds two. Solution profiles then exhibit characteristic "wiggles" or oscillations which can become unbounded. A standard method to stabilize high Reynolds/Peclet number calculations is to evaluate the fluxes using the "hybrid" scheme, consisting of first-order upwind differencing at cells where the Reynolds/Peclet number exceeds two and second-order central differencing everywhere else [Spalding (1972)]. The use of the hybrid scheme therefore causes the loss of

one order of accuracy in regions of high (greater than two) cell Reynolds or Peclet numbers, leading to overly diffusive solutions [Leschziner and Rodi (1980); Raithby (1976); Shyy and Correa (1985)]. Numerical stability is, however, guaranteed.

The first-order upwinding, second-order upwinding, and QUICK [Leonard (1981)] schemes are coded into our algorithm, and any one of them can be used in any given transport equation by selecting appropriate input options.

Evaluations of various finite difference operators for the convection term in the context of two- and three-dimensional recirculating flow calculations can be found in, for example, Tuann and Olson (1978), Leschziner and Rodi (1980), Shyy and Correa (1985), and Mei and Plotkin (1986). Discretization errors have also been quantitatively compared to other terms in each balance equation [Correa (1984), McGuirk et al. (1981)]. A second-order centrally-differenced a posteriori calculation of convection terms is subtracted from the original operator. The out-of-balance term is the "numerical diffusion" and is compared with each of the other terms (convection, diffusion, pressure gradient, source) at each node. Correa (1984) has already provided such evaluations for the bluff-body stabilized diffusion flame of Roquemore et al. (1982) and has indicated where to concentrate the grid in such a calculation.

In the calculations reported below, contours of the transverse cell Reynolds number are presented to help quantify the errors due to discretization.

5. SIMPLE: In the set of fluid flow equations, pressure is the only variable that does not have a governing equation. Furthermore, at low Mach numbers the pressure is essentially constant and so the continuity equation cannot be solved directly. The so-called "Semi-Implicit Method for Pressure-Linked Equations" (SIMPLE) algorithm [Patankar (1980)] is intended to overcome this problem. The essential feature is the replacement of the continuity equation (which does not contain the pressure) with a pressure correction equation, and subsequent sequential manipulations of the velocity field.

The algorithm proceeds sequentially through the momentum, pressure-correction, and other scalar equations with a maximum allowance being prescribed for updating each dependent variable. This procedure is defined as the outer iteration cycle. Within each equation, and to within a prescribed tolerance, the discretized system of linearized equations is also solved iteratively. This procedure is called the inner iteration cycle. The degree of convergence of the solution of the individual equations in the inner cycle can be very influential on the overall rate of convergence of the outer cycle.

6. TDMA: The algebraic equations that are the result of discretization are cast into a tridiagonal form and solved by line relaxation using the tridiagonal matrix algorithm (TDMA).

## 2.5 Comparison of Model Predictions with Data

### 2.5.1 Grid

The nonuniform but rectilinear 75 (axial)  $\times$  60 (radial) grid used for the axisymmetric 2D calculation is shown in Figure 31. In each of the coordinate directions, the mesh spacing grows according to a geometric progression with a modest expansion ratio (2% in x-direction, 3% in y-direction). The domain measures 55 jet diameters in axial extent, well beyond the high shear region of interest. The transverse grid is chosen to coincide with the fixed geometric points defined by the fuel tube radius, the bluff-body radius, and the tunnel radius. Since the tunnel is actually of square cross section, the outer radius was defined to give the same cross-sectional area as the square. The tunnel wall has no direct effect on the flame since the flame is confined to the vicinity of the centerline; there is a weak

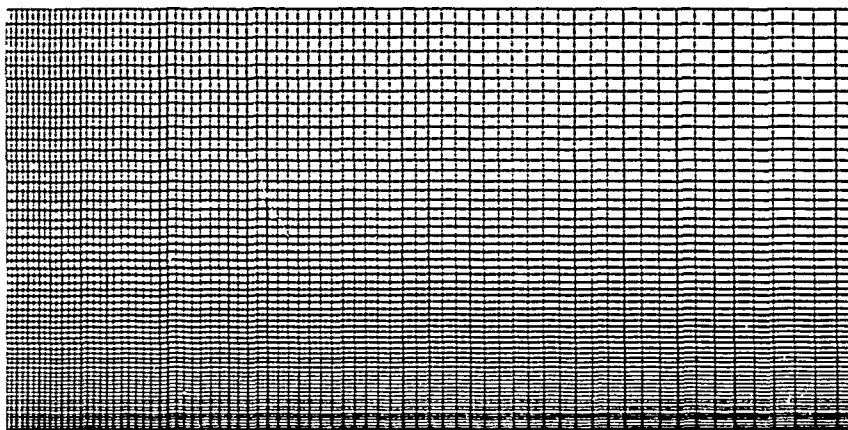


Figure 31. Nonuniform rectilinear 75 (axial)  $\times$  60 (radial) grid.



effect through the axial pressure gradient caused by the heat release, but this effect is accounted for by preserving cross-sectional area of the duct.

The grid expands in the radial and the downstream axial directions, but is dense enough in the critical shear regions as shown in subsection 2.5.3.

### 2.5.2 Boundary Conditions

The burner conditions are: pressure = 1 atm, inlet temperature = 300 K, bulk-averaged jet velocity = 80 m/s, and bulk-averaged annulus velocity = 6.5 m/s. Boundary conditions in the calculation are taken as plug flow in the jet and annulus, with inlet turbulence kinetic energy ( $k$ ) taken as 0.5% of the mean local velocity squared, and inlet dissipation rate ( $\epsilon$ ) obtained from the assumed length scale of turbulence (3% of the jet or annulus dimension). It is well known that such calculations can be sensitive to inlet boundary conditions on  $k$  and  $\epsilon$ , but variations in a reasonable range made little difference. For example, increasing the jet turbulence length scale by a factor of 5 changed the mean mixture fraction field values by less than 1%. The reason is that turbulence generation in this flow rapidly overwhelms the inlet levels.

### 2.5.3 Reduction of Discretization Error

As discussed in the section on "Discretization" above, numerical diffusion errors are expected in regions where the cell Reynolds numbers (Peclet numbers in scalar transport equations) are above two. Figure 32 shows the transverse cell Reynolds numbers in the flame calculation. The local transverse cell Reynolds number at each point  $(x,y)$  in the calculation domain is defined as

$$Re_{\Delta y}(x,y) = \frac{\rho(x,y) v(x,y) \Delta y}{\mu_t(x,y)} \quad (46)$$

The transverse direction is significant since it is the direction in which the important turbulent exchange (of mass, momentum, energy) occurs. The density, velocity, and turbulent viscosity fields are taken from the converged solution. It is clear from Figure 32 that the cell Reynolds numbers are below two everywhere except in the shear layer coming off the bluff body: this is not a cause for concern since there is no fuel or flame there (as shown below). The important shear layers are those along the flammable contours of mixture fraction, and these are adequately gridded.

Eliminating numerical diffusion from the convection operator does not mean that there are no numerical errors. A mesh-size dependent error still exists because of truncation, i.e., neglecting terms of higher-order (than second) in the Taylor series expansion of the convection and diffusion operators [Correa and Shyy (1987)]. It does mean, however, that the errors will monotonically decline in a sequence of nested grids, and also that turbulence models can be assessed without artificial diffusion.

### 2.5.4 Contour Plots

Contour plots of the calculated fields are presented first to give an overall view of the flame structure. Profiles are compared with data in the following two subsections.

Figures 33 and 34 show contours of the Favre-averaged mean mixture fraction and its variance, respectively, which are the lowest moments of the pdf over mixture fraction. For reference, note that the stoichiometric value is  $\xi = 0.33$ . Both sets of contours appear jet-like but with greater mixing at the base ( $0 < x/d < 20$ ). The maximum strain rates (scalar fluctuations) occur in the jet shear layer and are on the order of 30% of the local mean. Contours of the turbulent eddy viscosity ( $\mu_t$ ), obtained from the  $k$ - $\epsilon$  model as described above, show that there is another shear layer associated with the bluff

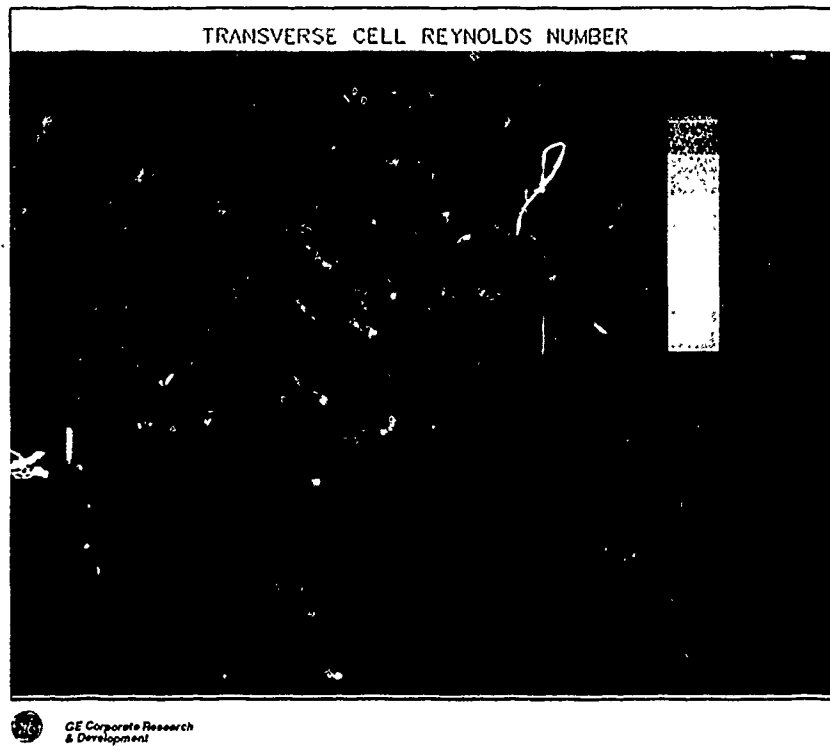


Figure 32. Transverse cell Reynolds numbers in the calculation.

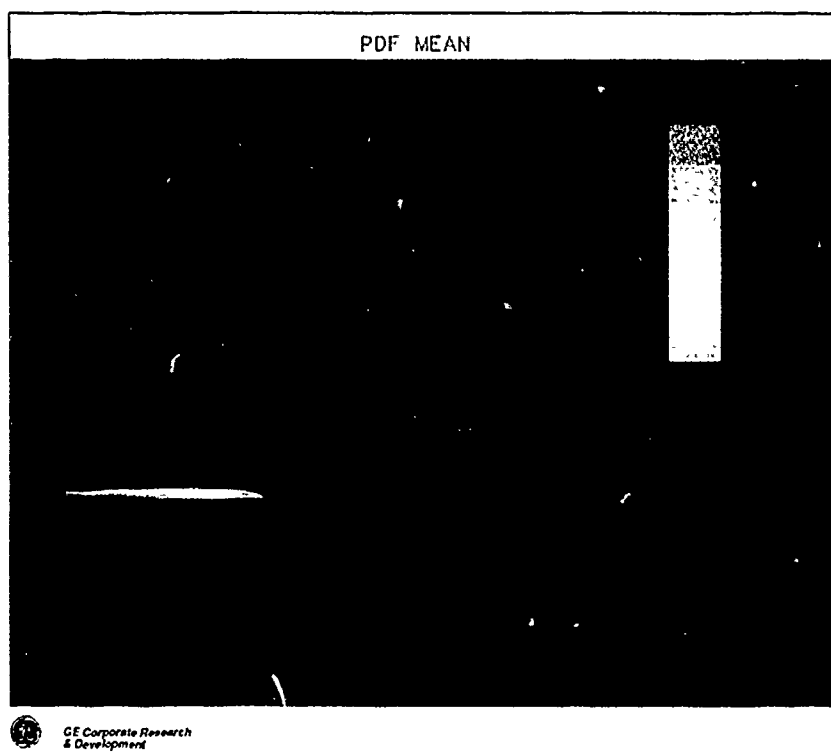


Figure 33. Contours of the Favre-averaged mean mixture fraction.

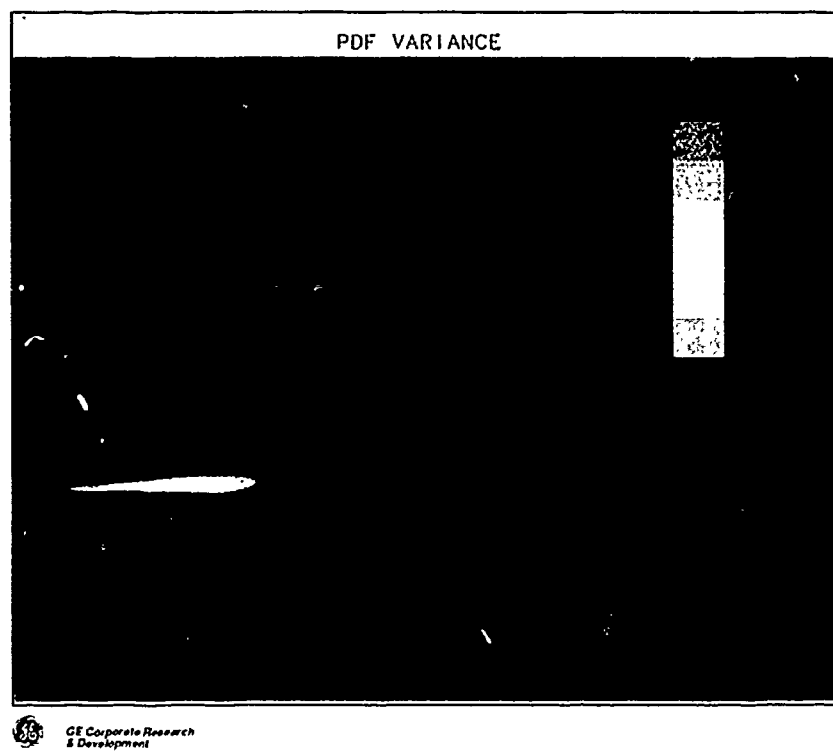


Figure 34. Contours of the Favre-averaged mixture fraction variance.

body. The latter layer affects only the velocity (and so  $k$ ,  $\epsilon$ , and  $\mu_t$ ) since the mixture fraction is not transported that far out radially.

The peak mean (unweighted) temperatures (Figure 35) are about 500 K below the stoichiometric adiabatic equilibrium value of 2170 K. This large decrement is caused by the intense turbulence. The reaction progress variable  $\eta$  (Figure 36) likewise shows a minimum in the shear layer.

Mean species fields are shown in Figures 37. The minor species peak along the stoichiometric contour, as expected.

### 2.5.5 Axial Profiles

Axial profiles along the centerline are presented for the mean density, axial velocity, turbulence kinetic energy, and the mean  $\bar{u}^2$  variance of scalar fluctuations (Figures 38 to 42). Raman data are shown for the scalar fields. The predicted jet decays faster than measured. This error can be attributed primarily to use of the standard  $k$ - $\epsilon$  turbulence model, since numerical diffusion in the transverse direction is largely eliminated as shown above. Deficiencies of the  $k$ - $\epsilon$  model are well documented in the literature and include the assumptions of isotropic turbulent eddy viscosity and gradient diffusion, the need for semi-empirical modification in axisymmetric jet or jet-dominated flow, and the intrinsic failure to account for transport of turbulent stresses. Overdiffusive predictions by the  $k$ - $\epsilon$  submodel seem to be responsible for the predicted jet decaying too rapidly.

Figure 43 shows that the normalized turbulence intensity  $\sqrt{(2k/3)} / U$ , where  $U$  is the local mean axial velocity, asymptotes to  $\sim 0.2$ . The corresponding normalized scalar fluctuation intensity profile (rms/mean scalar) is compared with Raman data in Figure 44. The scalar fluctuations develop too rapidly in the calculation, being about twice the measured value at  $x/d = 15$ , but the asymptotic value of 0.3 agrees with the data. It is interesting to note that an asymptotic value of 0.3 has been calculated for turbulent jet diffusion flames, also in agreement with Raman data on scalar fluctuations [Lapp et al. (1983)].

Note that second-order closure of the turbulence correlations could have been employed to relax some of the  $k$ - $\epsilon$ -scalar variance model assumptions. The plan, however, is to proceed directly to the Monte-Carlo joint pdf transport method, which is closed to all orders and will provide the same level of modeling sophistication in recirculating flow as already demonstrated for jet flames [Pope and Correa (1987)].

### 2.5.6 Radial Profiles

Figure 45 compares various Raman data with the calculations at  $x/d = 10$ , which is in the region of maximum shear. It is again clear that peak temperatures are well below the stoichiometric adiabatic equilibrium value. Species predictions are generally in reasonable agreement with the data, except in the cool fuel-rich core where partial equilibrium in the radical pool breaks down. There the model predicts too much  $H_2O$  at the expense of  $H_2$ . Breakdown of the partial equilibrium thermochemical model has previously been noted in our jet flame calculations, with both assumed shape as well as Monte Carlo pdf methods, and is to be expected since the assumption of partial equilibrium in the radical pool is invalid below  $\sim 1100$  K.

Overprediction of the jet decay rate can be interpreted retrospectively as a shift in virtual origin. Figure 46 compares the calculation at  $x/d = 15.4$  with the data at  $x/d = 20$ . This axial shift results in excellent agreement on the mean mixture fraction and the temperature fields.

Figures 47 and 48 compare the predicted Favre-averaged rms mixture fraction fluctuations, normalized by the local mean, with the Raman data at  $x/d = 10$  and  $x/d = 40$ , respectively. This normaliza-

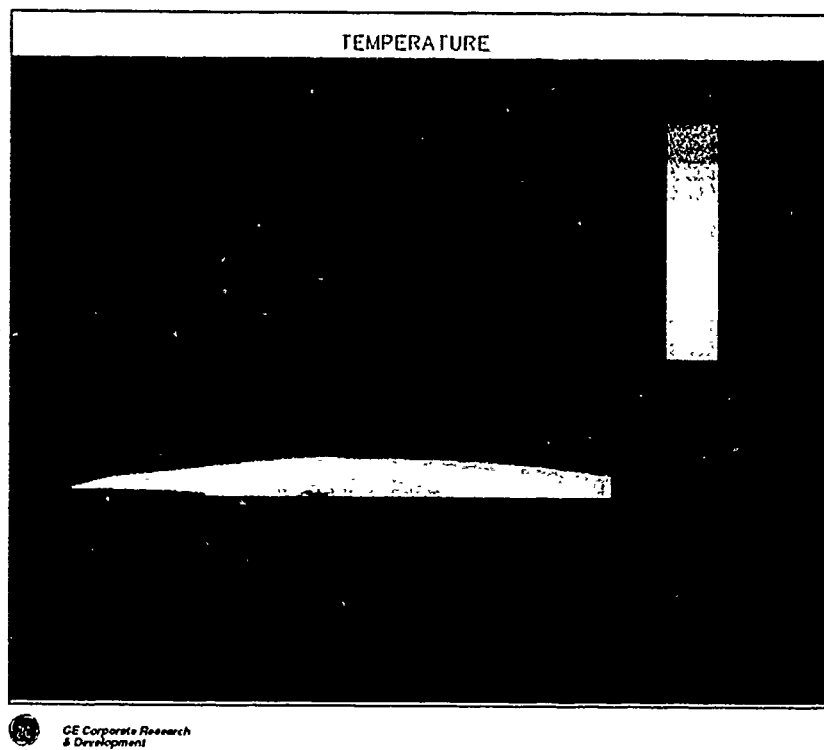


Figure 35. Contours of the mean temperature.

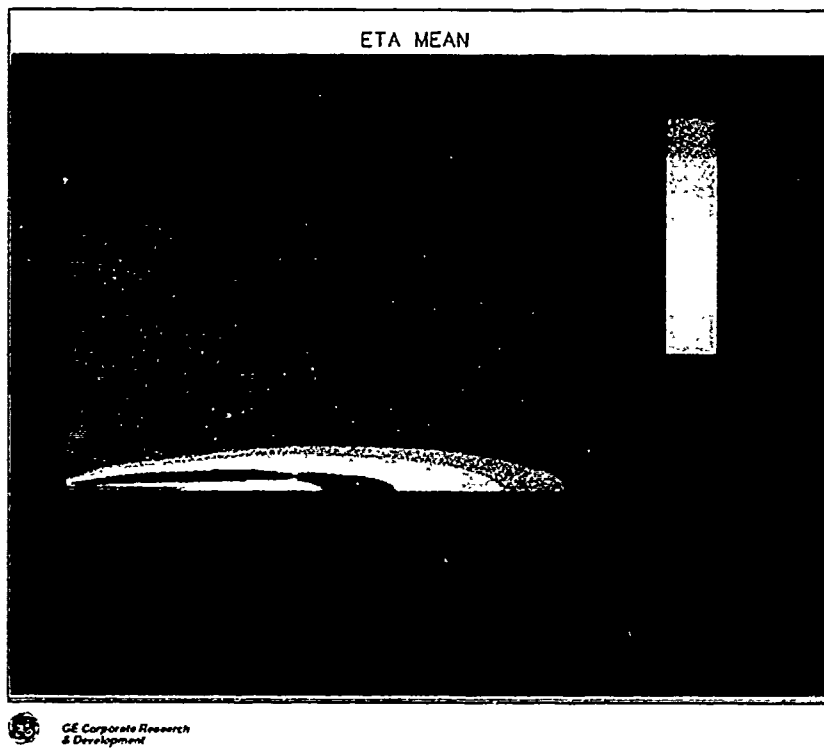


Figure 36. Contours of the mean reaction progress variable.

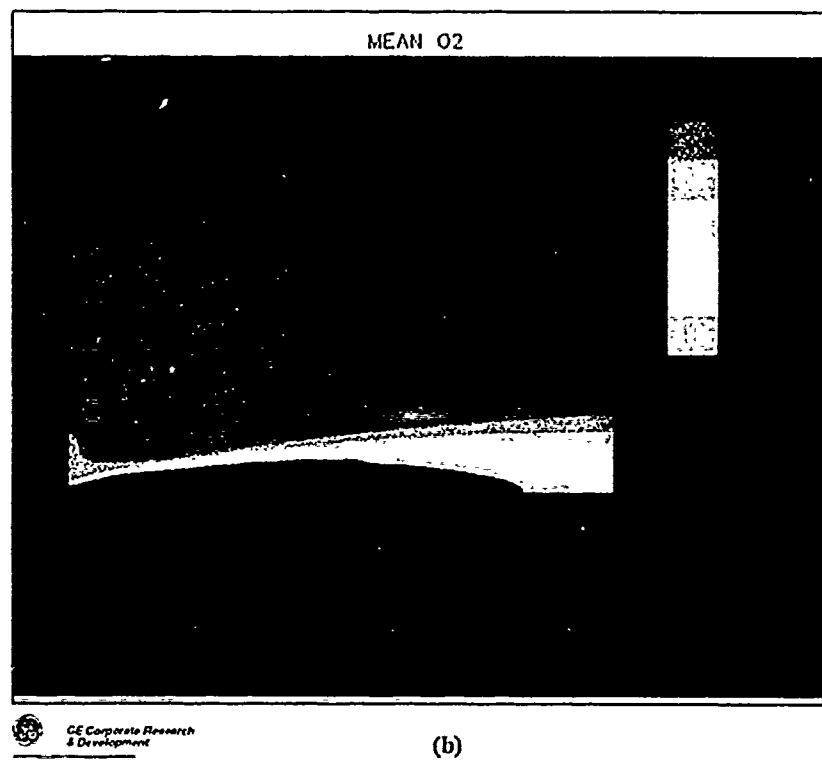
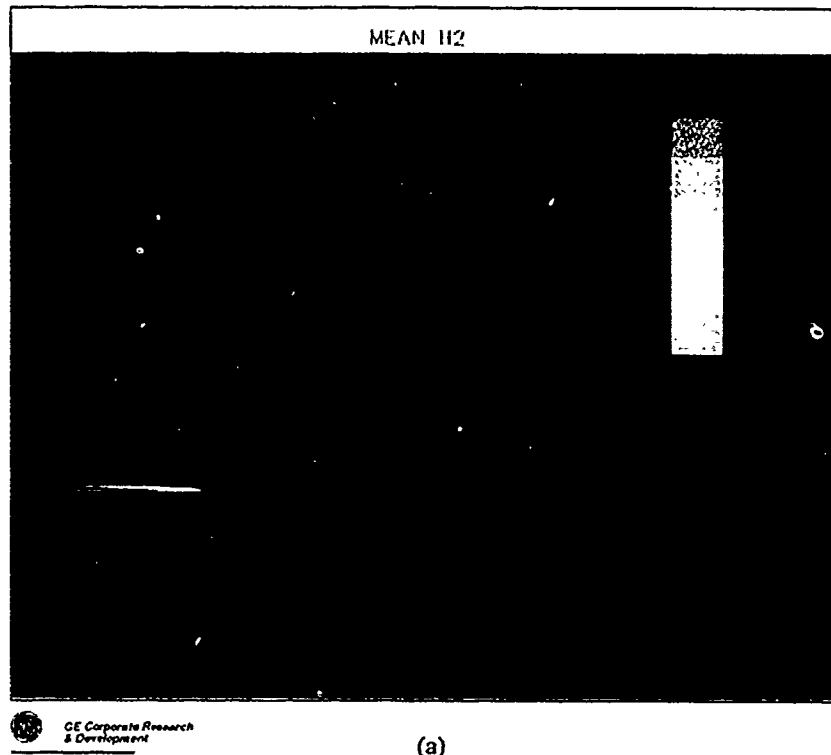


Figure 37. Contours of the Favre-averaged mean species mass fractions.  
 (a)  $H_2$ .  
 (b)  $O_2$ .

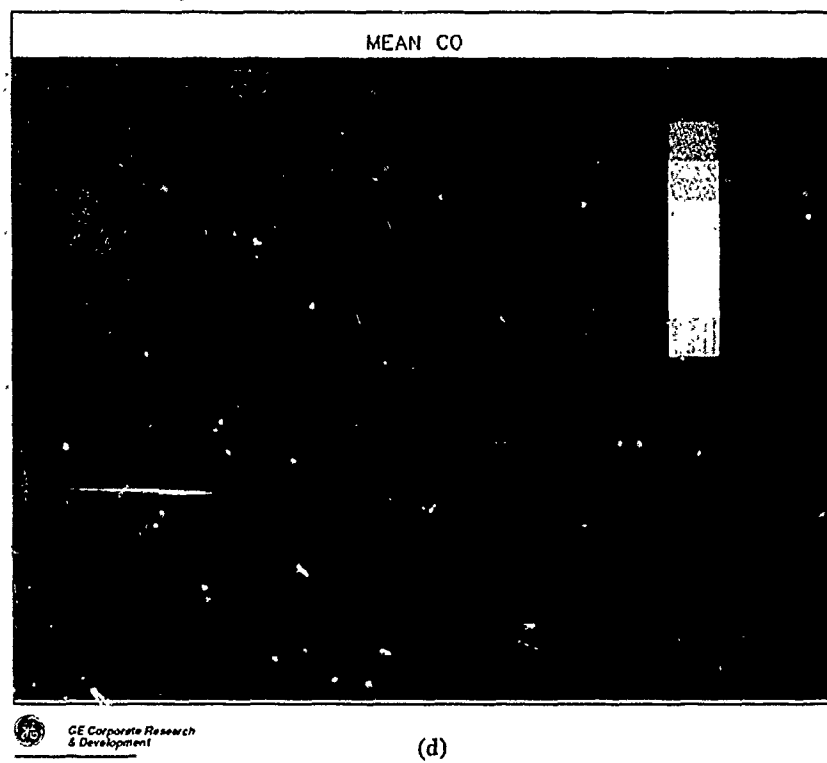
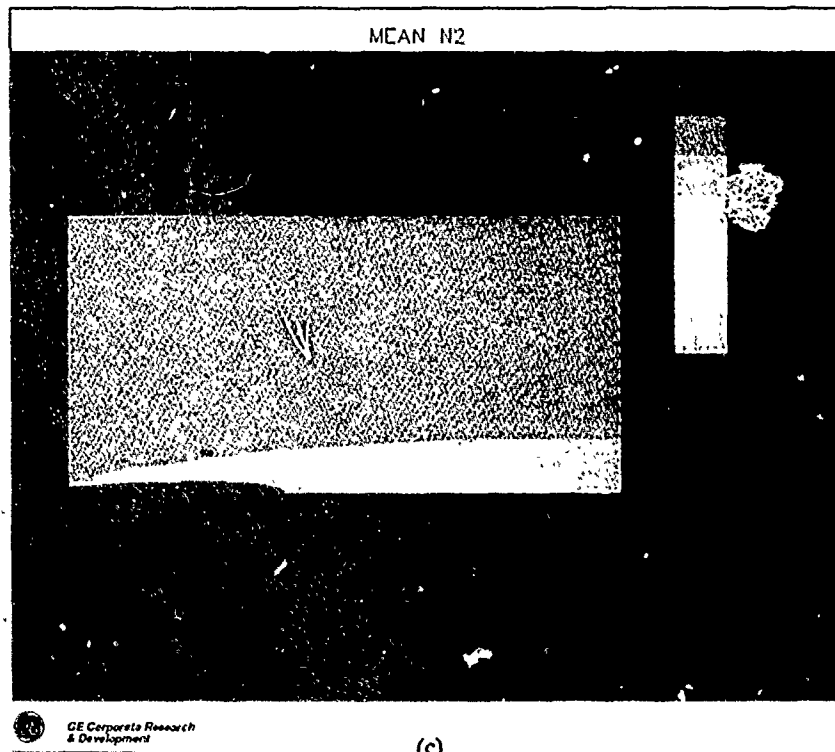
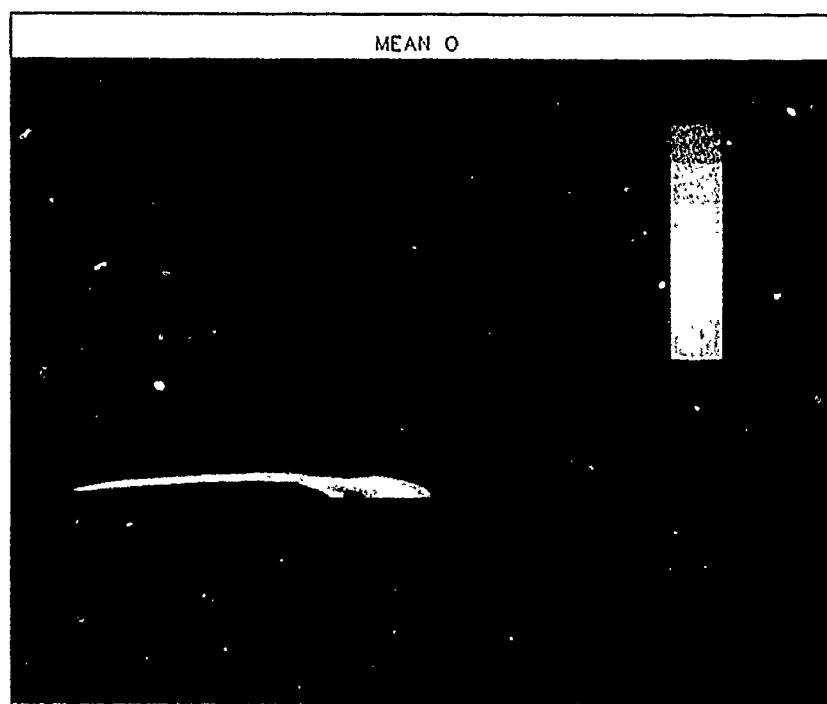
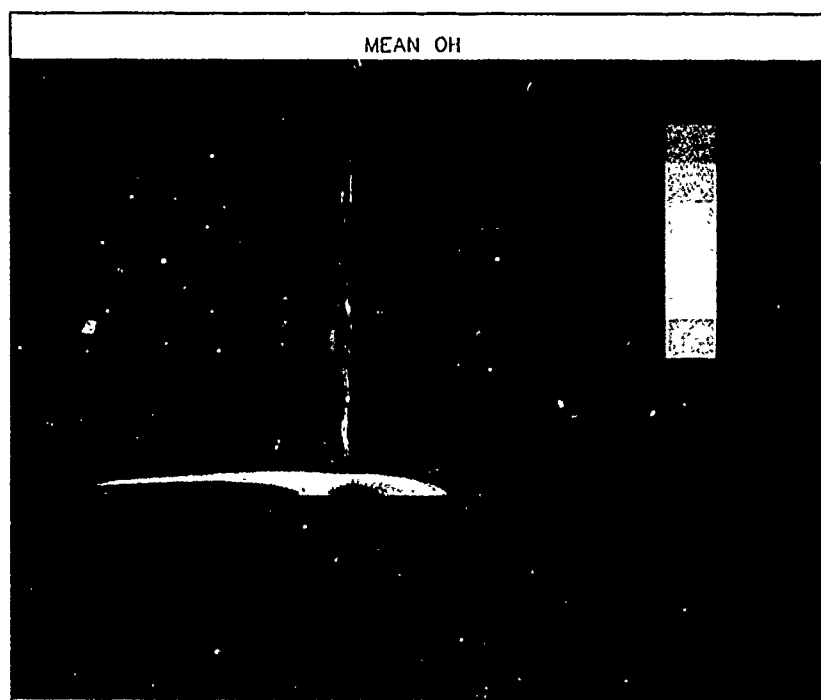


Figure 37. Contours of the Favre-averaged mean species mass fractions.  
 (c) N<sub>2</sub>.  
 (d) CO.



GE Corporate Research  
& Development

(e)



GE Corporate Research  
& Development

(f)

Figure 37. Contours of the Favre-averaged mean species mass fractions.  
(e) O.  
(f) OH.



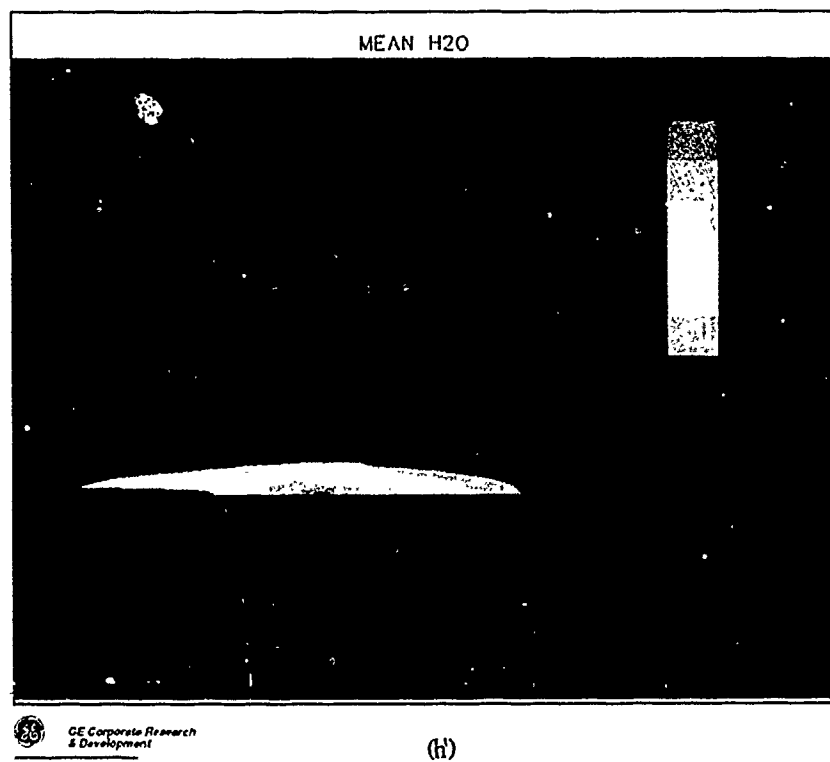
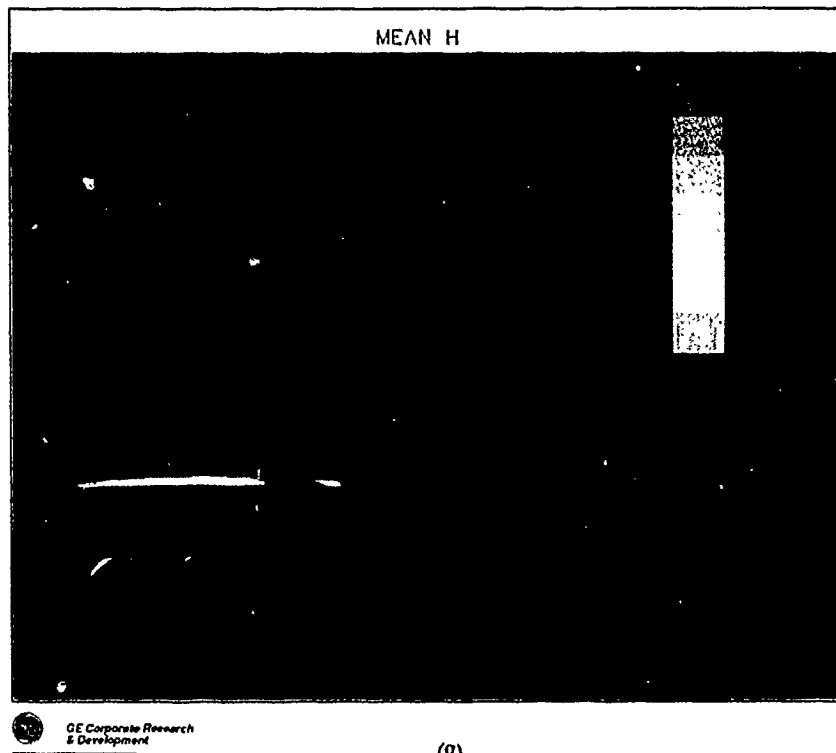


Figure 37. Contours of the Favre-averaged mean species mass fractions.  
(g) H.  
(h) H<sub>2</sub>O.

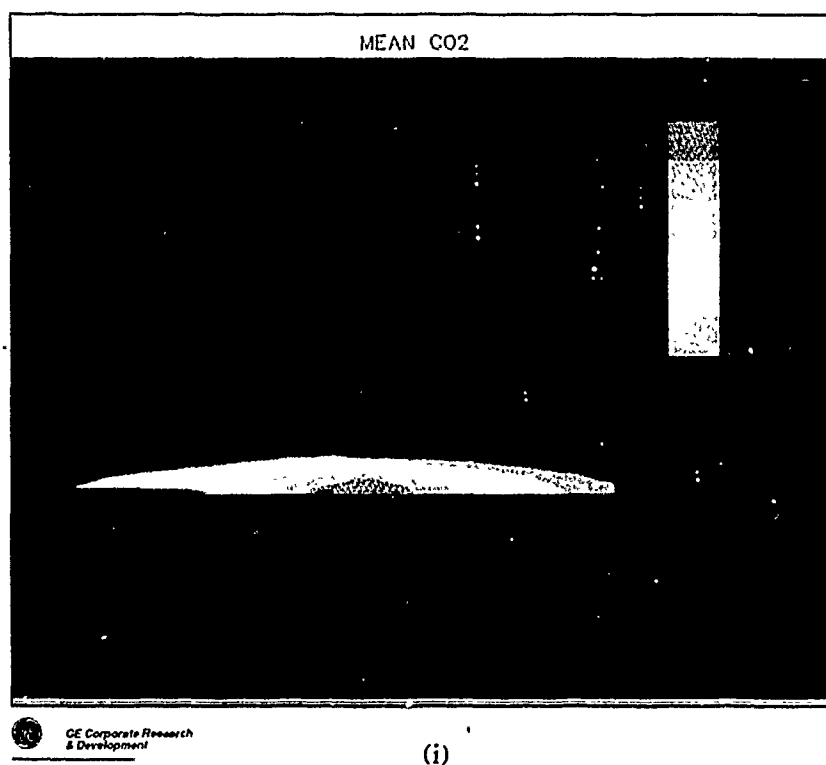


Figure 37. Contours of the Favre-averaged mean species mass fractions.  
(i) CO<sub>2</sub>.

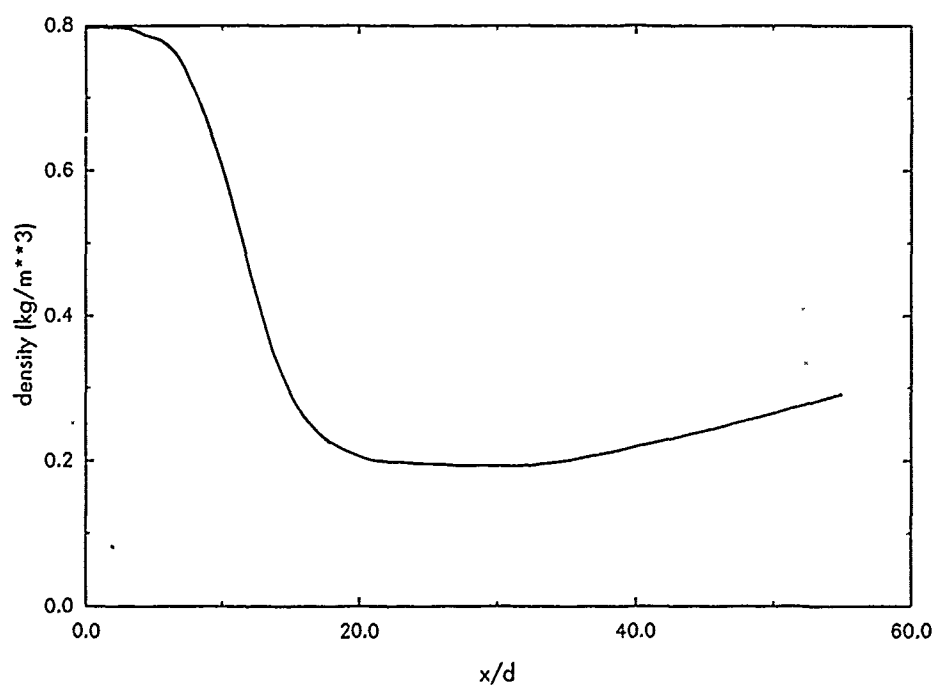
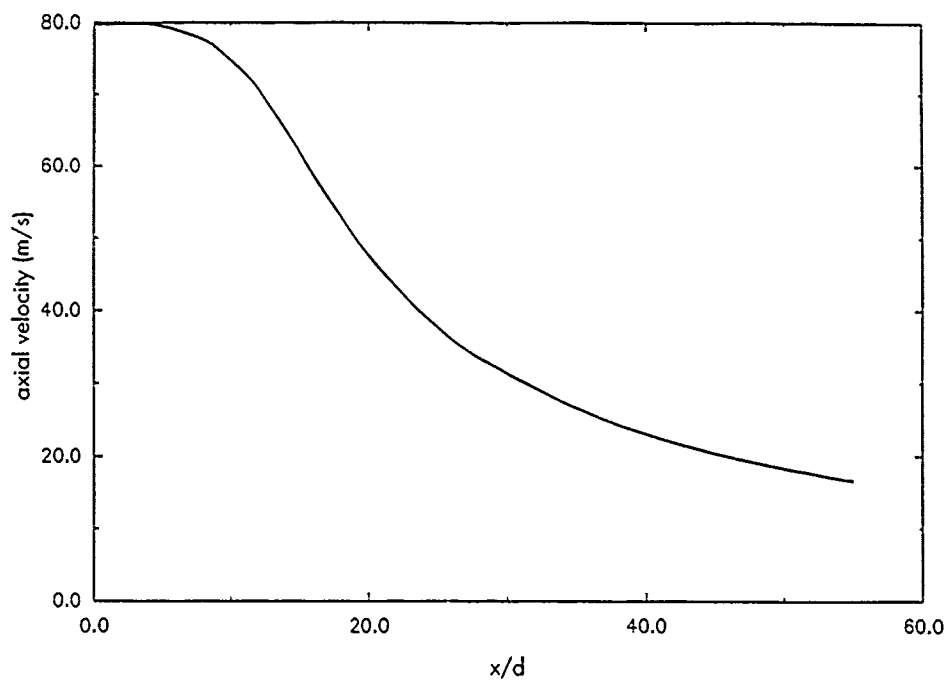
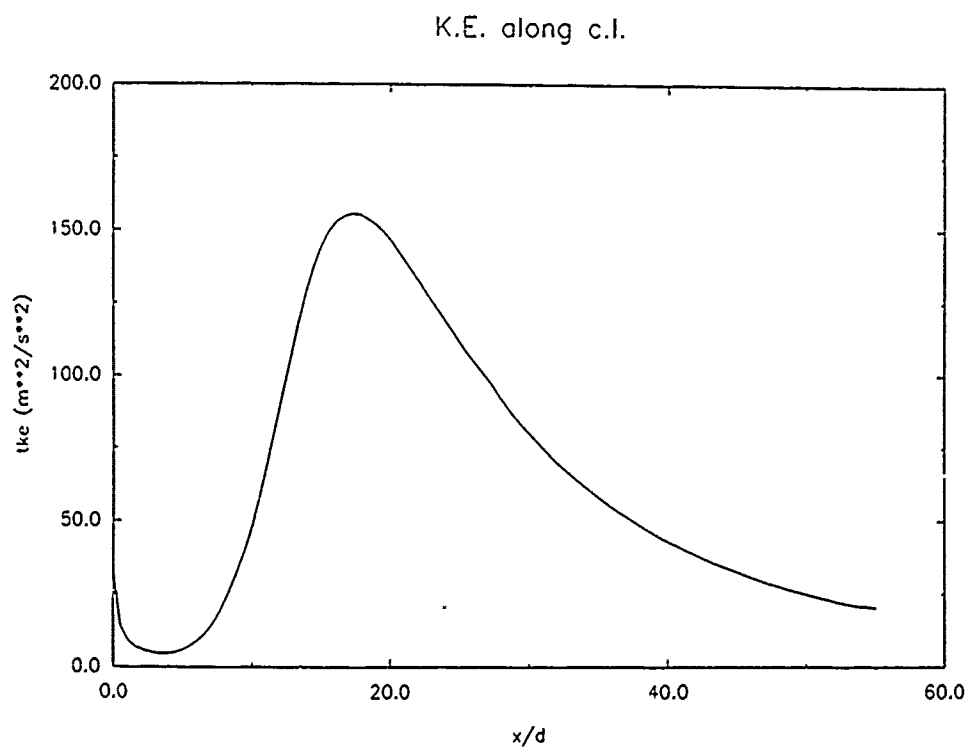


Figure 38. Centerline axial profile of the mean density.



**Figure 39. Centerline axial profile of the mean axial velocity.**



**Figure 40. Centerline axial profile of the mean turbulence kinetic energy.**

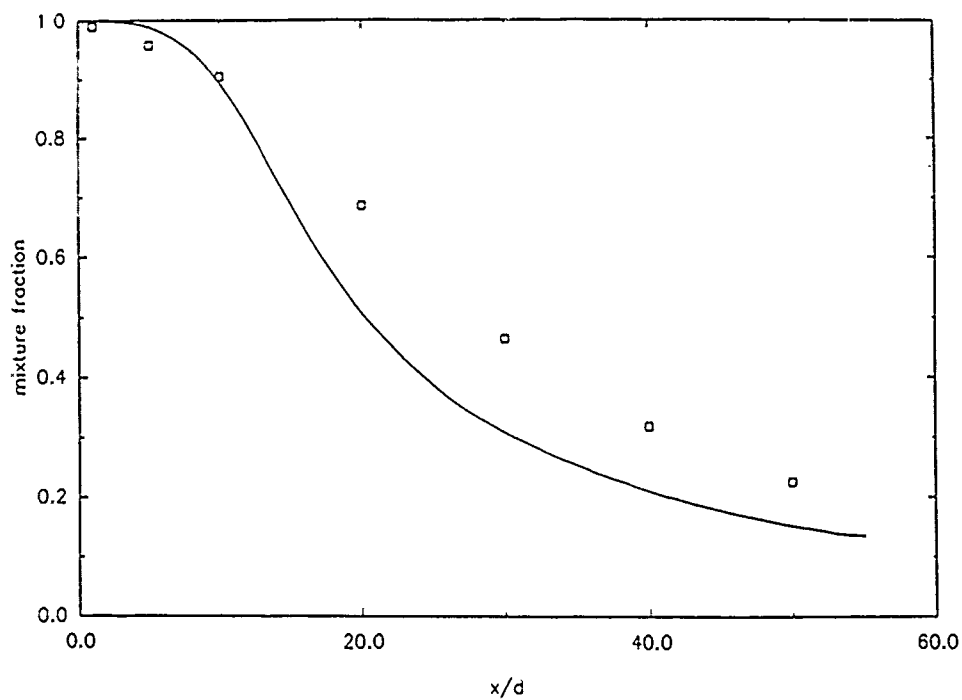


**Figure 41. Centerline axial profile of the mean mixture fraction.**

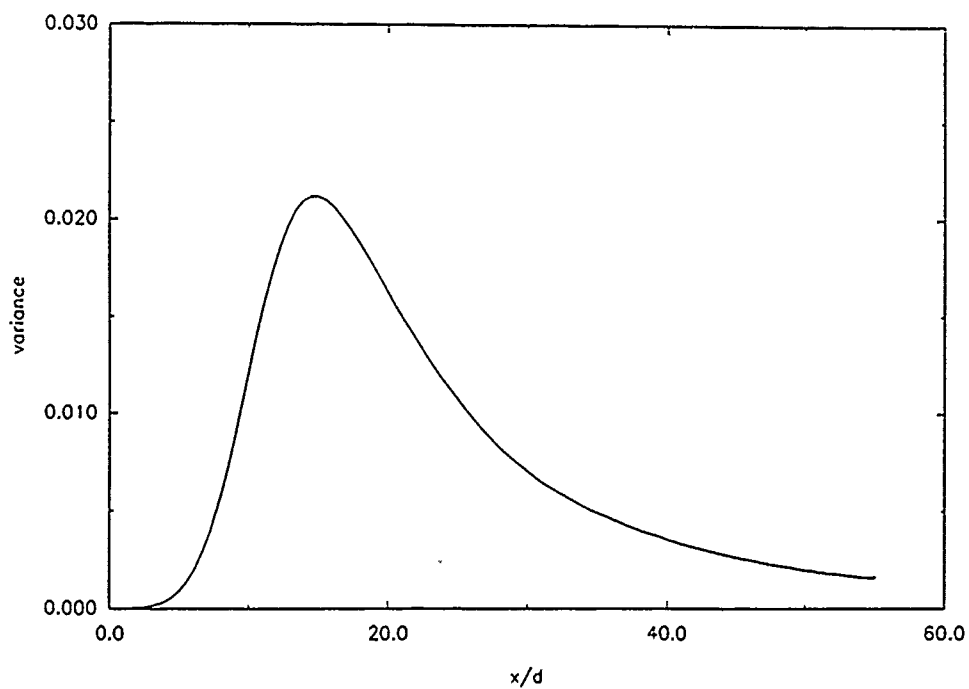


**Figure 42. Centerline axial profile of the variance in mixture fraction.**

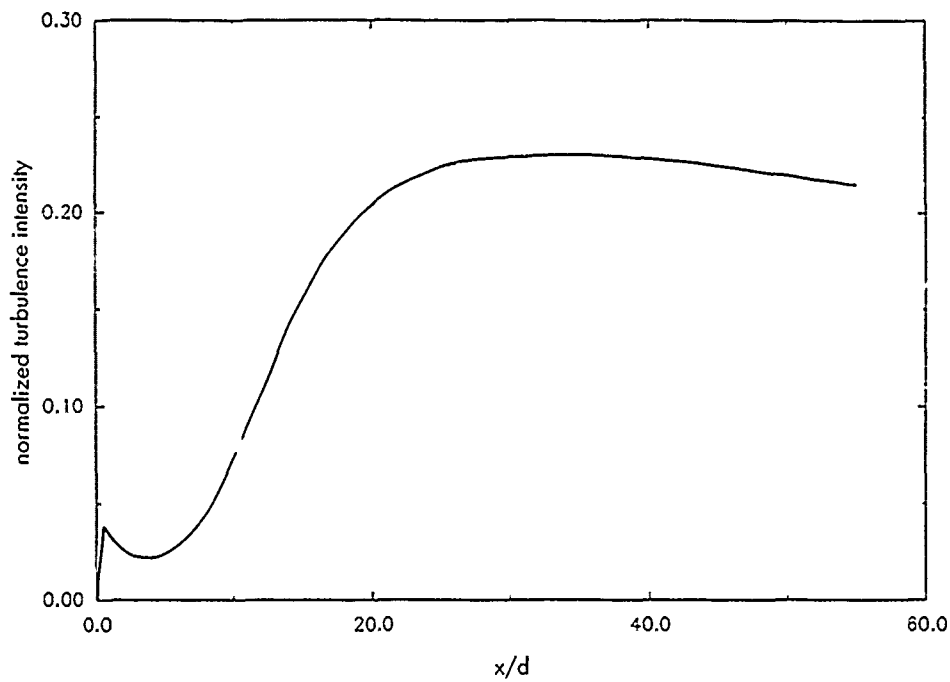


Figure 43. Normalized turbulence intensity  $\sqrt{(2k/3)} / U$  along centerline.

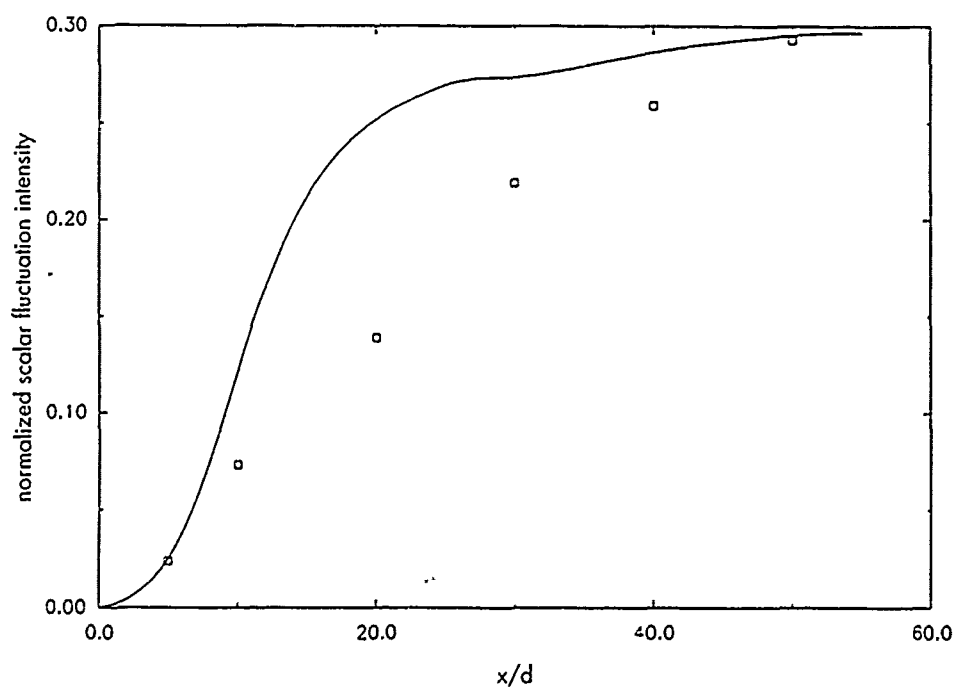
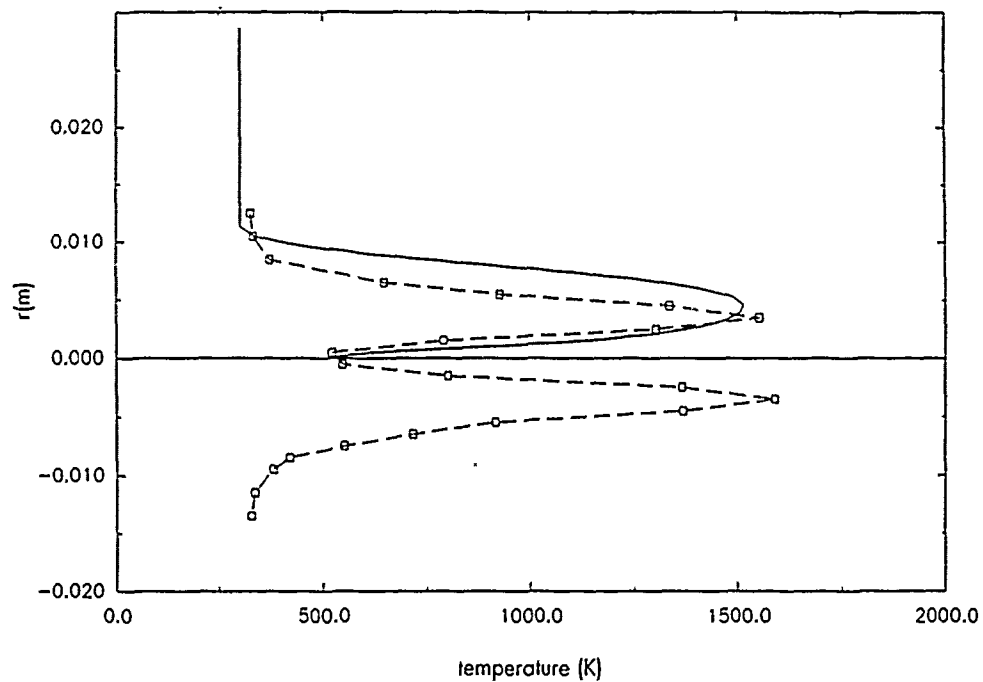
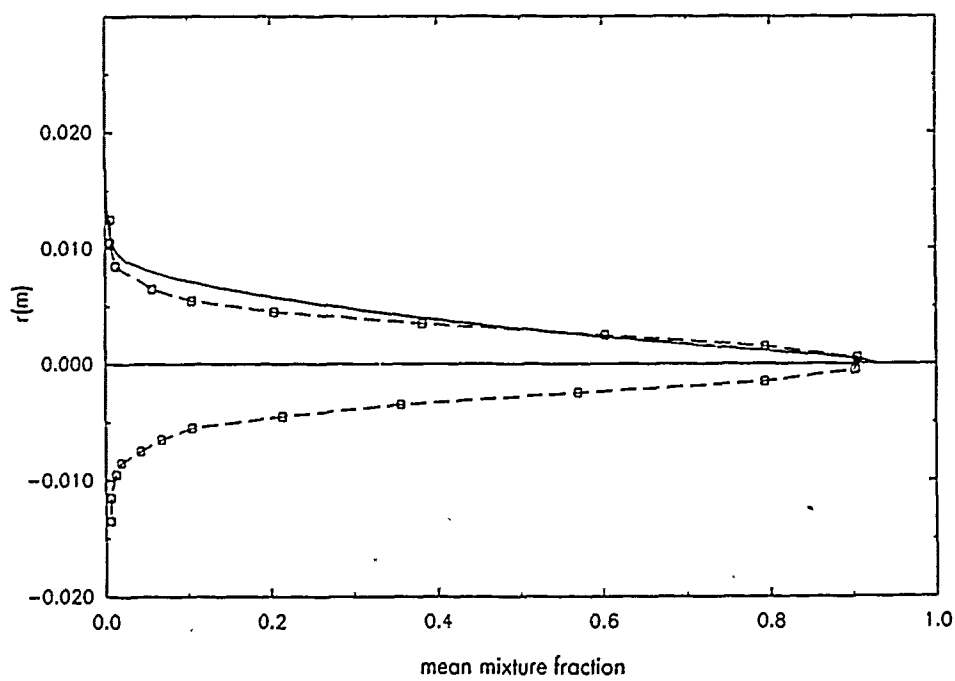


Figure 44. Comparison of predicted normalized scalar fluctuation intensity with Raman data.



(a)



(b)

**Figure 45. Comparison of predicted radial profiles with Raman data at  $x/d = 10$ .**  
 (a) Mean temperature.  
 (b) Mean mixture fraction.

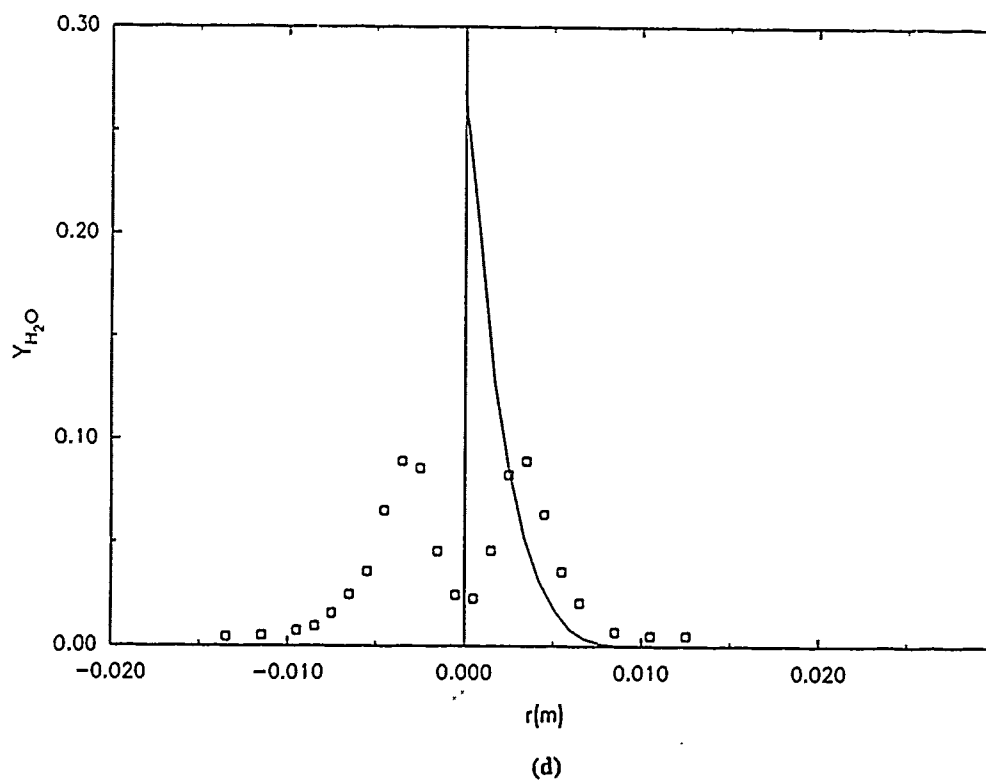
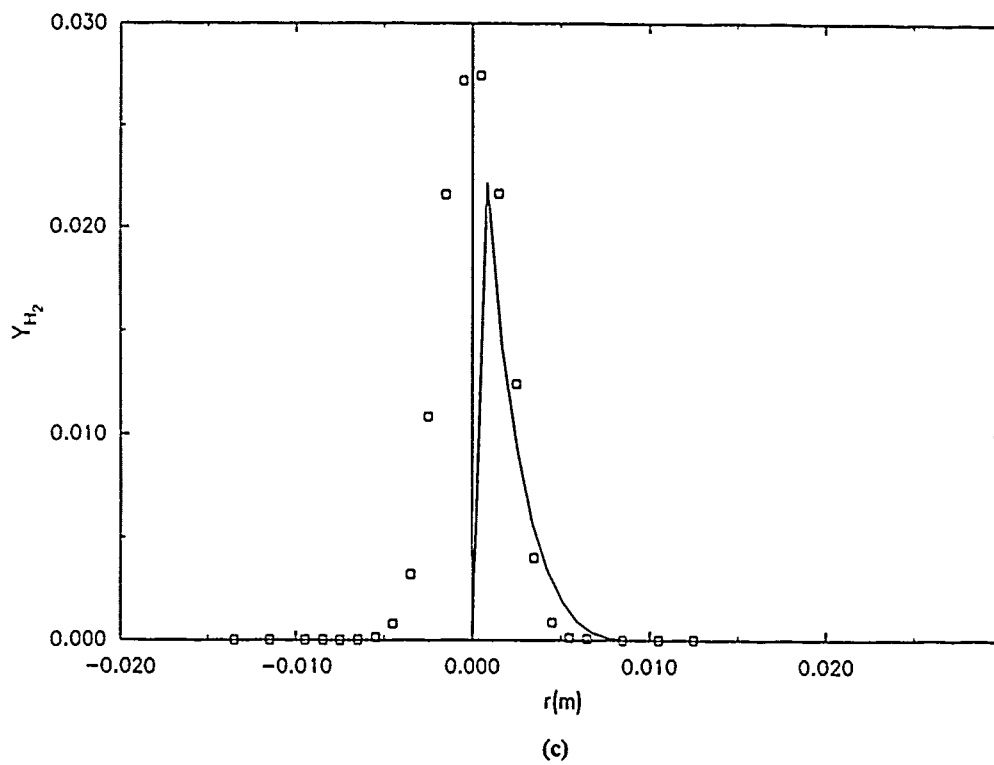


Figure 45. Comparison of predicted radial profiles with Raman data at  $x/d = 10$ .  
 (c) Mean  $H_2$ .  
 (d) Mean  $H_2O$ .

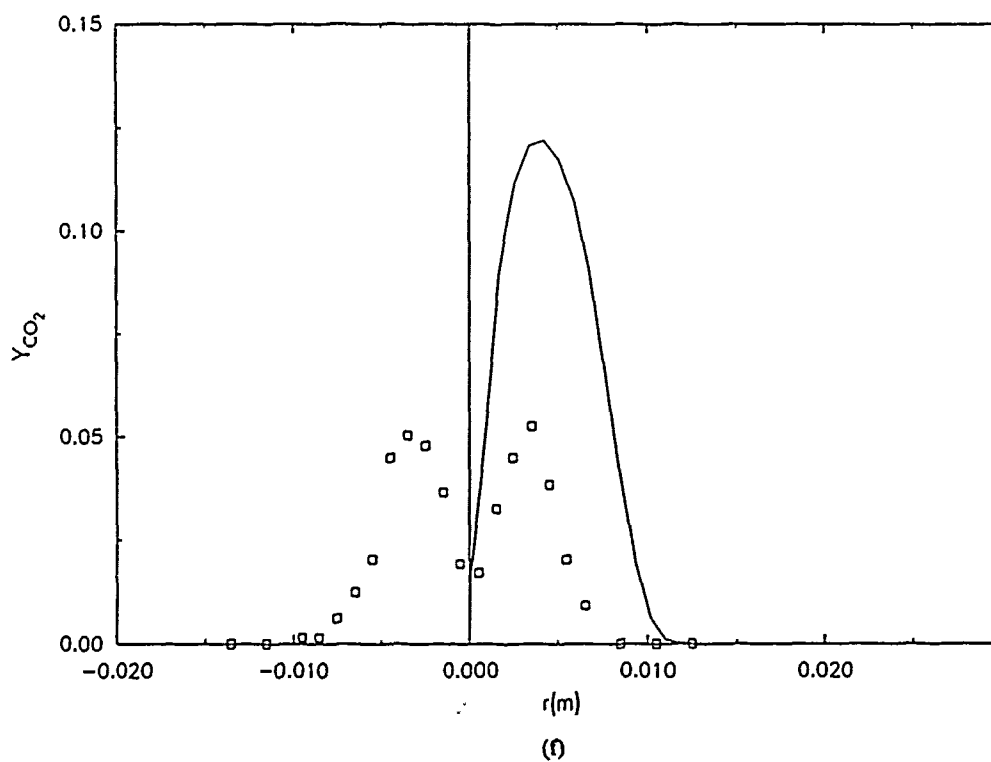
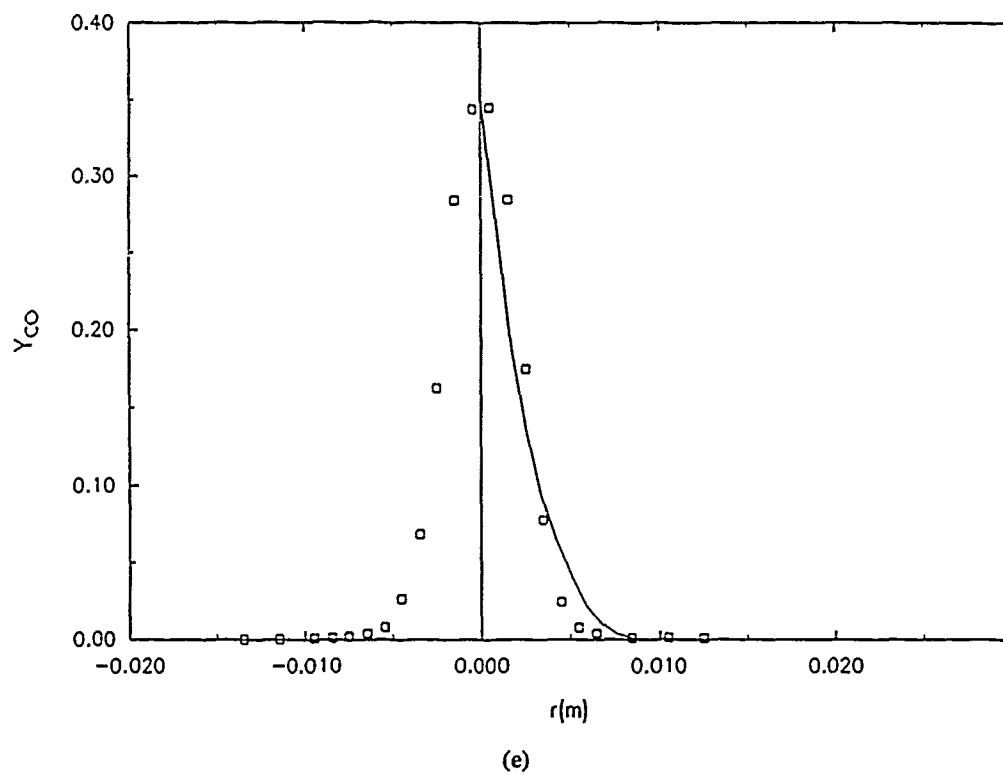


Figure 45. Comparison of predicted radial profiles with Raman data at  $x/d = 10$ .  
 (e) Mean CO.  
 (f) Mean CO<sub>2</sub>.



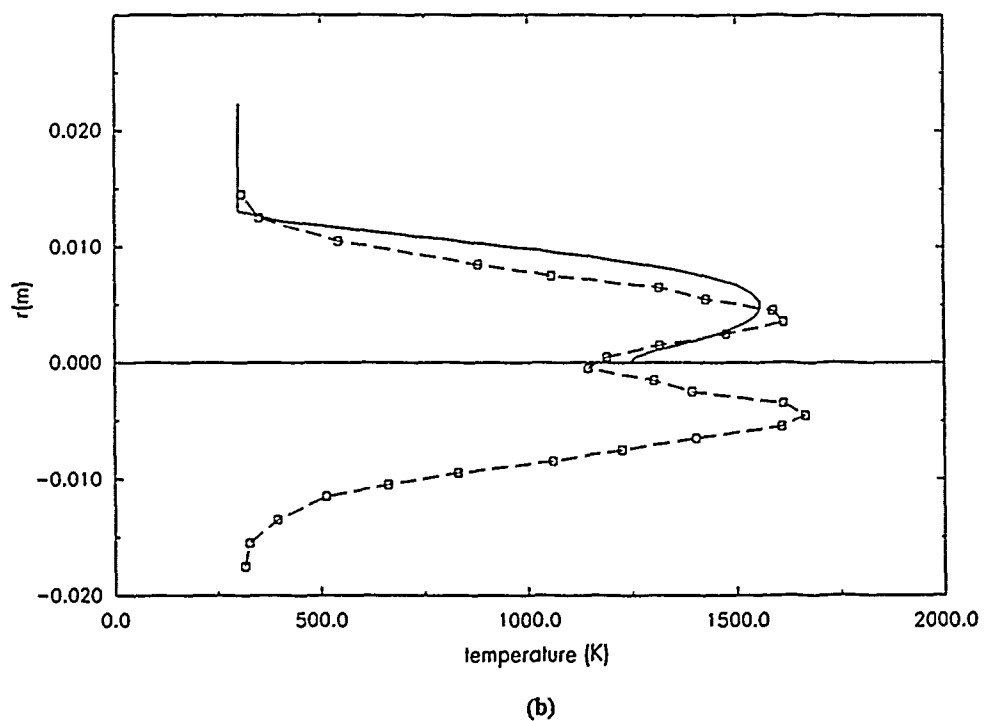
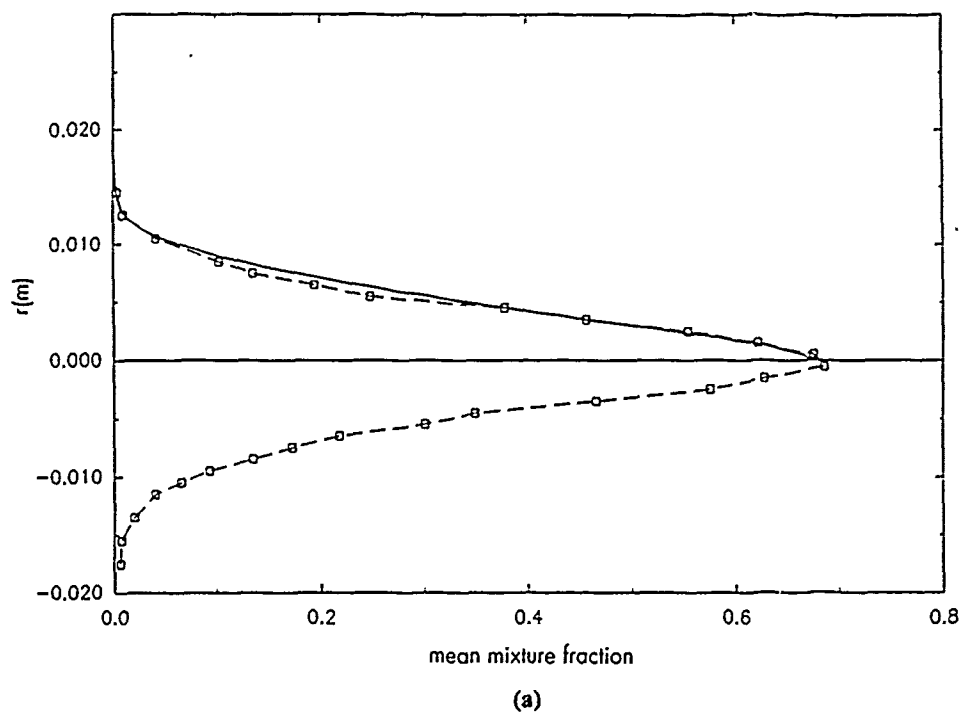


Figure 46. Comparison of predicted radial profiles at  $x/d = 15.4$  with Raman data at  $x/d = 20$ .  
 (a) Mean mixture fraction.  
 (b) Mean temperature.

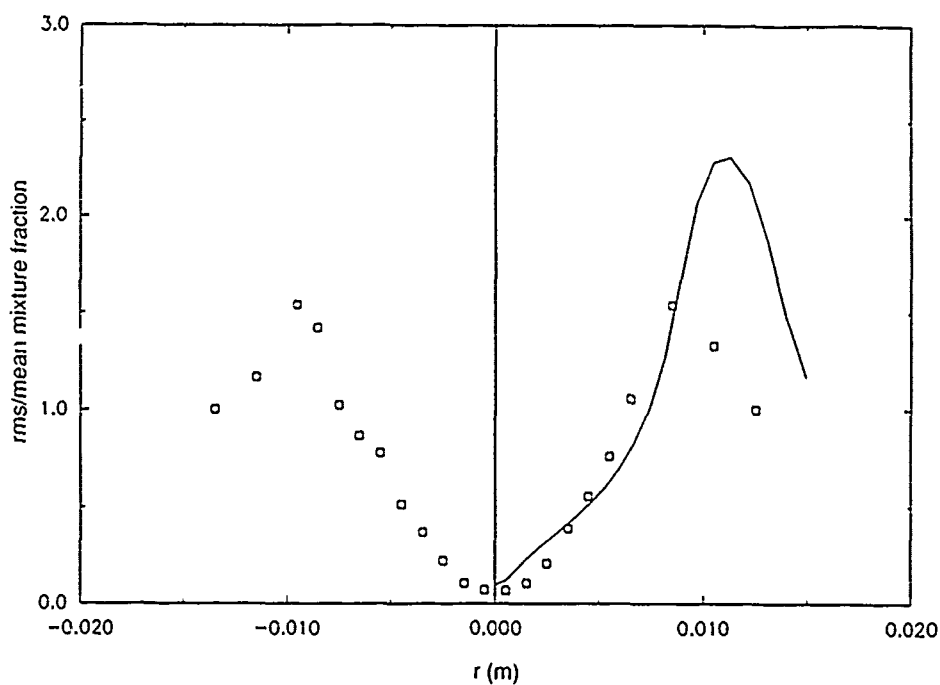


Figure 47. Comparison of the predicted normalized r.m.s. mixture fraction with the Raman data at  $x/d = 10$ .

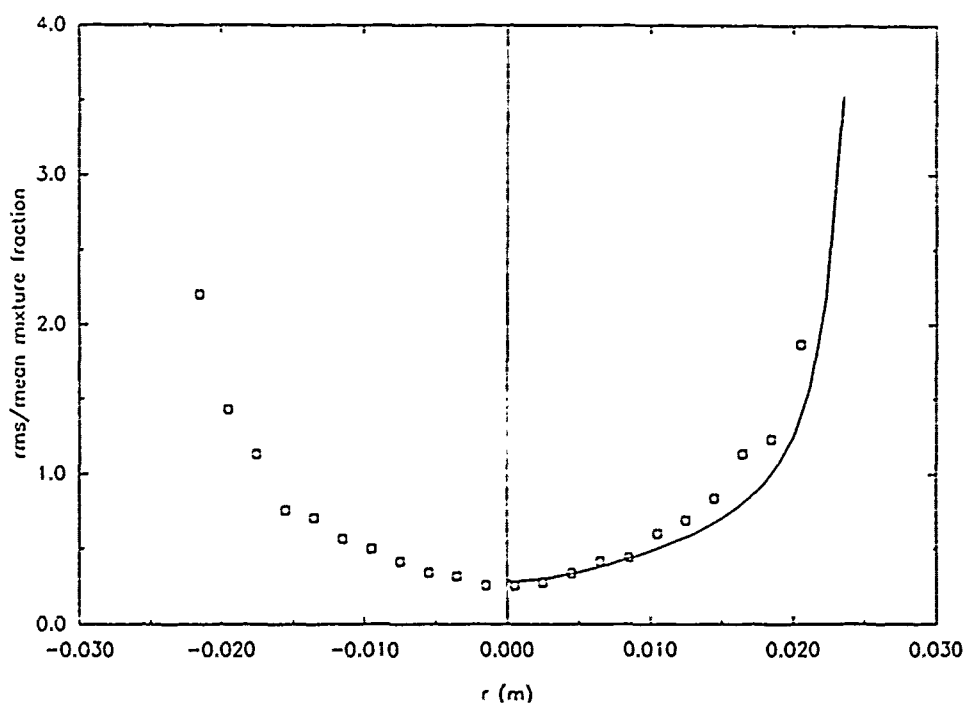


Figure 48. Comparison of the predicted normalized r.m.s. mixture fraction with the Raman data at  $x/d = 40$ .

tion takes care of the problem with the virtual origin but towards the edges of the mean mixture fraction profile, where the mean tends to zero, the quantity becomes indeterminate. The agreement at  $x/d=10$  is fairly good, although the off-axis peak is overpredicted by about 50% consistent with the overprediction of the near-exit turbulence levels. The agreement at  $x/d=40$  is very good.

## 2.6 Monte-Carlo Pdf Transport Method in Recirculating Flow

The assumption of shape – particularly the assumption of statistical independence of the scalar fluctuations – limits the number of scalars in the assumed shape pdf method. Direct pdf evolution methods are intrinsically suited to this problem of closing the chemistry. They can also relax many of the turbulence model assumptions, such as gradient diffusion, made above. Substantial difficulties arise, however, in recirculating flow particularly in complex geometries because the wall shape sets the mean pressure field.

A derivative of the full pdf evolution method is to use conventional  $k-\epsilon$  or Reynolds stress closure for the momentum equations, and the pdf evolution method for the scalar(s)' pdf only. Gradient diffusion is therefore invoked in the scalar flux, but there is no need for assumption of pdf shape. This approach is useful in internal recirculating flows where the mean pressure field is very important in setting the mean velocity field, as in bluff-body stabilized burners. This mean pressure field is not provided by the pdf evolution method. To relax even the gradient diffusion assumption, the full pdf method could be used with (i) the mean pressure field given by the mean momentum equation and (ii) the scalar fluxes given by the velocity-scalar coupling in the pdf, beyond which the velocity information in the pdf would be disregarded. The procedure is iterated to convergence.

Preliminary work on the hybrid approach has begun, with a goal of reproducing the  $\text{CO}/\text{H}_2/\text{N}_2$  flame calculation discussed above, and then going on to more complex chemistry (methane). A calculation procedure which iterates between the hydrodynamics and the pdf evolution equations has been worked out. The hydrodynamical part contains the mean flow and turbulence model equations, and the geometry of the problem. The mean velocity and the turbulence kinetic energy fields are passed to the pdf evolution equation solver. The pdf is shifted in phase space to agree with these lower moments.

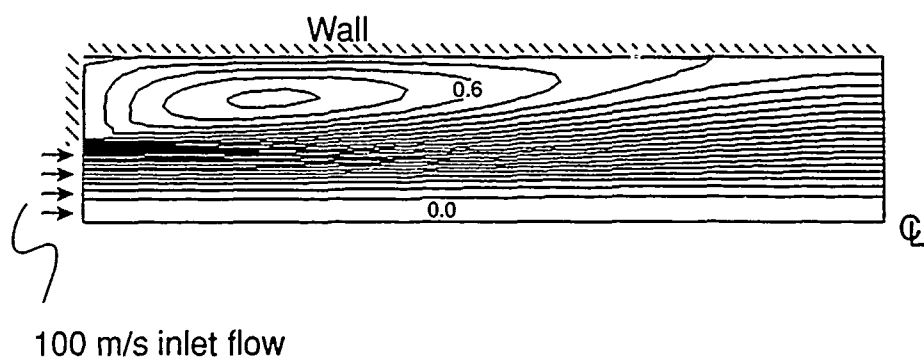
The test case is an axisymmetric constant density 1:2 sudden-expansion flow. The inlet boundary conditions are a plug 100 m/s axial velocity and a step-function profile for the conserved scalar. This (purely illustrative) calculation used a  $21 \times 21$  grid for the mean flow. Figure 49 shows contours of the stream function, and the mean and variance of the conserved scalar, all of which behave as expected.

The next step is to add scalar dimensions to the pdf and redo the two-scalar flame calculation of Section 2.5. The flexibility to handle multiscalar kinetics, without realizability constraints imposed by assumed shape pdf's, will be exploited to model the methane flame as well (three or four scalars, as necessary).

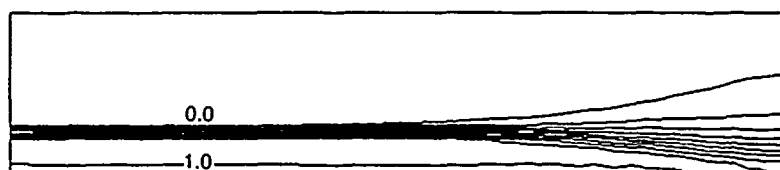
## 2.7 Universality of Turbulence-Chemistry Models

Should turbulent flames be viewed as ensembles of strained laminar "flamelets" [Peters (1987)] or as broader "distributed zones" [Bilger (1989)] of reacting species? This section shows that the answer is not unique even in a given flame. Turbulence-chemistry interactions span several orders of magnitude in Damkohler number, depending on the specific reaction and the specific turbulence process in question. Extreme cases are

(i) Relatively weak interactions which are characterized by moderate Reynolds/Peclet numbers, yielding order-of-unity Damkohler numbers for the radical recombination reactions and large Dam-



(a)



(b)



(c)

Figure 49. Application of hybrid Monte-Carlo-pdf-transport/finite-difference code to axisymmetric constant-density 1:2 sudden-expansion flow with step-function inlet profile for the conserved scalar.

(a) Stream function, contour spacing 0.03.

(b) Mean of conserved scalar, contour spacing 0.1.

(c) Variance of conserved scalar, contour spacing 0.01.

kohler numbers for the chain-branching reactions. This regime exhibits superequilibrium radical levels, which control burnout of major species and CO as well as oxidation of  $N_2$ .

(ii) Strong interactions, where even ignition reactions may have order-of-unity Damkohler numbers leading to a question of localized turbulence-induced extinction and eventually to blowoff.

To illustrate the range of interactions, chemical and fluid-mechanical scales have been compared for two types of air-breathing combustors. Diffusion flames have no intrinsic length scale, so time scales are used to compare mixing and chemistry. The physical picture to bear in mind is whether, at an interface between dissimilar reactants, turbulent straining occurs rapidly or slowly relative to the rates of important reactions.

Selected characteristic kinetic times were obtained from stirred reactor calculations, under conditions of (i) 0.1 atm  $H_2$ -air combustion, 1 ms residence time,  $H_2$  at 1100 K, air at 800 K, equivalence ratio  $\phi = 0.8$ , and (ii) 10 atm  $CH_4$ -air combustion, 10 ms residence time,  $CH_4$  at 300 K, air at 610 K, and  $\phi = 0.7$ , a stoichiometry representative of low- $NO_x$  "head-end" conditions. The two cases approximate a hypothetical supersonic combustion ramjet ("scramjet") in the mid-Mach number range (10-15) and a methane-fueled gas turbine combustor, respectively, closely enough for the present purpose of extracting kinetic time scales.

The kinetic scheme, adopted from Glarborg et al. (1986), contains 25 species and 100 reactions for methane oxidation excluding  $C_2$ -chemistry. The "thermal" and "prompt" (alkyl species-plus-nitrogen)  $NO_x$  mechanisms are also included because pollutant chemistry introduces additional time scales. Concentrations, density, and temperature from each of the stirred reactor solutions were used to estimate characteristic times of the ten reactions selected in Table I. Characteristic chemical time scales are estimated as  $\tau_c = 1/(k_f[X])$  where  $k_f$  is the reaction rate and  $[X]$  is the concentration of the more abundant reactant, with an additional concentration factor for three-body reactions. Time scales for selected reactions are shown in Table I.

Turbulence scales are estimated as follows. The integral time scale is given by  $\tau_I = \lambda_I u'$  where  $u'$  is the rms velocity fluctuation and  $\lambda_I$  is the integral length-scale. From the kinematic viscosity  $\nu$  and the dissipation rate  $\epsilon = u'^3/\lambda_I$ , the Kolmogorov time scale  $\tau_K$  follows as  $\tau_K = (\nu/\epsilon)^{1/2}$ . The relevance of the Kolmogorov time scale is worth attention.  $\tau_K$  characterizes the intense turbulent straining associated with the smallest scales. Since the pdf for scalar dissipation is log-normally distributed, this ( $\tau_K$ ) process is highly intermittent and is experienced by only a small part of the flow at any given instant.

These estimates are applied to the two cases described above, with the following assumptions: (i) in the supersonic combustor, the mean axial velocity  $\langle u \rangle = 3000$  m/s,  $u' = 300$  m/s,  $\lambda_I = 0.002$  m; the latter follows from PLIF (planar laser-induced fluorescence) flow visualization of the mixing of jets injected behind a realistically sized step into a supersonic crossflow [Correa et al. (1989)] and (ii) the mean velocity  $\langle u \rangle = 100$  m/s,  $u' = 10$  m/s,  $\lambda_I = 0.005$  m, being typical conditions in a turbine combustor. Turbulence time scales are shown in Table II.

Numerical values in Tables I and II may be used to compute the turbulent Damkohler numbers  $\tau_I/\tau_c$  and  $\tau_K/\tau_c$ , the latter also being an inverse Karlovitz number, and so to compare the turbulence and chemical scales:

(i) Scramjet: Because of the long chemical time scales (caused by the low static pressures), the reactions are slow relative to both the integral and Kolmogorov scales. The exceptions are the two-body oxyhydrogen reactions which are comparable to the integral scale. The recombination reaction time scales are comparable to the residence time, which is why there is a combustion efficiency issue in such devices. The ordering of time scales implies that partial equilibrium in the radical pool can be

a useful simplifying assumption. In any event, it is unlikely that the flamelet model would be applicable. Flame broadening by finite-rate chemistry would destroy the laminar flamelet topology.

(ii) Turbine combustor: Here the oxyhydrogen shuffle reactions are fast compared with the turbulence, except for  $O + H_2$ , which is comparable to the Kolmogorov scale. Because of the higher density, the recombination reactions have sped up and are in between the two turbulence scales. The thermal  $NO_x$  and  $CH_2 + N_2$  reactions are slow relative to both turbulence scales, but  $CH + N_2$  is fast. Time scales for the  $CH_4 + M$  and the  $CO + OH$  reactions are comparable to the integral and Kolmogorov scales, respectively.

It is clear that while some combustion reactions fall in the flamelet regime and some in the distributed regime, many important reactions fall in between. Turbulence-chemistry interactions occur in a greater variety of modes (Damkohler numbers) than accounted for by modern combustion theory. Most modern theories classify a flame as lying entirely in some particular domain on a set of intensity or time-scale axes, missing the critical issue that there are multiple interaction scales present in a single flame.

The simultaneous prediction of kinetically sensitive phenomena such as pollutants, flame stability and combustion efficiency will require recognition of the multiplicity of interactions within the same flame.

**Table I**  
**Characteristic Time Scales of Selected Reactions in Two Combustors**

Reactions		0.1 atm H <sub>2</sub> scramjet ( $\tau_c$ , s)	10 atm CH <sub>4</sub> combustor ( $\tau_c$ , s)
1.	H + O <sub>2</sub> = OH + O	$3.49 \times 10^{-5}$	$1.67 \times 10^{-7}$
2.	O + H <sub>2</sub> = OH + H	$2.64 \times 10^{-5}$	$1.81 \times 10^{-5}$
3.	H + OH + M = H <sub>2</sub> O + M	$1.59 \times 10^{-3}$	$7.20 \times 10^{-5}$
4.	N <sub>2</sub> + O = NO + N	$9.45 \times 10^4$	$3.92 \times 10^{-2}$
5.	CH <sub>4</sub> + M = CH <sub>3</sub> + H + M	—	$4.68 \times 10^{-4}$
6.	CH <sub>4</sub> + OH = CH <sub>3</sub> + H <sub>2</sub> O	—	$2.48 \times 10^{-7}$
7.	CH <sub>3</sub> + OH = CH <sub>2</sub> + H <sub>2</sub> O	—	$1.85 \times 10^{-6}$
8.	CO + OH = CO <sub>2</sub> + H	—	$2.22 \times 10^{-5}$
9.	CH + N <sub>2</sub> = HCN + N	—	$3.43 \times 10^{-6}$
10.	CH <sub>2</sub> + N <sub>2</sub> = HCN + NH	—	0.20

**Table II**  
**Characteristic Turbulence Time Scales**

	$u'$ (m/s)	$\lambda_I$ (m)	$\tau_I$ (s)	$\epsilon$ (m <sup>2</sup> /s <sup>3</sup> )	$\tau_K$ (s)
Scramjet combustor	300	0.002	$6.67 \times 10^{-6}$	$1.35 \times 10^{10}$	$6.01 \times 10^{-7}$
Turbine combustor	10	0.005	$5.0 \times 10^{-4}$	$2.0 \times 10^5$	$1.81 \times 10^{-5}$

### Section 3

#### CONCLUSIONS

The goal of this three-year research program was a quantitative understanding of turbulence-chemistry interactions in turbulent gaseous flames under conditions approaching blowoff. The program built on prior work, first on unassisted and more recently on pilot-stabilized CO/H<sub>2</sub>/N<sub>2</sub> jet flames in coflowing air.

Although the fast chemistry or "mixed-is-burned" paradigm is useful for understanding traditional design issues, present-day demands on combustion equipment and thus on computational models are increasing the need for a more advanced understanding of turbulence-chemistry interactions. For example, (i) flameout and relight in turbine combustors are related to interactions of turbulence with chain-branching reactions, (ii) hydrogen burnout in supersonic combustors is related to interactions with recombination reactions, and (iii) emissions of NO<sub>x</sub>, CO, smoke and other observables are related to nonequilibrium among species such as oxyhydrogen radicals and C<sub>x</sub>H<sub>y</sub>.

The main technical conclusions of this work are

1. To obtain higher turbulent strain rates than attainable with jet flames, a bluff-body stabilized burner was used. It will be necessary to accurately model such flows, which are more complex as regards both turbulence and numerics than jet-like flows, if the link between theory and experiment is to continue as fruitfully as before.
2. Although originally developed for H<sub>2</sub> flames, Raman systems can be modified to operate usefully even in the sooting/chemiluminescent environment of hydrocarbon flames. Measurements were made in CO/H<sub>2</sub>/N<sub>2</sub> and CH<sub>4</sub> flames.
3. Complementarily, the bluff-body stabilized burner was modeled:
  - i. A thermochemical submodel based on partial equilibrium in the oxyhydrogen radical pool was developed for the 27.5% CO/ 32.3% H<sub>2</sub>/ 40.2% N<sub>2</sub>-air system. The chemistry can be described in terms of two scalars.
  - ii. The elliptic form of the time-averaged Navier Stokes equations with  $k$ - $\epsilon$  closure was solved using an iterative finite volume/pressure correction algorithm. Mean properties such as density were obtained at each iteration by convolution with the joint pdf over the two thermochemical scalars. The pdf itself was obtained by the moment equation/assumed shape method.
4. Calculations were compared with the data. Agreement was very encouraging on mixture fraction mean and variance, temperature, and species concentration fields. Numerical error in the mean hydrodynamic field calculations can be demonstrably reduced to acceptable levels. The  $k$ - $\epsilon$  turbulence model gave too rapid an initial decay. To improve the turbulence model and to have a formalism permitting three or more scalars as required for hydrocarbon fuels, the pdf transport method should be merged with conventional solvers for the mean hydrodynamics.
5. Preliminary work on Monte-Carlo pdf transport methods in recirculation stabilized flames.

Second-order closure of the turbulence correlations could have been employed in this study to relax some of the  $k$ - $\epsilon$  model assumptions. The plan, however, is to proceed directly to the Monte-Carlo joint pdf transport method, which is closed to all orders and will provide the same level of modeling sophistication in recirculating flow as already demonstrated for jet flames [Pope and Correa (1987)].



6. The challenge of developing universal turbulence-chemistry models can be assessed by direct calculation of a matrix of Damkohler numbers,  $D_{ij} \equiv \tau_i / \tau_j$ , where  $j$  represents the chemical reaction of interest and  $i$  the turbulence scale of interest. It becomes apparent that while some combustion reactions fall in the flamelet regime and some in the distributed regime, many important reactions fall in between. Turbulence-chemistry interactions occur in a greater variety of modes than accounted for by modern combustion theory. The simultaneous prediction of kinetically sensitive phenomena such as pollutants, flame stability, and combustion efficiency will require a new approach.

Suggestions for future work are

- i. Laser Doppler Velocimetry, minor species measurements (laser-induced fluorescence), and joint major-minor species measurements (LIF-spontaneous Raman) in recirculation-stabilized flames.
- ii. Development and assessment of the hybrid Navier-Stokes-for-mean-flow/pdf- transport method, as outlined above.

## REFERENCES

1. Amano, R.S. and Kodali, V.S., (1984), "Prediction of Turbulent Flows in Combustors by Using Reynolds-Stress Closure," Paper AIAA-84-1494.
2. Bilger, R.W., (1980), *Comb. Sci. Tech.* 22, pp. 251-262.
3. Bilger, R.W., (1976), *Prog. Energy Combust. Sci.* 1, pp. 87-109.
4. Bilger, R.W. and Starner, S.H., (1983), *Combust. Flame* 51, pp. 155-176.
5. Bilger, R.W., (1989), Twenty-Second (International) Symposium on Combustion, The Combustion Institute, Pittsburgh, PA, pp. 475-488.
6. Chen, J-Y., Kollmann, W., and Dibble, R.W., (1989), *Comb. Sci. Tech.* 89, p. 315.
7. Correa, S.M. and Pitz, R.W., (1982), "The Effect of Large-Scale Structures on Eulerian Models of Turbulent Combusting Flows," Eastern States Section of Combustion Institute, Fall Technical Meeting, Atlantic City, NJ.
8. Correa, S.M., (1984), *ALAA Journal*, 22, pp. 1602-1608.
9. Correa, S.M., Drake, M.C., Pitz, R.W., and Shyy, W., (1984), Twentieth Symposium (International) on Combustion, The Combustion Institute, Pittsburgh, PA, pp. 337-343.
10. Correa, S.M., (1986), "Carbon Monoxide and Turbulence-Chemistry Interactions: Measurements and Modeling of Turbulent Jet Diffusion Flames," Annual Report, AFOSR Contract No. F49620-85-C-0035.
11. Correa, S.M. and Shyy, W., (1987), *Prog. Eng. and Comb. Sci.*, 13, pp. 249-292.
12. Correa, S.M., Warren, R.E., Gulati, A., Haller, F., and Kaiser, W.O., (1989) "Supersonic Sudden-Expansion Flow with Fluid Injection: an Experimental and Computational Study," Paper AIAA 89-0389.
13. Correa, S.M. and Gulati, A., (1989), Twenty-Second (International) Symposium on Combustion, The Combustion Institute, Pittsburgh, PA, pp. 599-606.
14. Correa, S.M., Gulati, A. and Pope, S.B., (1988), *Combust. Flame*, 72, pp. 159-173.
15. Correa, S.M., (1989), "Flame Structure: A Discussion," Proceedings of NASA Langley/ICASE Combustion Workshop, Oct. 2-4, 1989, to be published by Springer-Verlag.
16. Dibble, R.W., Kollmann, W., and Schefer, R.W., (1984), Twentieth Symposium (International) on Combustion, The Combustion Institute, Pittsburgh, PA, pp. 345-352.
17. Dibble, R.W., Masri, A.R., and Bilger, R.W., (1987), "The Spontaneous Raman Scattering Technique Applied to Nonpremixed Flames of Methane," *Combust. Flame*, 67, pp. 189-206.
18. Dibble, R.W., Starner, S.H., Masri, A.R., and Barlow, R.S., (1990), "An Improved Method of Data Acquisition and Reduction for Laser Raman-Rayleigh and Fluorescence Scattering from Multispecies," *App. Physics, B* 51, pp. 1727-1731.
19. Drake, M.C., Lapp, M., and Penney, C.M., (1982), "Use of Raman Effect for Gas-Temperature Measurement," in *Temperature, Its Measurement and Control in Science and Industry*, , Vol. 5, J.F. Schooley, Ed., Amer. Inst. Physics, p. 631.
20. Drake, M.C., Correa, S.M., Pitz, R.W., Shyy, W., and Fenimore, C.P., (1987), *Combust. Flame*, 69, pp. 347-365.
21. Fenimore, C.P. and Moore, J., (1974), *Combust. Flame* 22, pp. 343-351.
22. Gibson, M.M., (1985), "Effects of Streamline Curvature on Turbulence," in S.H. Davis and J.L. Lumley (eds.) *Frontiers in Fluid Mechanics*, pp. 184-198, Springer-Verlag, Berlin.
23. Glarborg, P., Miller, J.A., and Kee, R.J., (1986), *Combust. Flame*, 65, pp. 177-202.
24. Gulati, A., and Dibble, R.W., (1991), "Raman Measurements in a Sooty Bluff-body Stabilized Pure Methane Flame," Manuscript in Preparation.
25. Harlow, F.H. and Welch, J.E., (1965), *Phys. of Fluids*, 8, pp. 2182-2189.

26. Janicka, J. and Kollmann, W., (1982), *Combust. Flame* 44, pp. 319-336.
27. Janicka, J. and Kollmann, W., (1979), Seventeenth Symposium (International) on Combustion, The Combustion Institute, Pittsburgh, PA, pp. 421-430.
28. Jones, W.P. and Whitelaw, J.H., (1984), Twentieth Symposium (International) on Combustion, The Combustion Institute, Pittsburgh, PA, pp. 233-249.
29. Kaskan, W.E., (1959), *Combust. Flame* 3, pp. 49-60.
30. Koochesfahani, M.M., Dimotakis, P.E., and Broadwell, J.E., (1985), *ALAA J.* 23, pp. 1191-1194.
31. Lapp, M., Drake, M.C., Penney, C.M., Pitz, R.W., and Correa, S.M., (1983), "Turbulent Combustion Experiments and Modeling," General Electric Company Report 83CRD049, DoE Contract DE-AC04-78 ET 13146.
32. Launder, B.E. and Spalding, D.B., (1974), *Comput. Meths. in Appl. Mech. Engrg.*, 3, pp. 269-289.
33. Launder, B.E., Reynolds, W.C., and Rodi, W., (1984), *Turbulence Models and Their Applications*, Editions Eyrolles, Paris.
34. Leonard, B.P. (1981), *Recent Advances in Numerical Methods in Fluids*, Vol. 2, C. Taylor, ed., Pineridge Press, Swansea, U.K.
35. Leschziner, M.A. and Rodi, W., (1980), *ASME J. Fluid Engrg.* 103, pp. 352-360.
36. Libby, P.A. and Williams, F.A., (1980), ed., *Turbulent Reacting Flows*, Springer-Verlag, New York.
37. Lockwood, F.C. and Stolakis, P., (1983), "Assessment of Various Turbulence Models for Turbulent Round Diffusion Jets With Combustion," Fourth Symposium on Turbulent Shear Flows, pp. 1025-1031.
38. Mansour, M.S., Bilger, R.W., and Dibble, R.W., (1989), Twenty-Second Symposium (International) on Combustion, The Combustion Institute, Pittsburgh, PA, pp. 711-719.
39. Masri, A.R., Bilger, R.W., and Dibble, R.W., (1987), "Fluorescence Interference with Raman Measurements in Nonpremixed Flames of Methane," *Combust. Flame* 68, pp. 109-119.
40. Masri, A.R., Bilger, R.W., and Dibble, R.W., (1988), *Combust. Flame* 71, pp. 245-266.
41. Masri, A.R., and Dibble, R.W., (1989), Twenty-Second Symposium (International) on Combustion, The Combustion Institute, pp. 607-618.
42. McGuirk, J.J., Taylor, A., and Whitelaw, J.H., (1981), "The Assessment of Numerical Diffusion in Upwind Difference Calculations of Turbulent Recirculating Flows," 3rd Symposium on Turbulent Shear Flows, Springer-Verlag, pp. 206-224.
43. Mei, R. and Plotkin, A., (1986), *ALAA J.* 24, pp. 1106-1111.
44. Paczko, G., Lefdal, P.M., and Peters, N., (1986), Twenty-first Symposium (International) on Combustion, The Combustion Institute, Pittsburgh, PA, pp. 739-748.
45. Patankar, S.V., (1980), *Numerical Heat Transfer and Fluid Flow*, Hemisphere, Washington, DC.
46. Penner, S.S., Wang, C.P., and Bahadori, M.Y., (1984), Twentieth Symposium (International) on Combustion, The Combustion Institute, Pittsburgh, PA, pp. 1149-1176.
47. Peters, N., (1988), Twenty-First (International) Symposium on Combustion, The Combustion Institute, Pittsburgh, PA, pp. 1231-1250.
48. Pope, S.B., (1985), *Prog. Energy Combust. Sci.* 11, pp. 119-192.
49. Pope, S.B. and Correa, S.M., (1987), Twenty-First (International) Symposium on Combustion, The Combustion Institute, Pittsburgh, PA, pp. 1341-1348.
50. Raithby, G.D., (1976), *Comput. Meths. Appl. Mech. Engrg.* 9, pp. 75-103.
51. Rodi, W., (1980), "Turbulence Models and Their Application In Hydraulics," IAHR State-of-the-Art-Series Monograph, Delft, The Netherlands.
52. Roquemore, W.M., Britton, R.L., and Sandhu, S.S., (1982), "Investigation of the Dynamic Behavior of a Bluff Body Diffusion Flame Using Flame Emission," AIAA Paper No. 82-0178.
53. Schefer, R.W., Namazian, M., and Kelly, J., (1989), Twenty-Second (International) Symposium

- on Combustion, The Combustion Institute, Pittsburgh, PA, pp. 833-842.
54. Shyy, W. and Correa, S.M., (1985), "A Systematic Comparison of Several Numerical Schemes for Complex Flow Calculations," AIAA Paper 85-0440.
  55. Spalding, D.B., (1972), *Inter. J. for Numer. Meths. In Engrg.* 4, pp. 551-559.
  56. Starner, S.H. and Bilger, R.W., (1980), *Comb. Sci. Tech* 21, pp. 259.
  57. Starner, S.H. and Bilger, R.W., (1981), Eighteenth Symposium (International) on Combustion, The Combustion Institute, Pittsburgh, PA, pp. 921-930.
  58. Strahle, W.C. and Lekoudis, S.G., (1985), "Evaluation of Data on Simple Turbulent Reacting Flows," AFOSR-TR-85-0880.
  59. Switzer, G.L., Goss, L.P., Trump, D.D., Reeves, C.M., Stutrud, J.S., Bradley, R.P., and Roquemore, W.M., (1985), "CARS Measurements in the Near-Wake Region of an Axisymmetric Bluff body Combustor," *AIAA Paper* 85-1106.
  60. Tuann, S-Y and Olson, M.D., (1978), *J. Comput. Phys.* 14, pp. 105-125.
  61. Vinokur, M., (1974), *J. Comput. Phys.* 14, pp. 105-125.
  62. Warnatz, J., (1981), *Comb. Sci. Tech.* 26, pp. 203-213.

## Section 5

### WRITTEN PUBLICATIONS

The following publications were made during the reporting period May 1988 - May 1991, supported wholly or in part by this contract:

1. Gulati, A. and Correa, S.M., "Local Extinction Due to Turbulence in Non-premixed Flames," AIAA Paper No. 87-1717, 23<sup>rd</sup> AIAA Joint Propulsion Conference, San Diego, CA, June 29-July 2, 1987.
2. Correa, S.M. and Gulati, A., "Non-premixed Turbulent CO/H<sub>2</sub> Flames at Local Extinction Conditions," Twenty-Second (International) Symposium on Combustion, The Combustion Institute, Pittsburgh, PA, pp. 599-606, 1988.
3. Gulati, A. and Correa, S.M., "Raman/LV Measurements and Modeling in a CO/H<sub>2</sub>/N<sub>2</sub> Flame at High Reynolds Number," Paper 89-0056, 27<sup>th</sup> AIAA Aerospace Sciences Meeting, Reno, NV, Jan. 9-12, 1989.
4. Correa, S.M., "Appropriate Turbulence-Chemistry Models for Nonpremixed Combustion," Chemical and Physical Processes in Combustion, Class I Report 89CRD179, GE Corporate Research and Development Center, Schenectady, New York, 1989, also Eastern States Section of Combustion Institute, Fall Technical Meeting, Albany, NY, Oct. 30 - Nov. 1, 1989.
5. Correa, S.M., "Relevance of Non-premixed Laminar Flames to Turbulent Combustion," Proceedings of NASA Langley/ICASE Combustion Workshop, Oct. 2-4, 1989, to be published by Springer-Verlag.
6. Correa, S.M., "A Review of NO<sub>x</sub> Formation Under Gas-Turbine Combustion Conditions," submitted to Combustion Science and Technology, December 1990.
7. Correa, S.M. and Gulati, A., "Modeling Measurements in a Bluff-Body Stabilized Flame," submitted to *Combustion and Flame*, August 1991.

## **Section 6**

### **PROFESSIONAL PERSONNEL**

Dr. Sanjay M. Correa and Dr. Anil Gulati were principal investigators on this project. They were supported by Mr. Frank Haller, laser diagnostics specialist, and Ms. Janet Sober, computer analyst.

Dr. Correa earned his Ph.D. (Aerospace Engineering) in 1981 from the University of Michigan, with a thesis entitled, "Group Behavior of Liquid Fuel Sprays." Dr. Gulati earned his Ph.D. (Aerospace Engineering) in 1986 from the University of Michigan, with a thesis entitled, "Simultaneous Density-Velocity Measurements in Premixed Turbulent Flames to Assess a Theoretical Model."

## **Section 7**

### **INTERACTIONS**

The following external interactions occurred or were arranged during the reporting period May 1988 to June 1991:

#### **University Seminars**

Ohio State University (January 1989)

University of Connecticut (November 1989)

Cornell University (December 1989)

MIT (November 1990)

#### **Invited Talks**

Current Problems in Gas-Turbine Combustion

Fall Technical Meeting

Eastern States Section of the Combustion Institute

December 3-5, 1990

Orlando, Florida.

Successes and Failures of Numerical Combustion

SIAM Fourth International Symposium on Numerical Combustion

December 2-4, 1991

St. Petersburg, Florida.

#### **Other Interactions in which AFOSR-Sponsored Research was Discussed**

SANDIA Turbulent Combustion Research Group meetings (2/year)

AIAA Short Course, Leader: Computational Methods in Combustion: Gas-Turbines, Ramjets and Scramjets, Orlando, FL, July 1990.